
Electronic Theses and Dissertations, 2020-

2022

Terahertz Spintronics with Antiferromagnetic Insulators

Gyan Khatri
University of Central Florida

 Part of the [Physics Commons](#)

Find similar works at: <https://stars.library.ucf.edu/etd2020>

University of Central Florida Libraries <http://library.ucf.edu>

This Doctoral Dissertation (Open Access) is brought to you for free and open access by STARS. It has been accepted for inclusion in Electronic Theses and Dissertations, 2020- by an authorized administrator of STARS. For more information, please contact STARS@ucf.edu.

STARS Citation

Khatri, Gyan, "Terahertz Spintronics with Antiferromagnetic Insulators" (2022). *Electronic Theses and Dissertations, 2020-*. 1590.

<https://stars.library.ucf.edu/etd2020/1590>

TERAHERTZ SPINTRONICS WITH ANTIFERROMAGNETIC
INSULATORS

By

GYAN KHATRI

BS Tribhuvan University, 2011

MS Tribhuvan University, 2015

MS University of Central Florida, 2018

A dissertation submitted in partial fulfillment of the requirements
for the degree of Doctor of Philosophy
in the Department of Physics
in the College of Sciences
at the University of Central Florida
Orlando, Florida

Summer Term

2022

Major Professor: Enrique Del Barco

© 2022 Gyan B. Khatri

ABSTRACT

The existence of the THz gap in the electromagnetic spectrum is not only preventing the advancement of several technologies but also hindering research and developmental activities due to a lack of research facilities operating in the gap region. There is a plethora of materials with dynamics lying in the THz gap region whose study could potentially lead to the development of new technologies for the generation, detection, and processing of THz signals. Antiferromagnets are gaining recent interest due to their high frequency dynamics lying in the THz region, and their potential uses as active elements in THz spintronics devices have been suggested. This dissertation focuses on the study of insulating antiferromagnets for their potential use in future THz spintronic devices. The first chapter is the introductory one. In the second chapter we focus on the development of a state-of-the-art continuous polarization tunable quasi-optical measurement system operating in the frequency range 220GHz-1.1THz, at temperatures 5K-300K and a maximum magnetic field of up to 9T. The operation of this custom designed system is discussed, and initial results from the test measurements on MnF₂ single crystals verify its capabilities. In the third chapter we discuss results from a detailed spectroscopic study performed on two stoichiometric compounds of a novel two-dimensional antiferromagnetic insulator from the MnBi₂Te₄(Bi₂Te₃)_n family with n=1 and 2. The motion of the antiferromagnetic modes with the direction of applied magnetic field reveal the anisotropic nature of the system, characterized by an easy magnetic symmetry axis and a corrugated hard plane that change slightly with the stoichiometry variation. Our results show how the transition temperature also varies between n=1 and n=2 compounds, indicating that the exchange interaction originating from the antiferromagnetic order changes with the interlayer configuration. In the last chapter we discuss our results on single electron transistor measurements where we realize a stable 1- and 2-input single molecule logic gates.

To my parents, my wife, and my newly born son
For their love, support, inspiration, and blessings

ACKNOWLEDGEMENTS

I would like to take this opportunity to show my gratitude towards all of those whose guidance, inspiration, love, and support helped me achieve my dream of getting a PhD degree. Without you all it wouldn't have been possible to get to this point in my academic career.

First, I would like to thank my advisor Dr. Enrique Del Barco for giving me this great opportunity to work in his lab as a graduate researcher. I always feel proud to be one of your graduate students. Coming from Nepal without any experimental background to work in an experimental group involving complex technical skills was a big challenge, and you have walked me through every step to get through this. Your support and advice every time I was in need were of immense value. I always liked the way how easily you solved the complicated problems, at least for me, that I came across over these six years as a graduate student. I feel lucky to have learned experimental skills first-hand from one of the finest experimentalists like you. I must tell this, that each time I called you to the lab and you stopped by, I always learned something new from you. I will miss this once I leave the group. Thanks for always inspiring and challenging me towards my goal. To me, you will always remain a role model of a dedicated researcher, an efficient professional, and a fantastic human being.

I would also like to thank my committee members Dr. Michael Chini and Dr. Yasuyuki Nakajima from the Department of Physics, and Dr. Konstantin Vodopyonov from CREOL for serving on my thesis committee.

I would like to acknowledge all the people in the DelBarco group, former and current, who I came across in these wonderful six years. I would like to thank Marta for building my foundation by teaching me fundamental research skills in the lab. I would like to thank Priyanka, Rebecca, and Cameron for their excellent role as senior lab mates in the group. We enjoyed helping and teaching each other as well as making fun of each other while remaining focused on our end goal. Thanks for transferring all that important knowledge to me. I will always remember being in that junior role while we four were in the group for a

long time. And all my junior group members: Francis, Justin, Greg, Jake and Romena, thanks for trusting and helping me as a group leader. None of you have ever denied my request to perform any talk in the lab. All of you are wonderful. I enjoyed spending a lot of time with Greg while working on the high frequency set up and experiments. I wish you all the very good luck towards your PhD journey. I would like to thank our Post-Docs Dr. Jaesuk Kwon and Dr. Ran Liu for cooperating while working together in the lab. Ran, you are a brilliant researcher. Jaesuk, I will remember you as a dedicated researcher with vast experience who knows almost everything in the lab. Thanks for working with me in the same project for two years. Ran, you are simply a brilliant researcher, keep shining. I would also like to thank our visiting professor Dr. Yan Liu from China for teaching me difficult spintronics theory and calculations.

I would like to thank Prof. Hechang Lei from Renmin University, China for sending MBT samples for us. I would like to acknowledge the whole MURI team for providing wonderful opportunities to learn about antiferromagnetic spintronics in a collaborative way. I would like to specifically acknowledge Prof. David Lederman's group from the UCSC and Prof. Fengyuan Yang's group from OSU for sending samples for our study, and Prof. Ran Cheng's group from the UCR for the theoretical collaboration regarding. I would like to thank Prof. Simranjeet Singh from CMU for starting I would like to thank Prof. Andrew Kent from NYU for giving me an opportunity to work in his lab. I would also like to thank Hans Van Tol from NHMFL for his assistance during our visit to his lab. I would like to acknowledge Dr. Javier Gonzalez for his help in simulation study of bowtie antennas. I would also like to thank Seth from Dr. Peale's group for teaching me several cleanroom techniques and SEM, and Jesse from Dr. Ishigami's group for teaching me AFM techniques. I would also like to thank Tommy for your valuable suggestions while being together in the office.

I would like to thank the Physics Department and the whole UCF family for giving me this wonderful opportunity to come here to the USA, from a third world country in pursuit of a PhD degree and helping me get through this journey. I would like to thank current and former chair of the Physics Department Dr. Joshua Colwell and Dr. Eduardo Mucciolo for their support and encouragement. I would

also like to thank everyone from the administrative and accounting side of the Physics Department, particularly: Esperanza, Jessica, Nikitta, Evgenia, Leida, and Sierra. You guys have made it very easy to work in the Department. I would like to express my special thanks to Dr. Robert Peale for teaching me many experimental techniques, answering my research related questions, and allowing me access to his lab whenever needed. I am also grateful to our cleanroom technician Nathan Aultman and cryogenic facility manager Dr. David Richardson for their help and cooperation.

At last, but not the least, I would like to express my deepest gratitude to all of those from the non-academic side who helped me keep motivated towards my goal. I am always grateful towards my parents for their love, support, inspiration, and blessings towards me. Thanks for believing in me and aspiring towards higher education even though you never got such opportunities. I am grateful to my dear wife, Rishma, for your evergreen love, support, care, and encouragement towards me. Thanks for waking me up and inspiring when I was running low in my graduate life. I cannot imagine where I would be now if you were not in my life. Thanks for believing in a guy with Generalized Anxiety Disorder or Depression and inspiring and supporting him to fight his mental issue while achieving his dream of getting a PhD degree in Physics coming abroad. You are simply amazing, Sanu. In this regard I would also like to thank all the doctors who helped me in difficult times, namely: Dr. Mohan, Dr. Chacko, and Dr. Jacob. I would also like to acknowledge my brothers Khim Khatri, Dr. Dhan Khatri, (soon to be a Dr.) Himal Khatri, sister-in-law Laxmi Khadka, Cousin Mina Thapa and friend Jeevan Thapa for their love and support in every step. I would like to thank all my friends, senior and junior relatives back home, Nepali students in UCF, Nepalese community in Orlando and all my well-wishers for their direct/indirect support. Finally, I would like to express my deepest love to my dear son Riyan, who is 11 days old at the time I am writing this. Thanks, God, for sending him as a lucky charm in our life.

TABLE OF CONTENTS

LIST OF FIGURES	xii
LIST OF TABLES	xxvi
LIST OF ABBREVIATIONS	xxvii
CHAPTER 1: INTRODUCTION	1
1.1 Background	1
1.2 High frequency instrumentation	11
1.3 Spectroscopic characterization of 2D magnets	14
1.4 Molecular electronics using SETs	15
1.5 References	17
CHAPTER 2: A CONTINUOUS FREQUENCY AND POLARIZATION TUNABLE HIGH FREQUENCY SPECTROSCOPIC SYSTEM OPERATING IN THE 220GHz-1.1THz RANGE	20
2.1 Introduction	20
2.2 System description	23
2.3 Working Mechanism of the Quasi-Optical system for polarization tuning	30
2.4 Test measurements to verify the system	35
2.4.1 Frequency dependent measurements	36
2.4.2 Temperature dependent measurements	37
2.4.3 Frequency sweep measurements	38
2.4.4 Sample rotation measurements	39
2.4.5 Polarization dependent measurements	41

2.5 Frequency extension plans	43
2.6 Conclusion	45
2.7 References.....	46
CHAPTER 3: LOW FREQUENCY SPECTROSCOPY OF 2D VAN DER WAALS ANTIFERROMAGNETIC TOPOLOGICAL INSULATOR $\text{MnBi}_2\text{Te}_4(\text{Bi}_2\text{Te}_3)_n$ FOR $n = 1$ AND 2	49
3.1 Introduction.....	49
3.2 Samples and the measurement set up.....	50
3.3 Results and discussion	54
3.3.1 Measurements on MnBi_4Te_7 sample.....	54
3.3.1.1 Field rotation measurements at low frequency	55
3.3.1.2 In plane measurements and corrugated sample plane	58
3.3.1.3 Temperature-dependent measurements.....	60
3.3.1.4 Frequency dependent measurements	62
3.3.1.5 Frequency dependent measurements at 4K.....	63
3.3.1.6 Field rotation measurements at high frequency	64
3.3.1.7 18GHz low temperature measurements on the MnBi_4Te_7	68
3.3.2 Measurements on the $\text{MnBi}_6\text{Te}_{10}$ sample.....	71
3.3.2.1 Field rotation measurements	71
3.3.2.2 Temperature-dependent measurements.....	72
3.3.2.3 Frequency dependent measurements	73
3.3.3 High temperature measurements in both samples.....	74
3.3.4 Comparative study at 7GHz between two different stoichiometric samples	75

3.4 Conclusion	76
3.5 References.....	78
CHAPTER 4: STABLE UNIVERSAL 1- AND 2-INPUT SINGLE-MOLECULE LOGIC GATES.....	81
4.1 Introduction.....	81
4.2 The SELC sample preparation	82
4.3 The SELC Design	86
4.4 Results and Discussion	88
4.4.1 Current map measurements and calculations	88
4.4.2 Working principle of the resettable SELC	93
4.4.3 Determination of the gate voltage range for the 1-input logic gates.....	95
4.4.4 SELC 1-input logic gates	97
4.4.5 Multi-cycle stability test for 2-input logic gates	99
4.4.6 SELC 2-input logic gates	102
4.4.7 Current maps measured at different scales.....	106
4.4.8 Measured differential conductance maps of different Fc-based molecular junctions.	109
4.4.9 Functionality comparison with conventional CMOS.....	110
4.4.10 Leaking Current of the SETs	112
4.4.11 Stability of SELC under magnetic field.....	113
4.5 Conclusion	115
4.6 References.....	117
APPENDIX A: DESIGN OF ANTENNAS OPERATING IN THE THZ GAP REGION	121

Study on spiral antennas	122
Study on bowtie-antennas	124
APPENDIX B: FABRICATION AND CHARACTERIZATION OF COPLANAR WAVEGUIDES AND STT-FMR DEVICES.....	129
Photolithography process.....	130
Sample preparation and spin coating	130
Mask-alignment, exposure, and development.....	131
Metallization and lift off	132
Device characterization.....	133

LIST OF FIGURES

Figure 1.1:Neel vector in a uniaxial AFM. Here, \mathbf{m}_A and \mathbf{m}_B denote two sublattices of a uniaxial AFM with magnetic moments pointing in opposite directions. The order parameter is given as \mathbf{l} in terms of both magnitude and direction..... 4

Figure 1.2: Schematic diagram of AFM based THz oscillator taken from a theoretical proposal by Khymin et. al. [3]. Charge current flowing through a high spin orbit coupling material, Pt in this case, produces a spin current via SHE and drives AFM into a dynamic mode by the spin current produced as a result of the SHE. When proper anisotropy criteria is met i.e. hard axis lying along the interface of the heterostructure, sustained oscillations of magnetic moments can be generated which give the THz signal. The THz signal in this case can be detected as an ac signal voltage by using the ISHE process as a result of back spin pumping from AFM to Pt. 7

Figure 1.3: Frequency tunability of proposed AFM based THz oscillator as a function of applied charge current density proposed theoretically by Khymin et. al. [3]. Blue and green vertical dashed lines represent two thresholds required for the operation of the proposed devices. The upper threshold is called the ignition threshold (blue dashed line) and the lower threshold is called elimination threshold (green dashed line). 8

Figure 2.1: A magnetic spectroscopic system..... 21

Figure 2.2: System description..... 25

Figure 2.3: An image of the fully installed operating system in del Barco lab at UCF showing different components of the system described in the figure 2.2. 27

Figure 2.4: Illustration of working mechanism of quasi-optical system..... 31

Figure 2.5: A Frequency vs field plot for the resonance position while applying field along the easy axis and the hard axis directions performed on sample1 at 12K. Dotted magenta lines are straight guidelines connecting resonance positions for field along easy axis. The zero-field resonance is observed at 257 GHz (see text for details). The inset shows a sample raw signal at 450GHz where

a signal extinction can be clearly seen across the resonance position. The center of this extinction region is taken as the position of resonance and the width of extinction is taken as the error. The green vertical dotted line at 9.54T represents the spin flop transition of MnF₂ which is just beyond the capacity of our maximum field limit, 9T. 36

Figure 2.6: Temperature dependent measurements performed on sample2 at 260GHz. The resonance positions at different measurement temperatures are plotted as a function of magnetic field. Different trends of slopes across transition temperature (67K) denote antiferromagnetic nature of the signal at lower temperatures and paramagnetic the signal at higher temperatures. The inset shows the raw spectrum obtained at different temperatures. The resonance position was taken as center of the extinction region and the width of extinction was taken as the error..... 38

Figure 2.7: Frequency sweep measurements done at fixed field values on sample2 at temperature 35K. Black, red, green and blue curves represent frequency sweeps at 0.00, 0.25, 0.75 and 1.00T respectively. Vertical lines of corresponding color represent resonance positions for that sweep.39

Figure 2.8: Angle rotation measurements done on sample 1 at 420GHz and 12K with sample alignment close to the easy axis. The resonance field positions are plotted against alignment angle relative to a reference line taken for the sample alignment. Center of the signal at the extinction region is taken as the resonance position and the width of the extinction is taken as the error. The raw spectrum is given in the inset. The resonance position has a minimum around -4° which represents the direction of the easy axis..... 40

Figure 2.9: MnF₂ sample (sample1) used in the angle rotation measurement for localization of easy axis. Bulk MnF₂ crystal was polished to smoothen down surface roughness to 2nm (rms) and 4nm Pt was deposited on top for next set of transport measurements..... 41

Figure 2.10: Results for polarization dependent measurements (A) shows polarization dependent measurements performed on sample1 at 240GHz and 12K for the case where both transmitter and receiver side are set at same type of polarization. Blue, green, red and black curves represent data taken when polarization of both sides was fixed at HP, CP1, VP and CP2 respectively. (B) shows

polarization dependent measurements performed on sample2 at 260GHz and 35K when the polarization of transmitter side was fixed at HP and that of receiver side was rotated around. Blue, green, red and black curves represent data taken when receiver side polarization was set at HP, CP1, VP and CP2 respectively.....42

Figure 2.11: A design showing the upgraded THz circuitry. The components to be added to the existing circuitry (shown in figure 1 (b)) is marked in green. In the figure (i), (ii) and (iii) represent the corrugated feed horn, a collimating parabolic mirror and a corrugated waveguide respectively. .44

Figure 3.1: Crystal structures of $\text{MnBi}_2\text{Te}_4(\text{Bi}_2\text{Te}_3)_n$ for $n = 0-2$. **(A)** and **(B)** respectively show the crystal structures of quintuple and the septuple layers which are the building blocks of the $\text{MnBi}_2\text{Te}_4(\text{Bi}_2\text{Te}_3)_n$ family. **(C)** shows the crystal structure of the parent compound MnBi_2Te_4 ($n=0$) where the individual septuple layers are stacked together in layers. **(D)** shows the crystal structure of MnBi_4Te_7 ($n=1$) compound where a non-magnetic quintuple layer is inserted between the two septuple layers of MnBi_2Te_4 . **(E)** shows the structure of $\text{MnBi}_6\text{Te}_{10}$ ($n=2$) compound where two non-magnetic septuple layer is inserted between the two layers of MnBi_2Te_4 . (Image source: J. Q. Yan et. al., Phys. Rev. Materials 4, 054202 (2020))..... 50

Figure 3.2:**(A)** A microscope image of an MnBi_4Te_7 single crystal used in the measurement. **(B)** A microscope image of a CPW mounted on a housing box where the two central lines of coaxial cable make connection to the central line of the CPW while the ground planes are grounded to the housing box using conductive silver paint. **(C)** An image of the Helium-3 cryostat used for the measurements. **(D)** An image showing the spectroscopic measurement set up in the lab where the cryostat shown in (C) is inserted in the magnet Dewar filled with liquid helium and a VNA is connected to the cryostat..... 52

Figure 3.3: **(A)** A sketch of a CPW with G-S-G configuration used in the measurement. The two ground planes are grounded while the central line on both sides connects to the central line of coaxials coming from the housing box. The sample sits on top of the highly sensitive constricted central region of the CPW. The chosen coordinate system with respect to the CPW is also shown. **(B)**

relative field orientation at the sample sitting on top of the CPW. A planar sample lies on the y-z plane of the chosen coordinate system with x-axis pointing out of the sample plane. z-axis represents the direction parallel to the flow of ac current. Angles θ and ϕ represent the polar angles for the direction of applied magnetic field \mathbf{H} in the chosen coordinate system..... 53

Figure 3.4: Results for the field rotation measurements performed on MnBi_4Te_7 at $T = 7\text{K}$ and $f = 7\text{GHz}$ frequency. A sample resonance signal is shown in the inset in (C). **(A)** A contour plot for the field rotation measurements performed along the x-y plane (OOP) direction where the angle values correspond to θ of the considered field orientation system. 0° and 90° on the contour correspond to the + x- and the + y- axis respectively and it continues to rotate in that way until coming back to the starting position. The two horizontal dotted lines passing through 85° and 265° represent angle positions corresponding to the maximum field position of the signal. **(B)** A plot for the resonance position as a function of field angle along the OOP direction defined by z-x plane i.e., θ rotation for ϕ fixed at 0° . 0° and 90° on the contour correspond to + z- and + x-axes respectively and it continues to rotate in that way until coming back to the starting position. The two horizontal dotted lines passing through 0° and 180° show angle positions corresponding to the maximum field position of the signal and represent the positions for applied field along the in-plane (IP) direction. **(C)** A contour plot for the field rotation measurements performed along the corrected IP direction (see the next section (3.3.1.2) for details) defined as a plane perpendicular to the easy axis defined by 88.5° and 355° for the values of θ and ϕ respectively. Angles 0° and 90° on the contour correspond to the corrected + z- and + y- axes of the newly defined sample plane respectively, and the rotation continues along the modified (-) y to + z to + y direction. The two vertical dotted lines represent the maximum and minimum field positions for the signal..... 55

Figure 3.5: **(A)** Contour plot for the in-plane (IP) field rotation measurement on MnBi_4Te_7 at 7GHz and 7K along the y-z plane of the considered coordinate system. In the plot 0° and 90° correspond to + z and +y axis respectively and rotation completes in that direction. **(B)** represent the contour plot

for the modified sample plane which is perpendicular to the easy axis defined by 80° and 355° for the angles θ and ϕ respectively. In the plot 0° and 90° correspond to modified + z and +y axis respectively and rotation completes in that direction of rotation. **(C)** A plot of the resonance positions of three different rotation angle values: 0° , 45° and 90° for different θ planes defined by the angles in the legend. In this graphic, the 90° curve corresponds to the field rotation in the z-x plane. **(D)** A plot of the θ plane angle vs the maximum modulation obtained from the rotations in plot (c). The θ value for the direction of the easy axis is given by the minimum field modulation plane i.e., 88.5° represented by the green dotted line. 58

Figure 3.6: Results from the temperature and the frequency dependent measurements are shown in upper and lower panels respectively. **(A)**, **(B)** and **(C)** represent the contour plots for the temperature dependent measurements performed at $f = 7\text{GHz}$ in the temperature range from 1K to 25K for the direction of the applied field along the x-, y- and z-axes respectively. The horizontal dotted lines in each of the plots correspond to the transition temperature for this material. 60

Figure 3.7: Results for the frequency dependent measurements performed at $T = 7\text{K}$. **(A)** A contour plot for the frequency dependence along the IP direction (y-axis) of the applied field. **(B)** A frequency vs field plot for the data corresponding to (a). **(C)** A frequency vs field plot for the frequency dependence along the OOP direction (x-axis) of the applied field. The errors in **(B)** and **(C)** are proportional to the width of the corresponding signals. 62

Figure 3.8: Results for the frequency dependent measurements performed on the MnBi_4Te_7 sample at 4K. **(A)** IP frequency dependence for the applied field along the y-axis of the considered coordinate system. **(B)** OOP frequency dependence for the applied field along the x-axis. The errors in both the data are proportional to the width of the corresponding signals. 64

Figure 3.9: Results for the field rotation measurements performed at $f = 18\text{GHz}$ and $T = 7\text{K}$. **(A)-(C)** represent the contour plots for the field rotations along the y-z, x-z and x-y planes respectively. In **(A)** the θ rotation is performed keeping ϕ at 90° from (-) y-axis (-90°) to +y-axis (90°) through +z-

axis (0°). In **(B)** the θ rotation is performed keeping ϕ at 0° from (-) x-axis (-90°) to +x-axis (90°) through +y-axis (0°). In **(C)** the ϕ rotation is performed keeping θ at 90° from +x-axis (0°) to (-) x-axis (180°) through +y-axis (0°)..... 65

Figure 3.10: Results for the temperature dependent measurements performed in the range 250mK to 25K at $f = 18\text{GHz}$ for the applied field along all three principal axes directions of the considered coordinate system. **(A)**-**(C)** respectively represent the contour plots for the applied field along x-, y-, and z-axes. 67

Figure 3.11: Field rotation measurements at 18GHz frequency and 4K temperature. In the figure, **(A)**, **(B)** and **(C)** represent the contour plots for the applied field along y-z, x-z and x-y planes respectively. In plot **(A)** the θ rotation is performed keeping ϕ at 90° from (-) y-axis (-90°) to + y-axis (90°) through + z-axis (0°). In plot **(B)** the θ rotation is performed keeping ϕ at 0° from (-) x-axis (-90°) to + x-axis (90°) through + y-axis (0°). In plot **(C)** the ϕ rotation is performed keeping θ at 90° from + x-axis (0°) to (-) x-axis (180°) through + y-axis (0°)..... 68

Figure 3.12: **(A)** contour plot for the field rotation measurement performed at 18GHz and 250mK along the y-z plane. In the measurement the θ rotation is performed keeping ϕ at 90° from (-) y-axis (-90°) to + y-axis (90°) through + z-axis (0°). **(B)** contour plot for the temperature dependent measurement performed at 18GHz in the range 1K to 25K in step of 1K while applying the field along -40° direction of plot (A). 70

Figure 3.13: Results for the field rotation measurements performed on the $\text{MnBi}_6\text{Te}_{10}$ sample at $f = 8\text{GHz}$ and $T = 7\text{K}$. In the figure, **(A)**-**(C)** represent the field rotation measurements the x-z, x-y and y-z planes of the considered coordinate system respectively. In **(A)** the θ rotation is performed keeping ϕ at 0° from (-) x-axis (-90°) to + x-axis (90°) through + z-axis (0°). In **(B)** the ϕ rotation is performed keeping θ at 90° from + x-axis (0°) to (-) x-axis (180°) through + y-axis (0°). In **(C)** the θ rotation is performed keeping ϕ at 90° from (-) y-axis (-90°) to + y-axis (90°) through + z-axis (0°)..... 71

Figure 3.14: Results for the temperature dependent measurements on $\text{MnBi}_6\text{Te}_{10}$ sample performed at $f = 8\text{GHz}$ in the range 1K to 25K . (A)-(C) represent the contour plots for the measurements with applied field along the x-, y- and z-axes, respectively. The horizontal dotted lines in each plot correspond to the transition temperature..... 72

Figure 3.15: Results for the frequency dependent measurements performed on $\text{MnBi}_6\text{Te}_{10}$ sample at $T = 7\text{K}$. (A) represents the data for the IP measurement for the direction of the applied field along the y-axis. (B) represents the data for the OOP measurement for the direction of the applied field along the x-axis. In both the plots the errors are proportional to the width of the corresponding signals. 74

Figure 3.16: Results for the frequency dependent measurements performed at 25K in both sample. Plots (A) and (B) represent the frequency dependent measurements for the MnBi_4Te_7 and $\text{MnBi}_6\text{Te}_{10}$ compounds respectively for the applied field along all three principal axes directions represented by different colors. The magenta lines are the arbitrary lines passing through the representative data of either compound and the origin. 75

Figure 3.17: Plots for the 7K and 7GHz OOP field rotation measurements along y-z plane performed on the two stoichiometric compounds. Plots (A) and (B) respectively represent the results for the MnBi_4Te_7 and the $\text{MnBi}_6\text{Te}_{10}$ compounds. In both the plots 0° , 90° and 180° represent the field direction along the +x-, +y, and (-) x-axis respectively. The two vertical dotted lines in each plot are straight lines passing through the maximum and the minimum signal position whose difference gives the strength of field modulation for each case..... 76

Figure 4.1: The SEM images for chip at different stages. (A) The pattern of the first two layers (the conducting-leads layers). (B) The third layer ($\text{Al}_2\text{O}_3/\text{Al}$ back-gate electrode) is deposited between the patterns formed by the first two layers. (C) The fourth and fifth layers (Au nanowires and Au nano-pads) are deposited on top of the first three layers. (D) The zoom- in picture shows the nanowire has been deposited on the back-gate electrode. The constricted part of the nanowire is 50nm wide and 15nm thick..... 83

Figure 4.2: The current feedback-controlled electromigration I-V curves of four nanowires that show the molecular conductance signal after breaking. (A) The blue curve is the electromigration curve of the nanowire at room temperature and pressure. The red curve is the electromigration curve at 4 K. For the whole electromigration processes, the starting resistance was 155 Ω , the middle state resistance was 13 K Ω , and the final breaking resistance was \sim 1 M Ω . The inset is the corresponding resistance of the low temperature electromigration process. (B) The electromigration processes in a second successful experiment. The resistance starts with 200 Ω and ends with \sim 4 M Ω . (C) The electromigration processes in a third successful experiment. The resistance starts with 150 Ω and ends with \sim 2 M Ω . (D) The electromigration processes in a fourth successful experiment. The resistance starts with 182 Ω and ends with \sim 3 M Ω . Five additional working SELC nanowire prototypes were found, giving a total yield of 9 from the total of 37 devices with these characteristic electromigration curves..... 86

Figure 4.3: The design of SELC. (A) Chemical structure and schematic of a S-(CH₂)₃-Fc-(CH₂)₉-S molecule bridging the nanogap between two nano-electrodes. (B) SEM image of a SELC showing the Au nanowire on the Al₂O₃/Al back-gate on a Si wafer and positions where V_b and V_g are applied. The nanowire and the back-gate were patterned by electron-beam and optical lithography, respectively [53]. The molecular junction formed in the center of the nanowire was produced using current feedback-controlled electromigration [15, 27, 46]. (C) Representative I-V_g curves for different values of V_b measured at 225 mK with 231 points per curve. The arrows mark the switch points of the current plateaus. The dashed lines indicate the V_g values corresponding to the seven I-V_b curves in (D). (D) Representative I-V_b curves for the seven different V_g values, with 231 points per curve. T = 225 mK. 88

Figure 4.4: The current modulation of SELC. 90

Figure 4.5: Logic calculation based on resonance excitations of MOs. (A) Measured 231 \times 231 points current map at 225 mK marked with logic operating voltage-ranges. A, A', A'', AA' and B, B', BB' are the voltage-ranges of input-gate and input-bias, respectively. White rectangles mark 2-input

logic operation areas. Input (1, 1) means high-gate and high-bias voltages, (0, 0) is the opposite case. Input (1, 0) means high-gate and low-bias voltages, (0, 1) is the opposite. **(B)** Differential conductance map corresponding to (A). Input AA'-BB' is an example to illustrate how gate (V_g) and bias (V_b) voltages are combined to achieve logic operations. The black arrow goes from (0, 0) to (1, 1), when V_g and V_b both change along the short green arrows. The yellow arrow goes from (0, 1) to (1, 0), when V_b and V_g change along the short orange and green arrows, respectively. **(C)** The schematic diagrams describe the energy level distributions of the four input cases in (B). Phase 0° and 180° correspond to the black and yellow arrow, respectively. **(D)** Equivalent logic circuit and truth table with AA'-BB' inputs at 0° and 180° phases. **(E and F)** show the curves of input V_g and V_b and measured output current at 0° and 180° , respectively. 94

Figure 4.6: The test to determine gate voltage range for the operation of 1-Input logics at 70 mV bias voltage, 225 mK. In **(A-F)**, the red curves are the input gate voltage signal, the high “1” gate voltages are about -2.0 V, the low “0” gate voltages are -1.67, -1.70, -1.71, -1.73, -1.79 and -1.82 V, respectively. The gray curves are the output current. The current values corresponding to the high gate voltages (“1”) are around 420 nA (“1”) marked by the blue arrows. While these marked by the green arrows are modulated by the low “0” gate voltages. The pink arrows on the left of each current curve indicate the Boolean “1” and “0” states of current, which is decided by whether the current value is higher than 300 nA. 97

Figure 4.7: Four resettable universal 1-input logic gates. In **(A and D)**, input gate voltages with A, A', AA' and A'' ranges are marked on the current maps, which indicate 1-input “YES”, “NOT”, “PASS 1” and “PASS 0” logic gates. **(B)** Equivalent circuit, truth table and corresponding Input/Output signal for 1-input “YES” gate. With the gate voltage change from -2.02 V '1' to -1.82 V '0', the current changes from 410 nA '1' to 120 nA '0'. **(C)** For 1-input “NOT” gate, with gate voltage change from -1.82 V '1' to -1.67 V '0', the current changes from 120 nA '0' to 405 nA '1'. **(E)** For 1-input “PASS 1” gate, with the gate voltage change from -2.02 V '1' to -1.67 V '0', the current changes from 410 nA '1' to 405 nA '1'. The frequency of the current signal is doubled compared with the input gate

signal. (F) For 1-input “PASS 0” gate, with the gate voltage change from -1.82 V '1' to -1.77 V '0', the current changes from 120 nA '0' to 130 nA '0'. All 1-Input logic gates operate at 70 mV bias.

..... 99

Figure 4.8: The multi-cycle repeatable test for 2-input logic gates at $T = 225$ mK. (A) The truth table for the logic gates. The color frames corresponding to different logic gates shown at (B-H), respectively. The long black and yellow frames indicate the bias signal and gate signal with same phase and with 180° phase, respectively. (B-H) are the logical operation regions marked on the current color map for different logic gates. The input and output signals are shown on the right. The black arrow and yellow arrow in the color map represent the 0° and 180° phase difference between the input bias and gate signals, respectively. The starting point and ending point of the arrows determine the voltages changing range and mark the corresponding output current states. (Red color is the “on” state of the current and blue color is the “off” state)..... 100

Figure 4.9: The 37-cycle repeatable curves for AA'-B at 0° and 180° phase, 225 mK..... 101

Figure 4.10: AA'-B curves with different points at 0° and 180° phases, 225 mK. (A) The AA'-B curve at 0° phase with 40 points per cycle. (B) The AA'-B curve at 180° phase with 40 points per cycle. (C) The AA'-B curve at 0° phase with 4 points per cycle. (D) The AA'-B curve at 180° phase with 4 points per cycle. 102

Figure 4.11: Seven resettable universal 2-Input logic gates. (A and B) “AND” and “INH” logic gates with A-B' and A'-B' inputs in both phases, respectively. The black and yellow arrows in current map are corresponding to the Input/Output signals in 0° phase and 180° phase, respectively. (C) “XOR” logic gate with A'-BB' input in 0° phase and AA'-B input in 180° phase. The input gate voltages in both phases have the same minimum value and the input bias voltages in both phases have the same maximum value, i.e., the (0,1) point is the same in the voltage ranges in both phases. The highest gate voltage and the lowest bias voltage (i.e., the (1,0) point) from 0° phase to 180° phase is changed. (D) “XNOR” logic gate with AA'-B input in 0° phase and A-BB' input in 180° phase. The input gate and bias voltages in both phases have the same maximum value, i.e., the (1,1) point

is the same in the voltage ranges in both phases. The lowest gate voltage and the lowest bias voltage (i.e., the (0,0) point) from 180° phase to 0° phase is changed. **(E, F and G)** “NAND”, “NOR” and “OR” logic gates have the same input bias voltage range in both phases and change the gate voltage range with phase only. “NAND” has A’-B input in 0° phase and AA’-B input in 180° phase. “NOR” has A’-B input in 0° phase and A’’-B input in 180° phase. “OR” has A-B input in 0° phase and AA’-B input in 180° phase. 105

Figure 4.12: The measured 231×231 points current maps for different voltage ranges at 225 mK and the energy shift caused by slight conformational changes of the molecule under high gate voltage fields calculated by DFT. **(A)** The whole scan for ϵ_2 and ϵ_1 , which represent the resonance regimes contributed by the conductive MOs. **(B)** and **(C)** are the zoom-in scans of the voltage ranges within the yellow frame marked in **(A)**. The gate voltages for the crossing points of ϵ_1 at **(A)**, **(B)** and **(C)** maps are 1.71 V, 1.67 V and 1.64 V, respectively. ν' and ν'' indicate the edges between the resonant regime of ϵ_1 and the Coulomb blockade regions. **(D)** is the 101×142 points theoretical conductance map, taking into account the -15 meV energy shift due to slight conformational changes of the molecule when the gate voltage is higher than -2.2 V. **(E)** is the energy evolution of the two adjacent conductive MOs ϵ_1 and ϵ_2 along the gate voltage field. **(F)** indicates the slight conformational changes under different gate voltage fields. The calculations were performed in Gaussian package [56] with the B3LYP functional and LANL2DZ basis set. 108

Figure 4.13: The measured differential conductance maps for different Fc-based molecular SETs with 0 to 100 mV bias voltage at T = 4.2 K. **(A)** The map for Au/S-(CH₂)₄-Fc-(CH₂)₄-S/Au molecular junction [27]. **(B)** The map for Au/S-(CH₂)₆-Fc-(CH₂)₆-S/Au molecular junction (the electromigration curve see Sample-O6, Figure S3). **(C)** The map for Au/S-DPA-CH₂-Fc-(CH₂)₂-S/Au molecular junction [23]. **(D)** The map for Au/S-DPA-Fc-(CH₂)₂-S/Au molecular junction [23]..... 110

Figure 4.14: Comparing the functionality of CMOS and SELC by building all universal logic gates. **(A)** The three basic logic gates “NOT”, “NAND” and “NOR” as obtained by CMOS. The number in

each rectangular box is the number of CMOS components used in the logic gate. V_{dd} , V_{OUT} and V_G indicate the bias, output and gate (input) voltages of CMOS, respectively. I indicates the charging current. CL is the load capacitor. **(B)** The five universal logic gates “OR”, “XNOR”, “AND”, “INH” and “XOR” consist of the three basic logic gates in (A) and can therefore be constructed by CMOS. The number of CMOS components is marked in each box. Both A and B are the input gate voltages, C is the output voltage. **(C)** By controlling the range of input voltages (A: gate voltage V_g and B: bias voltage V_b) separately, SELC can create all the universal logic gates by switching the output current (C: I) through a single molecular junction. 111

Figure 4.15: Current measured through the Al_2O_3 layers of SETs at 4 K when biasing the gate. Black arrows indicate gate voltage, where the average tunneling currents for samples 1 to 4 are below 0.1 nA..... 112

Figure 4.16: Conductance maps measured under magnetic fields and the spin-polarized transmission spectra calculated by DFT. **(A)** and **(B)** are 231×231 points conductance maps measured at 225 mK under 0 T and 1 T magnetic fields, respectively. **(C)** and **(D)** are 151×151 points conductance maps for a small voltage range at 225 mK under 0 T and 1 T magnetic fields, respectively. **(E)** is a comparison of the spin-polarized Ts and unpolarized Ts of the optimized tip-to-tip molecular junction at 0 V bias. 115

Figure A. 1: **(A)** A center part of a spiral antenna showing a small sample region and the direction of high-density dc current flow. **(B)** A spiral antenna with feed lines on the left and the right-side. **(C)** Angular distribution of the radiation pattern at different frequencies across the studied spiral antennas. Blue, green, red and cyan curves represent emission patterns for 500, 1000, 1500 and 2000GHz antennas respectively. The black line at the center connecting 90° and 270° separates the substrate from the air. **(D)**A THz current distribution in the spiral antenna operational at 1.5THz. **(E)**A 2D plot for the radiation intensity for 1.5THz antenna across a direction perpendicular to the

antenna. The plane at 0 micron in the vertical direction separates the substate (lower) and the air (upper) regions. **(F)**A 3D plot for the radiation distribution for a 1.5THz antenna. 123

Figure A.2: **(A)** Design of a bowtie antenna on MnF₂ substrate with feed lines passing through the center of bows along the length of the antenna. The sample region is shown as the Pt center area where AFM sample will sit on top of Pt or any other high spin orbit coupling material. **(B)** Emission intensity plot across the antenna and the feed lines for an antenna in (A) with resonance frequency 1.5THz and length 20 μm **(C)**Angular distribution of the emission pattern for a set of 1.5 THz antennas with different bowtie lengths shown by color code. 124

Figure A. 3: **(A)** A design of slightly different bowtie antenna on the MnF₂ substrate where feed lines pass through the opposite side of the flat edge of the bows. **(B)** Emission intensity plot for the type of antenna shown in (A) with a resonant frequency 1.5THz and length 40μm. Inset of (B) shows the emission intensity across a plane perpendicular to the direction of the bowtie and passing through its center. 125

Figure A. 4(A): A design of a bowtie antenna on a MgF₂ substrate where the feed lines are transversal to the bowtie and enter through the opposite corners of the bows in the opposite directions. **(B)** Emission intensity plot for the design of the bowtie shown in (A) with resonant frequency 1.5THz. Inset of (B) shows the transverse view of the emission of the antenna across a plane perpendicular to and passing through the center of the bowtie. 126

Figure A. 5: **(A)** A plot of calculated bowtie lengths for different frequencies at a 30° flare angle for the optimized antenna geometry. **(B)** The flare angle dependence of resonance linewidth for a 1.5THz bowtie antenna with the optimized geometry for the feedlines. 127

Figure A. 6: **(A)** Optimized geometry of single bowtie antenna which will be used for the emission/absorption of linearly polarized radiation. The magnetic sample will sit at the center of the bowtie in the constricted region (shown in orange color) **(B)** Two crossed bowtie which will be

used for the emission/absorption of circularly polarized radiation. The magnetic sample will sit at the cross section of two bowties. 128

Figure A. 7: Microscope images of fabricated devices. **(A)** An image of a CPW fabricated by single step photolithography process. **(B)** An image of a STT-FMR device fabricated by using two step photolithography process. The inset shows the magnified view of the constricted sample region where a $15\mu\text{m}\times 25\mu\text{m}$ Pt/Py sample in the gap region is connected to the two ends of the central line of the CPW..... 133

Figure A. 8: **(A)** Microwave transmission through a CPW from 10MHz to 50GHz under different conditions. The purple curve denotes the transmission through the sample in a housing box at the room temperature. The olive and blue curves respectively represent the transmission at room temperature and low temperature when the housing box with the CPW in (A) is put inside a cryostat. **(B)** Room temperature microwave transmission through two STT-FMR devices of different sample sizes in the frequency range 10MHz to 20GHz. 134

LIST OF TABLES

Table 1.1: Different AFMs with their Neel Temperatures and resonance frequencies which are of interest for our study on high frequency spintronics	11
Table 2.1: Installed HFM frequency bands and the available average output power level in each band...	28

LIST OF ABBREVIATIONS

- 2D: Two dimensional
- AFM: Antiferromagnet
- AFMR: Antiferromagnetic Resonance
- CFM: Cryo-Free Magnet
- CP: Circular Polarization
- DFT: Density Functional Theory
- EPR: Electron Paramagnetic Resonance
- EM: electromagnetic
- FM: Ferromagnet
- FMR: Ferromagnetic Resonance
- HFM: High Frequency Microwave
- HOMO: Highest Occupied Molecular Orbital
- HP: Horizontal Polarization
- ISHE: Inverse Spin Hall Effect
- MO: Molecular Orbital
- M-P: Martin-Puplett
- MURI: Multi University Research Initiative
- NM: Non-Magnet
- NMR: Nuclear Magnetic Resonance
- RIE: Reactive Ion Etcher
- SAM: Self Assembled Monolayer
- SET: Single Electron Transistor
- SAX: Signal Analyzer Extension

SELC: Single Electron Logic Calculator

SEM: Scanning Electron Microscope

SGX: Signal Generator Extender

SHE: Spin Hall Effect

SHNO: Spin Hall Nano-Oscillator

THz: Terahertz

TI: Topological Insulators

VDI: Virginia Diodes Incorporation

VNA: Vector Network Analyzer

VP: Vertical Polarization

VTC: Variable Temperature Cryostat

CHAPTER 1: INTRODUCTION

1.1 Background

Most of the research activities conducted in this thesis are part of a large collaborative Multi-University Research Initiative (MURI) project to study Terahertz (THz) spintronics with Antiferromagnetic insulators where the focus is to address the so-called “THz gap” in the spectrum of electromagnetic (EM) waves [1]. The THz gap refers to the existence of significant technical challenges in generating, detecting, and processing signals in the frequency range from 0.01 to 10 THz. The existence of this gap is hindering the advancement of several technologies, e.g., it is preventing communication technology and microelectronic memory devices from operating at THz speeds. The THz operative devices would enable three orders of magnitude faster technologies compared to the currently existing GHz technologies. Practical realization of easily operable devices operating in the THz gap region would bring much faster technologies like communication and computation from which society would benefit. A reliable THz technology could also be implemented in numerous other fields, including security, non-destructive testing, and medicine.

There exist several approaches, such as quantum cascade lasers, superconducting Josephson junctions, superconducting mesas, and free electron lasers which aim at addressing the THz gap. But these methods involve either a complex and bulky set up or require a cryogenic environment and a high voltage to operate, limiting their feasibility in terms of practical applications. To bypass these limitations there is a big push to use magnetic materials as active device components for generation, manipulation, and detection of THz signals [2-10].

Currently, active components in magnetic devices are made from ferromagnets (FMs) owing to their easy manipulation and addressability arising from the non-zero ground state magnetic moment. But the ferromagnetic dynamics governing the operational speed of these devices lie in the low end of the GHz range, limiting their operational speed to nanoseconds. Indeed, there already exist FM-based Spin Hall

Nano-Oscillators (SHNO) which act as nanoscale GHz signal sources. These SHNOs are simple to use but lack in terms of efficiency, high frequency and power level which decreases drastically with increase in frequency [11-13]. Unlike FMs, whose GHz dynamics depend on an applied field bias (H_{ext}) and a dipolar dominant anisotropy field (H_A), antiferromagnets (AFMs) present three orders of magnitude faster spin dynamics (in the THz range) originating from the combination of a relatively weak anisotropy field (H_a) and an extremely strong internal exchange interaction field (H_E). The resonant modes of FMs and AFMs arising from their magnetic dynamics are given by equations (1) and (2),

$$\omega_{FM} = \gamma\sqrt{H_{ext}H_A} \quad (1)$$

$$\omega_{AFM} = \gamma\sqrt{H_E H_a} \quad (2)$$

In these equations, ω_{FM} and ω_{AFM} represent the resonant frequencies for FMs and AFMs, respectively, in terms of angular units, where γ is a constant called gyromagnetic ratio whose value varies slightly from system to system. The major difference between these two equations is the presence of an extremely strong exchange field term in equation (2) whose value lies in the order of a thousand Tesla in typical AFMs based on fluorides, e.g., MnF_2 and FeF_2 , and oxides, e.g., Cr_2O_3 and Fe_2O_3 . The existence of this extremely strong internal exchange field uplifts the dynamics of AFMs up to the THz frequency range. This so-called “*exchange amplification*” allows for the control of AFM dynamics with relatively small spin currents [10], making AFMs a natural choice for active elements in high frequency devices operating in the THz range [2-4]. In this scenario, the study and use of the unique properties of high frequency THz dynamics in antiferromagnets (AFMs) provides an opportunity to transform methods of generation, transmission, and processing of THz signals and achieve next generation technological goals.

AFMs exist in different electronic states including metallic, semiconducting, and insulating as well as in the form of recently evolving exotic materials like topological insulators. In addition to the normal bulk AFMs, there are two-dimensional (2D) AFMs which can be exfoliated into thin sheets down to a single atomic layer. AFMs possess a variety of crystal structures and are naturally more abundant than their

counterparts, FMs. AFM materials have been known for a long time but neglected in terms of practical applications as active device components. Currently they are mainly used as a pinning layer to fix the orientation of FMs via exchange bias in memory devices and read heads of hard disc drives. They used to be considered materials with interesting properties in terms of a theoretical viewpoint but useless in terms of practical applications as explained in 1970 Nobel Lecture by Louis Neel [14] who got his Nobel Prize for his foundational work in AFMs and FMs. However, with the rapid developments in the field of spintronics in the recent few decades good progress has been made in understanding the physical mechanisms governing AFM dynamics both theoretically [2-4, 6, 15-17] and experimentally [7, 10, 18-21], and numerous potential practical applications have been suggested [16, 17, 21-24]. These studies suggest methods to harness the magnetic state of AFMs and their dynamics by applying different external stimuli, e.g., pure spin current [2, 3, 10, 21] and circularly polarized microwave stimuli [20, 25], among others. The excited high frequency AFM dynamics can be used in THz devices for signal generation [2-5] and detection [6, 9], in magnetic memory devices as ultrafast switching units [10, 21], and in neuromorphic devices which could mimic the functionality of the human brain at operating speeds down to a single picosecond time [26].

In the absence of an external magnetic field (\mathbf{H}) and below their Neel temperatures (T_N), AFMs have a long-range magnetic order with zero net magnetization. The existence of this zero net magnetization makes it difficult to manipulate and control the magnetic state of AFMs (i.e., is difficult to read a non-magnetic bit). On the other hand, this zero net magnetization in AFMs produces no stray fields (contrary to FMs) and gives the possibility of packing AFM device elements much closer than with their FM counterparts, while still operating independently without crosstalk, leading to an ultimately ultrahigh density for magnetic storage. This zero net magnetization gives extra stability to the AFM devices and makes it possible to operate them in extreme conditions of EM radiation, e.g., in the outer space and in regions of strong magnetic fields.

AFMs are described by an order parameter called the Neel vector (\mathbf{l}) which dictates their dynamics. For simple AFMs with two sublattices having sublattice magnetization vectors \mathbf{m}_A and \mathbf{m}_B , the Neel vector is the vector difference $\mathbf{l} = \mathbf{m}_A - \mathbf{m}_B$ between these two sublattices as shown in Fig. 1.1.

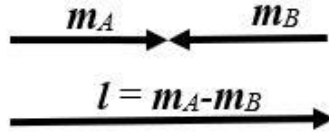


Figure 1.1: Neel vector in a uniaxial AFM. Here, \mathbf{m}_A and \mathbf{m}_B denote two sublattices of a uniaxial AFM with magnetic moments pointing in opposite directions. The order parameter is given as \mathbf{l} in terms of both magnitude and direction.

AFMs are broadly classified into two types: collinear and non-collinear AFMs, based on the alignment of magnetic moments within the magnetic crystals. In collinear AFMs, like MnF_2 , the magnetic moments are aligned in one direction, whereas in non-collinear AFMs, like Mn_5Si_3 , the magnetic moments point in different directions in both the in plane as well as in the out of plane directions [27]. AFMs can also be classified into different types based on the type of anisotropy they possess, e.g., easy axis AFMs, biaxial AFMs, easy plane AFMs, and other more complex magnetic organizations leading to a zero-net magnetization. In easy axis AFMs there is one preferred magneto-crystalline axis called the easy axis for the orientation of the magnetic moments or the Neel vector. MnF_2 , FeF_2 and Cr_2O_3 are examples of easy axis AFMs. An axis perpendicular to the easy axis where the magnetic moments do not remain stable under normal conditions is called the hard axis. The dynamics of these AFMs is governed by a convolution of the easy axis anisotropy and the exchange interactions. These easy axis AFMs have degenerate magnon modes with opposite chiralities that can be manipulated by circularly polarized EM stimuli, electron spin currents, and DC magnetic fields. The zero-field degenerate mode of easy axis AFMs range practically from 160GHz in Cr_2O_3 to 1.5THz in FeF_2 , enabling the possibility to study different magnetic effects over a wide range of frequencies in a similar type of systems. The degenerate mode is lifted by the application of a DC magnetic field and with increasing field the two branches with opposite chirality will move towards

opposite directions in frequency [28]. The upper (lower) branch is called the right (left) circularly polarized mode which can be excited by using EM stimuli of the corresponding circular polarization handedness [20].

In biaxial AFMs there is an easy axis and a hard axis, and in this case the magnetic dynamics depend on both the easy axis as well as the hard axis anisotropy. NiO is a well-known biaxial AFM. In easy plane AFMs the magnetic moments lie in specific crystallographic planes. In some of these easy plane AFMs, like NiF₂ and α -Fe₂O₃, the presence of the Dzyaloshinskii-Moriya interaction (DMI) causes the magnetic moments to tilt a small degree out from the easy plane resulting on a finite static magnetic moment in the ground state [29, 30]. As a result, easy plane AFMs have usually both ferromagnetic and AFM magnon modes. Because of the presence of a finite static magnetic moment, these AFMs give rise to the possibility of controlling their dynamics in a way which is not possible in AFMs with zero net magnetization [4].

In addition to these simple AFMs where the magnetic moments point either along a particular axis or along a particular plane, there are complex AFMs where the alignment of magnetic moments is more complicated. Examples of these complex AFMs include Mn₃Sn, where the magnetic moments lie antiferromagnetically in a triangular geometry [31], and Mn₅Si₃, where the magnetic moments lie both in plane as well as in the out of plane direction [27] but still giving a zero net magnetic moment in the ground state.

AFMs can also be classified into different types based on their conductive nature. There are metallic AFMs, like Mn₂Au, CuMnAs and Mn₃Au, where conduction happens through free charge carriers as in normal metals. There are insulating AFMs, mostly oxides e.g., NiO and halides e.g., MnF₂, which are insulating in nature but are of great interest because of their potential to carry chargeless spin waves called magnons. This dissertation and its umbrella project, the AFOSR MURI project, focus on insulating AFMs. Compared to metallic AFMs, where charge transport leads to a large dissipation, insulating AFMs present extremely low damping [18], enabling a clean manifestation of their magnetic quantum properties and long distance pure spin transport through magnons in the absence of charge motion [19]. This makes insulating

AFMs a natural choice for the realization of practical nano-scale technological devices operating with low power consumption and minimum energy loss.

There are several theoretical ideas put forward for the realization of AFM based THz oscillators and the detectors [2-5]. All of these proposals rely on the fact that a high density charge current flowing through a non-magnetic (NM) material with high spin orbit coupling gets converted into spin current by a process called the Spin Hall effect (SHE), which drives the magnetization dynamics in the adjacent AFM layer of an AFM/NM heterostructure as a result of spin transfer torque, as shown in Fig. 1.2. When the charge current density is strong enough to overcome the magnetization damping of the AFM material, the anti-damping torque generates sustained oscillations of the magnetic moments whose frequency depend on the eigen mode of the AFM used and/or the strength of the input spin current. Several methods are suggested for the detection of the generated THz signal. Cheng et. al. [2] and Khymyn et. al. [3] propose the use of the Inverse Spin Hall Effect (ISHE) [32] as a potential method to detect the signal while Sulymenko et. al. [5] propose the use of an AFM based magnetic tunnel junction. Another study by Sulymenko et. al. [4], on signal sources based on canted AFMs, suggests the use of different types of resonators for the free space irradiation of the generated high frequency signal which can be detected by THz detectors.

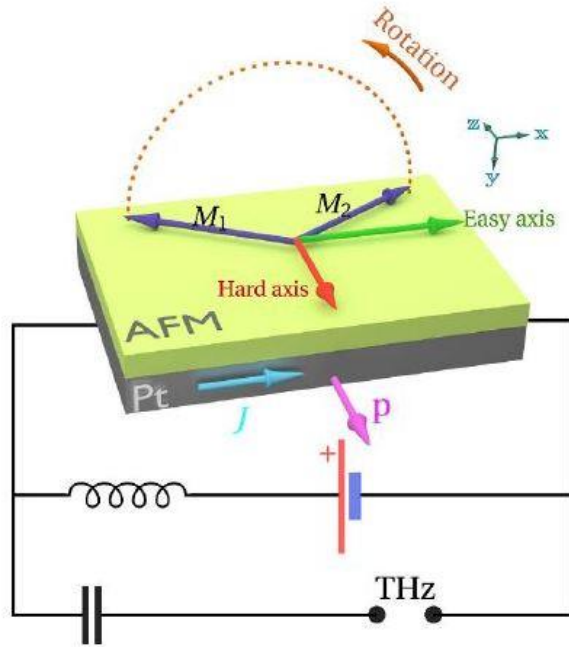


Figure 1.2: Schematic diagram of AFM based THz oscillator taken from a theoretical proposal by Khymin et. al. [3]. Charge current flowing through a high spin orbit coupling material, Pt in this case, produces a spin current via SHE and drives AFM into a dynamic mode by the spin current produced as a result of the SHE. When proper anisotropy criteria is met i.e. hard axis lying along the interface of the heterostructure, sustained oscillations of magnetic moments can be generated which give the THz signal. The THz signal in this case can be detected as an ac signal voltage by using the ISHE process as a result of back spin pumping from AFM to Pt.

While the major goal our project is to study high frequency insulating AFMs for the realization of potential AFM based THz oscillators and detectors, there is a long way to go before one can achieve this due to several technical challenges along the way. There are many challenging initial and intermediate experiments to be performed before being in the position to perform experiments which realize AFM based THz devices as suggested theoretically [2-6, 9, 15]. The first step towards this goal is to find the right material candidate which can be grown as a thin film and meets the theoretical anisotropy requirements. The major challenge for this step is obtaining the required out of plane anisotropy in the magnetic material of the heterostructures, with the Neel vector along the out of plane direction i.e., the hard axis along the interface as shown in Fig. 1.2. This is not possible in conventional insulating AFMs as they tend to grow

with in plane anisotropy. We have been working with different AFMs and their heterostructures to characterize them for their potential use in THz oscillators and detectors while overcoming this challenge.

Another challenge towards this goal is the requirement of high charge current density, in the order of 10^8 A/cm² [3], which must flow through a NM material with high spin orbit coupling in order to generate a sizeable amount of spin current at the interface with the AFM, as well as an efficient means to transfer the stimuli across the interface and into the whole AFM layer. Pt and Ta are natural choices for the NM material, but they cannot withstand such high charge current densities. Even though the proposed AFM based THz oscillators are supposed to be frequency tunable with applied charge current density, as shown in Fig. 1.3; the requirement of such current density beyond the normal limit adds additional challenges for the experimental realization of such devices. Therefore, alternative materials with higher efficiency in interconverting charge current into spin current are required.

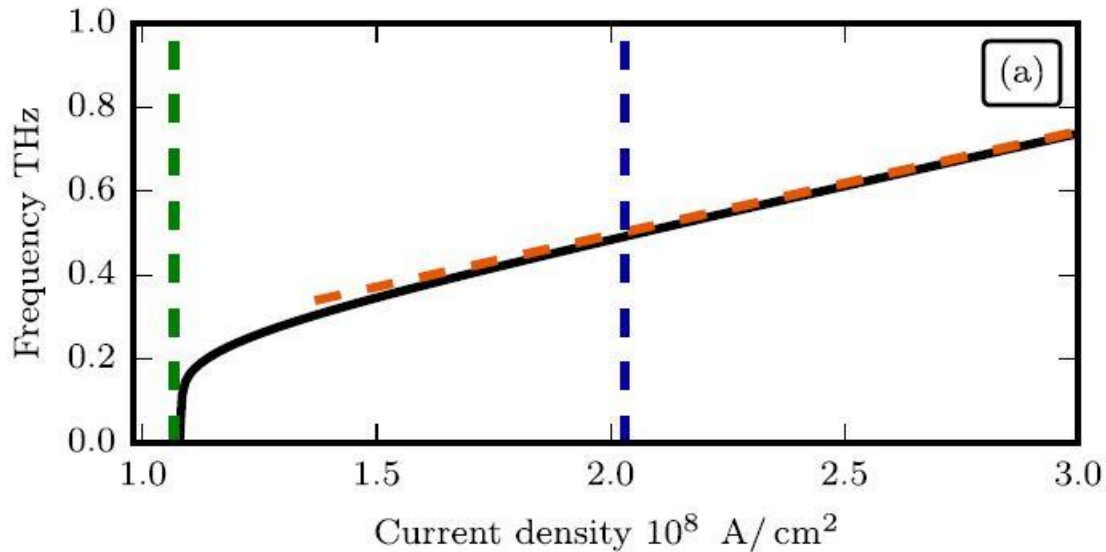


Figure 1.3: Frequency tunability of proposed AFM based THz oscillator as a function of applied charge current density proposed theoretically by Khymin et. al. [3]. Blue and green vertical dashed lines represent two thresholds required for the operation of the proposed devices. The upper threshold is called the ignition threshold (blue dashed line) and the lower threshold is called elimination threshold (green dashed line).

We are investigating different options to find the best possible candidate for this by performing several spin-charge interconversion experiments, called spin pumping experiments, with different AFM/NM heterostructures. We are also intending to address this issue by using other exotic material options like topological insulators (TIs) which are supposed to be much more efficient in generating spin current via SHE [33, 34].

Once the right heterostructure consisting of AFM/NM which meets all required properties is characterized, one still needs to make the appropriate monodomain AFM devices and perform the experiments at frequencies in a range difficult to work with in experiments. Fabrication of devices depends on the detection mechanism chosen to detect the THz signal. As discussed earlier, there are different theoretical proposals for signal detection, so it is still not clear which device would work best for this. In our case we are approaching this issue in a slightly different way. We intend to use bowtie antennae for the detection mechanism [35]. Instead of using a normal Pt stripe, a bow tie antenna will be patterned on top of the magnetic material to be used in the THz device. The bow tie antenna will help to increase the current density required to drive AFM into dynamics as well as to convert the generated sustained oscillations into free space radiation by concentrating the generated electric field in the device. We also intend to use the bowtie antennae to detect the expected dc signal from the ISHE measurements while irradiating the sample with a HFM signal and applying a dc bias at the same time. In this case the bowtie antenna will concentrate the applied HFM radiation to a small region of the sample thereby increasing the microwave power intensity. When the spin torque coming from the spin current originating from the dc bias is sufficient and is of the right orientation, it can reduce the damping of the system thereby reducing the linewidth of observed signal. The linewidth decreases gradually with increase in dc bias, and a zero linewidth indicates the onset of self-sustained oscillation. This experiment can confirm whether it will be possible to realize the self-sustained oscillations in AFMs by using spin current. For this we have studied different types of bowtie antennas and calculated the geometrical antenna parameters considering the proper working range of our interest. The detailed explanation on the antennae study is given in appendix A.

In summary, a collective collaborative effort in terms of material growth, characterization and device development is moving forward with the final goal of realizing the AFM based THz oscillators and detectors. While there are big final goals of the project, all these initial and intermediate steps are also equally important, and each step add to the knowledge of scientific community in each step.

We are interested in studying several insulating AFMs which have natural dynamics in the THz range. Table 1.1 outlines different insulating AFMs, with their Neel temperature and resonant frequencies, which are of interest for our study.

It can be seen from the table that most of these AFMs have sub-THz and THz dynamics. A study of these materials for their potential use in THz devices and other applications first requires a detailed spectroscopic study to understand their dynamics. As mentioned in the beginning, this frequency range lies in the THz gap, where it is difficult to work due to unavailability of research facilities which work in this frequency range. Many research labs have capabilities to work up to 50GHz using Vector Network Analyzers (VNAs), and the working frequency can be extended to around 100GHz by using frequency extension method which uses some external extension modules, available in our lab as well. Working in frequencies above 100GHz becomes more and more challenging as there are only a few facilities in the world where a few frequencies in the THz gap region are available. The National High Magnetic Field Lab (NHMFL) in Tallahassee has one such facility where we can work at 120GHz, 220GHz, 336GHz, 395GHz and a few other more discrete frequencies [36] . There are some facilities in Europe and other parts of the USA as well, but their operational range of frequency is limited to a few narrow bands within the range of our interest [37]. Moreover, it takes longer times, in general, to complete a project in such facilities where we get limited time to perform experiments at a time and usually there is a long waiting period before we could get our turn. It is best to have one such facility within a big collaboration like the MURI project for the study of antiferromagnetic insulators, to meet demanding requirements of the project in a timely manner. For this, we have developed a state-of-the-art high frequency instrumentation in our lab at UCF which forms the

next topic for discussion in this chapter, as I have taken full responsibility in its design and assembly as part of my dissertation activities.

Table 1.1: Different AFMs with their Neel Temperatures and resonance frequencies which are of interest for our study on high frequency spintronics

AFMs	Neel Temperature (K)	Resonance Frequency
MnF ₂	67.0	261 GHz
FeF ₂	78.4	1.5 THz
NiF ₂	73.2	100 GHz and 932 GHz
CoF ₂	37.8	854 GHz and 1079 GHz
FeCl ₂	23.5	489 GHz
CoCl ₂	24.7	575 GHz
MnO	122.0	70 GHz
CoO	291.0	4.5 THz and 6.5 THz
NiO	523.0	140GHz and 1.1 THz
α -Fe ₂ O ₃	948.0	170 GHz
Cr ₂ O ₃	308.0	165 GHz
MnBi ₂ Te ₄	24.0	108 GHz

1.2 High frequency instrumentation

We have developed a unique high frequency spectroscopy system in our lab at UCF capable of working from 220GHz to 1.1THz in a magnetic field up to 9T at temperature range from 5K to 300K. In our knowledge, there is no system in the world capable of working in this frequency range with continuous frequency tunability. In addition, this system also has a capability of tuning the polarization of high frequency microwave (HFM) signals of any frequency in the range from linear polarization to circular to elliptical and so on in a continuous manner. The system components were chosen in a way that we could cover the maximum frequency range of our need while remaining within a limited budget. This system

allows us to work on our AFM project on an effective basis to meet the demanding goals of the project. We also have provision to expand this frequency range to cover from 60GHz to 1.5THz continuous frequency with the polarization tunability which will open further research opportunities for different material systems.

This system consists of a 9T split coil cryofree magnet (CFM) and a rebuilt cryofree variable temperature cryostat (VTC) capable of working from 5K to 300K. This work involving the low temperature side of the system was done by Cryogenic Ltd, a UK based company. Cryofree route was chosen considering frequent Helium shortages [38] in the market which is affecting research activities involving liquid Helium as a cryogenic liquid to cool down the sample to low temperatures as well as to operate high magnetic field superconducting magnets. In such a scenario, having a cryofree system allows for continuous run of experiments, without having to worry about the supply of liquid helium, provided there is electricity (with proper power requirement) to run the Helium compressors which cool down the CFM and the VTC in a closed cycle cooling mechanism. Moreover, this system doesn't involve any cryogenic liquid and users are not directly exposed to cryogenic temperatures, so it is safer to use compared to the ones involving cryogenic liquid. The working mechanism of the cooling system is just flip switch method. This means once the operating switch is turned ON, in a certain time the system will cool down to designated operating temperatures to perform experiments and once the switch is turned OFF at the end of the experiment it will warm up to room temperature where we can open the cryostat and change the sample if necessary.

In addition to the magnet-cryostat system, the system also involves high frequency quasi-optical system to work in the designated frequency range. This quasi-optical system consists of a circuit involving many metallic blocks and wire grids which guides the HFM from the transmitter side of the system to the receiver side and rotates the polarization of the HFM as needed independently on either side. This system collimates and focuses the HFM beam to the sample position and collects the beam coming out from the sample for its detection. This part of the system was built by Thomas Keating Ltd., a UK based company with specialization in HFM components.

The HFM signal is generated and detected by using instruments from Virginia Diode Inc. (VDI), a USA based company working on high HFM source and detectors. A pre-existing hp sweep oscillator in the lab is used to drive the base module of VDI's high frequency signal generation scheme and several other multipliers are used to cover the entire frequency range of the system. VDI's signal analyzer modules are used to detect the HFM signal which is down converted and fed to a state-of-the-art spectrum analyzer for analysis.

All these components, HFM source and detector together with the quasi-optical system are properly integrated and aligned with the CFM and VTC of the system making one big integrated system allowing us to perform cutting-edge research experiments involving HFM in our own lab.

Initial discussions about this system started in 2019 when we learned that the MURI project for study on THz spintronics using insulating AFMs would be funded to the team led by my advisor. Even though we had an idea on what needed to do experimentally and what type of system was required for this, we had no clue about which companies work in those field and could potentially work with us. I, as a graduate student, started to work on this project from the beginning, and it was my primary job to search for the right vendors who could fulfill our demand and build the system. In the March Meeting 2019 in Boston, MA, we sorted two companies which could potentially work on few aspects of our project: Cryogenic Ltd as magnet company and Virginia Diodes for high frequency components. We had several online and in person meetings, phone calls and email conversations, with several companies including these two, from which conclude on what we wanted to build in our lab. Later we learned about Thomas Keating who could help us with the high frequency circuitry. After months of discussions with several companies and experts, these three companies appeared to fit our demand and agreed to work in collaboration with each other to build our system. This was a challenging job in part being completely custom designed and other part being made by three different companies where a part/instrument made by one is supposed to fit and well align within sub-millimeter accuracy with the part made by another. Even after placing orders to all three companies, we organized several meeting involving us and all three companies to make sure we

all were on the same page until they finish their task. Finally, everyone completed their part of the job and the long-awaited system got delivered in the spring of 2021. It took longer than expected to remotely install the system and learn about the working mechanism of different components, but I took the lead on each part of this task. Now the system is up and running and the team has a very good understanding of its working mechanism. We have performed test experiments to verify working of the system. The operation of the system has been verified from different test measurements. A detailed explanation about the system with its different aspects, working mechanism and the results of the initial test measurements is given in chapter 2 of this thesis.

1.3 Spectroscopic characterization of 2D magnets

In previous sections I have explained our spintronics project with a major focus on insulating AFMs for the realization of control-tunable THz sources and detectors which could potentially boost the performance of several technologies including communication and security. We also learned that it is not obvious to achieve such an ambitious goal. We are trying to address our challenges by performing several experiments on the high frequency set up installed in the lab, introduced in section 1.2, together with our collaborators. On the other hand, to show the proof of concept of the considered THz oscillator we are also exploring AFMs with special characteristics whose dynamics lie in a lower frequency range and could be used in antiferromagnet-based spintronics devices.

In addition to bulk AFMs, where the strong exchange interaction between nearby sublattice magnetization uplifts the dynamics to THz and sub-THz range, there are other types of AFMs which are becoming fascinating because of their unique properties as 2D systems and low (accessible) frequency dynamics [39, 40]. Some of these AFMs are topological insulators (TIs) [40, 41], which are exotic materials in which the bulk state is insulating, but with topologically protected conducting surface states [42]. TIs are already used in spintronics where they replace high spin orbit coupling materials like Pt for the spin charge interconversion. Furthermore, they seem to be much more efficient in spin charge interconversion than Pt

[33, 34], which could be used in our proposed THz oscillator to reduce the required high current density threshold. Having magnetic topological insulators adds another important aspect to this fast-evolving class of materials and one can imagine the realization of a spintronics auto-oscillator made of these materials which are magnetically ordered with high spin orbit coupling within themselves. Experimental realization of 2D magnetic TIs, which can be used in devices of reduced dimensionality is even more exciting. One class of such materials is $\text{MnBi}_2\text{Te}_4(\text{Bi}_2\text{Te}_3)_n$ where $n = 0, 1$ and 2 compounds are antiferromagnetically coupled and the coupling strength decreases with increasing value of n [40].

The potential application of any material requires careful study of its properties, which is true in the case of magnetic materials as well. In magnetism, the first step towards this is to study detailed dynamics of these materials to explore the nature of dynamics they possess and dictate their position in the frequency spectrum. One way to do this experimentally is to perform a detailed spectroscopic characterization. In our case, we have performed a detailed spectroscopic study in two members of $\text{MnBi}_2\text{Te}_4(\text{Bi}_2\text{Te}_3)_n$ family with $n = 1$ and 2 i.e., MnBi_4Te_7 and $\text{MnBi}_6\text{Te}_{10}$ and found interesting results. A detailed explanation of these measurements is given in chapter 3 of this thesis.

1.4 Molecular electronics using SETs

While we were waiting for our new system to be made by a collective effort of three different vendors Covid-19 came under way, and like everyone else we were also severely affected in this project. Everything got pushed back including the delivery date of the different parts of the new system to be machined. With setbacks, including campus shutdown and several other restrictions due to Covid-19, the new system arrived almost a year late from the initial expected delivery date. Even after the delivery, it took a long time, about 4 months, to get the new system properly installed and running due to the travel ban imposed to company technicians because of Covid-19. This whole process affected my research study where we wanted to use this system to focus on my spintronics research, but we had to wait for the system delivery for a long time and multiple changes in the delivery date from a couple of our vendors made the

waiting even longer. However, during that waiting period I got heavily involved in another project on molecular electronics in which we measured transport across single molecular junctions. The reason for this involvement on another project was to utilize my time while learning new techniques and try to implement the technique of single molecular junction measurements to our spintronics project. While we are still unsure whether we will be able to use this technique in spintronics, we got beautiful results from measurements on a single molecule which forms the fourth chapter of this thesis. Nevertheless, there is a growing field of molecular spintronics which combines many fields including organic spintronics, molecular magnetism, molecular electronics, and quantum computing. This field of molecular spintronics is advancing fast and promises large technological payoffs as described in the review article in reference [43]. So far, the molecular spintronics devices rely on molecular Self-Assembled Monolayer (SAM) junctions [44] where the collective response of many molecules at the same time is gathered, but our approach of molecular electronics is to study molecules at a single molecular level using the so-called single electron transistors (SETs) [45]. In our perspective, study of spin based single molecules using SET method can give insights into the underlying physical mechanism involving spin dynamics and transport of spin information at the molecular level. This approach has been well established and widely used in the case of transport measurements across single molecular junctions, even in our group. We believe the same approach would also work for spin-based single molecules. Verification of this requires a careful study on a completely different project which is out of scope of this thesis. But for now, we are going to describe a unique way of realizing universal logic gates at the single molecular level in chapter 4 of this thesis.

1.5 References

- [1] R. Kleiner, "Filling the Terahertz Gap," *Science*, vol. 318, no. 5854, pp. 1254-1255, 2007, doi:10.1126/science.1151373.
- [2] R. Cheng, D. Xiao, and A. Brataas, "Terahertz Antiferromagnetic Spin Hall Nano-Oscillator," *Phys Rev Lett*, vol. 116, no. 20, p. 207603, May 20 2016, doi: 10.1103/PhysRevLett.116.207603.
- [3] R. Khymyn, I. Lisenkov, V. Tiberkevich, B. A. Ivanov, and A. Slavin, "Antiferromagnetic THz-frequency Josephson-like Oscillator Driven by Spin Current," *Sci Rep*, vol. 7, p. 43705, Mar 6 2017, doi: 10.1038/srep43705.
- [4] O. R. Sulymenko, O. V. Prokopenko, V. S. Tiberkevich, A. N. Slavin, B. A. Ivanov, and R. S. Khymyn, "Terahertz-Frequency Spin Hall Auto-oscillator Based on a Canted Antiferromagnet," *Physical Review Applied*, vol. 8, no. 6, 2017, doi: 10.1103/PhysRevApplied.8.064007.
- [5] O. R. Sulymenko, O. V. Prokopenko, V. S. Tyberkevych, and A. N. Slavin, "Terahertz-Frequency Signal Source Based on an Antiferromagnetic Tunnel Junction," *IEEE Magnetics Letters*, vol. 9, pp. 1-5, 2018, doi: 10.1109/lmag.2018.2852291.
- [6] G. Consolo, G. Valenti, A. R. Safin, S. A. Nikitov, V. Tyberkevich, and A. Slavin, "Theory of the electric field controlled antiferromagnetic spin Hall oscillator and detector," *Physical Review B*, vol. 103, no. 13, 2021, doi: 10.1103/PhysRevB.103.134431.
- [7] X.-L. Li, X. Duan, Y. G. Semenov, and K. W. Kim, "Electrical switching of antiferromagnets via strongly spin-orbit coupled materials," *Journal of Applied Physics*, vol. 121, no. 2, 2017, doi: 10.1063/1.4974027.
- [8] A. Litvinenko *et al.*, "Ultrafast Sweep-Tuned Spectrum Analyzer with Temporal Resolution Based on a Spin-Torque Nano-Oscillator," *Nano Lett*, vol. 20, no. 8, pp. 6104-6111, Aug 12 2020, doi: 10.1021/acs.nanolett.0c02195.
- [9] A. Safin *et al.*, "Electrically tunable detector of THz-frequency signals based on an antiferromagnet," *Applied Physics Letters*, vol. 117, no. 22, 2020, doi: 10.1063/5.0031053.
- [10] P. Wadley *et al.*, "Electrical switching of an antiferromagnet," *Science*, vol. 351, no. 6273, pp. 587-590, 2016, doi:10.1126/science.aab1031.
- [11] V. E. Demidov *et al.*, "Magnetic nano-oscillator driven by pure spin current," *Nat Mater*, vol. 11, no. 12, pp. 1028-31, Dec 2012, doi: 10.1038/nmat3459.
- [12] M. Ranjbar *et al.*, "CoFeB-Based Spin Hall Nano-Oscillators," *IEEE Magnetics Letters*, vol. 5, pp. 1-4, 2014, doi: 10.1109/lmag.2014.2375155.
- [13] S. I. Kiselev *et al.*, "Microwave oscillations of a nanomagnet driven by a spin-polarized current," *Nature*, vol. 425, no. 6956, pp. 380-383, 2003/09/01 2003, doi: 10.1038/nature01967.
- [14] L. Neel, "Magnetism and the local molecular field," in "Nobel lectures, Physics," 1963-1970 1970.
- [15] A. Safin, S. Nikitov, A. Kirilyuk, V. Tyberkevych, and A. Slavin, "Theory of Antiferromagnet-Based Detector of Terahertz Frequency Signals," *Magnetochemistry*, vol. 8, no. 2, 2022, doi: 10.3390/magnetochemistry8020026.

- [16] J. Železný, P. Wadley, K. Olejník, A. Hoffmann, and H. Ohno, "Spin transport and spin torque in antiferromagnetic devices," *Nature Physics*, vol. 14, no. 3, pp. 220-228, 2018, doi: 10.1038/s41567-018-0062-7.
- [17] O. Gomonay, V. Baltz, A. Brataas, and Y. Tserkovnyak, "Antiferromagnetic spin textures and dynamics," *Nature Physics*, vol. 14, no. 3, pp. 213-216, 2018, doi: 10.1038/s41567-018-0049-4.
- [18] I. Boventer, H. T. Simensen, A. Anane, M. Klaui, A. Brataas, and R. Lebrun, "Room-Temperature Antiferromagnetic Resonance and Inverse Spin-Hall Voltage in Canted Antiferromagnets," *Phys Rev Lett*, vol. 126, no. 18, p. 187201, May 7 2021, doi: 10.1103/PhysRevLett.126.187201.
- [19] R. Lebrun *et al.*, "Tunable long-distance spin transport in a crystalline antiferromagnetic iron oxide," *Nature*, vol. 561, no. 7722, pp. 222-225, Sep 2018, doi: 10.1038/s41586-018-0490-7.
- [20] P. Vaidya *et al.*, "Subterahertz spin pumping from an insulating antiferromagnet," *Science*, vol. 368, no. 6487, pp. 160-165, 2020, doi: doi:10.1126/science.aaz4247.
- [21] K. Olejník *et al.*, "Terahertz electrical writing speed in an antiferromagnetic memory," *Science Advances*, vol. 4, no. 3, p. eaar3566, doi: 10.1126/sciadv.aar3566.
- [22] T. Jungwirth, X. Marti, P. Wadley, and J. Wunderlich, "Antiferromagnetic spintronics," *Nat Nanotechnol*, vol. 11, no. 3, pp. 231-41, Mar 2016, doi: 10.1038/nnano.2016.18.
- [23] V. Baltz, A. Manchon, M. Tsoi, T. Moriyama, T. Ono, and Y. Tserkovnyak, "Antiferromagnetic spintronics," *Reviews of Modern Physics*, vol. 90, no. 1, 2018, doi: 10.1103/RevModPhys.90.015005.
- [24] X. Marti, I. Fina, and T. Jungwirth, "Prospect for Antiferromagnetic Spintronics," *IEEE Transactions on Magnetics*, vol. 51, pp. 1-4, 2015.
- [25] J. Li *et al.*, "Spin current from sub-terahertz-generated antiferromagnetic magnons," *Nature*, vol. 578, no. 7793, pp. 70-74, Feb 2020, doi: 10.1038/s41586-020-1950-4.
- [26] O. Sulymenko *et al.*, "Ultra-fast logic devices using artificial "neurons" based on antiferromagnetic pulse generators," *Journal of Applied Physics*, vol. 124, no. 15, 2018, doi: 10.1063/1.5042348.
- [27] N. Biniskos *et al.*, "Complex magnetic structure and spin waves of the noncollinear antiferromagnet Mn₅Si₃," *Physical Review B*, vol. 105, no. 10, 2022, doi: 10.1103/PhysRevB.105.104404.
- [28] K. K. M. Hagiwara, H. Yamaguchi, M. Tokunaga, I. Yamad, M. Gross, and P. Goy, "A complete frequency-field chart for the antiferromagnetic resonance in MnF₂," *International Journal of Infrared and Millimeter Waves*, vol. 20, 1999.
- [29] a. G. J. G. P. R. Elliston, "Some antiferromagnetic resonance measurements in Fe₂O₃," *J. Phys. C: Solid State Phys.*, vol. 1, no. 169, 1968.
- [30] A. N. B. A. S. Borovik-Romanov, and N. M. Kreines, "The weak ferromagnetism of NiF₂," *Sov. Phys.-JETP*, vol. 37, 1973.
- [31] A. Markou, J. M. Taylor, A. Kalache, P. Werner, S. S. P. Parkin, and C. Felser, "Noncollinear antiferromagnetic Mn₃Sn films," *Physical Review Materials*, vol. 2, no. 5, 2018, doi: 10.1103/PhysRevMaterials.2.051001.
- [32] E. Saitoh, M. Ueda, H. Miyajima, and G. Tatara, "Conversion of spin current into charge current at room temperature: Inverse spin-Hall effect," *Applied physics letters*, vol. 88, no. 18, p. 182509, 2006.

- [33] A. R. Mellnik *et al.*, "Spin-transfer torque generated by a topological insulator," *Nature*, vol. 511, no. 7510, pp. 449-51, Jul 24 2014, doi: 10.1038/nature13534.
- [34] P. Li *et al.*, "Magnetization switching using topological surface states," *Science Advances*, vol. 5, no. 8, p. eaaw3415, 2019, doi: doi:10.1126/sciadv.aaw3415.
- [35] F. J. González and G. D. Boreman, "Comparison of dipole, bowtie, spiral and log-periodic IR antennas," *Infrared Physics & Technology*, vol. 46, no. 5, pp. 418-428, 2005, doi: 10.1016/j.infrared.2004.09.002.
- [36] J. van Tol, L. C. Brunel, and R. J. Wylde, "A quasioptical transient electron spin resonance spectrometer operating at 120 and 240 GHz," *Review of Scientific Instruments*, vol. 76, no. 7, 2005, doi: 10.1063/1.1942533.
- [37] T. V. Can *et al.*, "Overhauser effects in insulating solids," *J Chem Phys*, vol. 141, no. 6, p. 064202, Aug 14 2014, doi: 10.1063/1.4891866.
- [38] K. David, "Helium is again in short supply," *Physics Today*, 2022, doi: 10.1063/PT.6.2.20220404a.
- [39] D. MacNeill, J. T. Hou, D. R. Klein, P. Zhang, P. Jarillo-Herrero, and L. Liu, "Gigahertz Frequency Antiferromagnetic Resonance and Strong Magnon-Magnon Coupling in the Layered Crystal CrCl₃," *Phys Rev Lett*, vol. 123, no. 4, p. 047204, Jul 26 2019, doi: 10.1103/PhysRevLett.123.047204.
- [40] J. Q. Yan *et al.*, "A-type antiferromagnetic order in MnBi₄Te₇ and MnBi₆Te₁₀ single crystals," *Physical Review Materials*, vol. 4, no. 5, 2020, doi: 10.1103/PhysRevMaterials.4.054202.
- [41] M. M. Otrokov *et al.*, "Prediction and observation of an antiferromagnetic topological insulator," *Nature*, vol. 576, no. 7787, pp. 416-422, Dec 2019, doi: 10.1038/s41586-019-1840-9.
- [42] J. E. Moore, "The birth of topological insulators," *Nature*, vol. 464, no. 7286, pp. 194-8, Mar 11 2010, doi: 10.1038/nature08916.
- [43] A. Cornia and P. Seneor, "Spintronics: The molecular way," *Nat Mater*, vol. 16, no. 5, pp. 505-506, Apr 25 2017, doi: 10.1038/nmat4900.
- [44] A. Ulman, "Formation and Structure of Self-Assembled Monolayers," *Chemical Reviews*, vol. 96, no. 4, pp. 1533-1554, 1996/01/01 1996, doi: 10.1021/cr9502357.
- [45] H. Song, Y. Kim, Y. H. Jang, H. Jeong, M. A. Reed, and T. Lee, "Observation of molecular orbital gating," *Nature*, vol. 462, no. 7276, pp. 1039-43, Dec 24 2009, doi: 10.1038/nature08639.

CHAPTER 2: A CONTINUOUS FREQUENCY AND POLARIZATION TUNABLE HIGH FREQUENCY SPECTROSCOPIC SYSTEM OPERATING IN THE 220GHz-1.1THz RANGE

This section describes the need, design, installation, working mechanism and initial results of a state-of-the-art high frequency system recently installed in Del Barco lab at UCF.

2.1 Introduction

Magnetic resonance spectroscopy is an important technique which gives access to magnetization dynamics [1-3], Landé g-factor [4], and anisotropy of magnetic materials [5]. Such spectroscopy is given a particular name depending on the type of magnetic material involved, including electron paramagnetic resonance (EPR) [6-8], nuclear magnetic resonance (NMR) [9, 10], and ferromagnetic resonance (FMR) [11-13] where unpaired electron spins, nuclear magnetic moments and magnetization are the resonating magnetic species respectively. In the case of antiferromagnets, the sublattice magnetizations play the leading role in the absorption of electromagnetic radiation giving rise to antiferromagnetic resonance (AFMR) [14, 15]. All the spectroscopies involved with these resonances find their practical applications in technologies as well as in research and development. EPR spectroscopy is widely used in different fields to detect and identify magnetic free radicals [16-18] as well as in material characterization [18, 19]; while NMR spectroscopy techniques are commonly used in chemistry and molecular physics to investigate molecular structures[20, 21], and is known in medicine as magnetic resonance imaging [22, 23]. FMR and AFMR spectroscopy are useful techniques to characterize ferromagnets and antiferromagnets probing the magnetic dynamics and associated anisotropies of those materials [1-3, 24, 25], with vast applications in magnetic-based technologies, such as magnetic memory or spintronics.

Magnetic resonance spectroscopy requires irradiation of a magnetic sample with microwaves of a particular frequency and its detection after interaction with the sample while sweeping the magnetic field or vice versa (i.e., static field while sweeping the microwave frequency). It is usually done by using vector

network analyzers (VNAs) that serve both as the source and the detector and perform the ratio between the outgoing and incoming signals to determine the response of the sample [26]. Shown in Fig. 2.1 is the low temperature magnetic spectroscopy measurement system in DelBarco lab at UCF where an Agilent VNA model E8463B is used for microwave transmission measurements.

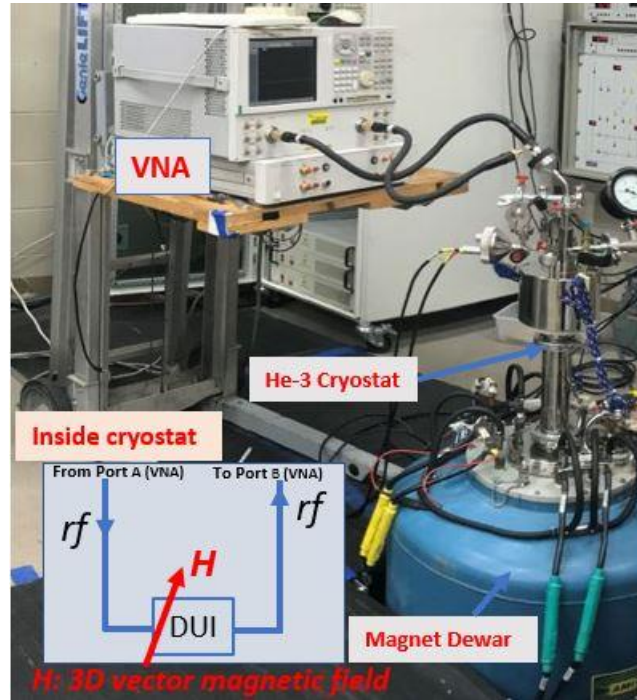


Figure 2.1: A magnetic spectroscopic system

A Low temperature spectroscopic system operating up to 50GHz using VNA in DelBarco lab UCF. A helium-3 cryostat or dilution refrigerator is used to cool down sample temperature and a 3D-vector magnet is used to apply magnetic field in required direction while passing microwaves through sample using coaxial cables.

However, most of the commercially available VNAs are limited in frequency up to around 50GHz, a threshold which is set by the capability of electronics used in signal processing in the oscillators used to generate frequency. This frequency is extended up to around 100GHz by attaching expensive millimeter wave frequency extension modules to the output frequency of VNAs, practically setting the lower limit of the THz gap. On the high frequency limit of the THz gap. On the high frequency limit of the gap we found optical sources that can easily generate signals with frequencies above 10THz and therefore be used in

spectroscopy as well as in other studies and technologies. This 10THz lower limit (setting the high limit of the THz gap) is imposed by the performance of semiconductor lasers and light emitting diodes. In between these two frequencies lies the so-called THz-gap [27] which is defined as the existence of several technological challenges in terms of signal generation, processing, and detection in the frequency range 0.1-10THz [28]. The existence of this gap is not only preventing technologies in communications, non-destructive testing, and biological sensing to operate at higher speeds, but also affecting research and development activities in the gap region due to lack of easily accessible resources. It is not only a problem with generation and detection in the THz gap region but also with the required optics to work within this range as it lies outside the bands covered by electronics and conventional optics. A quasi optical set up [29] is required to work in the THz gap region which involves specially designed corrugated waveguides, feed horns, metallic mirrors, and fine wire grids to manipulate the THz signal. Nonetheless, there are a few research facilities which operate in the lower frequency side of this THz gap but only for a few discrete monochromatic frequencies [30, 31] and access to those facilities usually requires long wait times. On the other end, the high frequency side of this gap is being pushed by optical methods where the THz signals are generated by methods like electro-optical sampling [32, 33]. A signal produced this way is usually of broadband in nature which is not useful in cases where a monochromatic frequency is desired.

In spite of these technological limitations, there is a plethora of magnetic materials, particularly antiferromagnets (AFMs), whose dynamics lie in the THz gap region [3, 34-39] and their use in spintronics devices as potential THz oscillators [40-43] and detectors [44-46] has been suggested theoretically. Study and understanding of the magnetic behavior of such materials for their possible use in THz spintronics devices require a well-established research facility capable of performing detailed experiments in a broad range of temperatures, in a continuous frequency range, and in the presence of strong magnetic fields. Several of these AFMs have chiral dynamical modes [3, 47] which require research facilities with polarization tunability for their complete understanding. Successful realization of experiments involving such high frequency magnetic materials can lead to the development of new techniques for practical

applications in the THz range, forbidden by the THz-gap, thereby advancing currently existing technologies. For this transformative study it is desirable to have an easily accessible research facility which could be used to perform the required experiments for the realization of THz frequency oscillators and detectors.

Here we describe a custom designed state-of-the-art high frequency quasi-optical multifunctional system which is continuously frequency tunable from 220GHz to 1.1THz and is capable of polarization rotation at any given frequency within the range, as well as easily expandable into the broader frequency range 60GHz to 1.5THz with the addition of electronic components. The system operating in the temperature range from 5K to 300K and at magnetic fields up to 9T. The cryostat and split coil magnets are furnished with optical access ports from all three major directions to the sample sitting on a 2-axes rotatable sample holder capable of performing arbitrary rotations with respect to the field direction. Moreover, this system can also be used for transport studies, measurements across single molecules, EPR studies at lower frequencies using a VNA, and studies involving ultrafast laser pulses. Results from initial test measurements in antiferromagnetic MnF_2 single crystals are presented that verify the operation of the system.

2.2 System description

This high frequency system consists of a split coil 9T cryofree magnet (CFM) system, a cryofree variable temperature cryostat (VTC) with optical access, and a quasi-optical circuit system to work with high frequency microwave (HFM) as shown in Fig. 2.2(A). The CFM, shown as (ii) in Fig. 2.2(A), has a 92 mm room temperature through bore port along the field direction which allows the user to slide the cryostat into the magnet to align the sample in the magnetic field. In addition, the CFM has a 30 mm room temperature through bore port transverse to the major bore opening to allow optical access to HFM. The CFM also has an additional room temperature bore port transverse to the others described earlier which gives additional optical access to the sample in the cryostat. The VTC, shown as (i) in Fig. 2.2(A), has a

sample stage attached to a cold finger whose temperature can be set from 5K to 300K using a lakeshore temperature controller model 350. The VTC has a window block, with five optical windows, which attaches with five optical windows: two of diameter 25mm and three of diameter 34mm, which attaches to a narrow tail section that goes into the room temperature magnet bore of the CFM. The five rather large room temperature windows of the system results into a compromise of the operating temperature of the system due to black body radiation heating. The system cools the sample down to different base temperatures depending on the number of windows optically open to the sample position. When all 5 windows are open, the system cools down to 35K. When only two windows are open while blocking the other three by a metallic sheet at the radiation shield of the cryostat it can cool down to 20K. When only one window is open, the sample cools down to 15K. When all the windows are completely blocked at the sample position, the system cools down to 5K. The operating temperatures in the case when one and two windows are open can be reduced further down to 6K and 12K respectively by using conical pieces at the radiation shield position by reducing the room temperature black body radiation getting to the sample position. The temperature above the base temperature of each case can be tuned up to 300K using a set of feedback-controlled heaters.

The VTC sits on a sliding rail so that it can be moved in and out of the CFM to align the sample with the magnetic field and along the direction of HFM, and to open the window block while changing samples. The sample stage has an outside accessible rotatable sample holder which allows sample rotation along in and out of plane direction with respect to the magnetic field. The sample stage has one LCC44 chip carrier holder with a maximum of 44 connections to the sample which become very important in some of the measurements where it is required to measure several nanoscale devices at one time. There are four micro-coaxial cables terminated near the sample stage with mini-SMP connectors which makes it possible to work with low frequency microwave up to 50GHz in a field up to 9T. An image of the rotatable sample holder with few other parts is shown in Fig. 2.2(D).

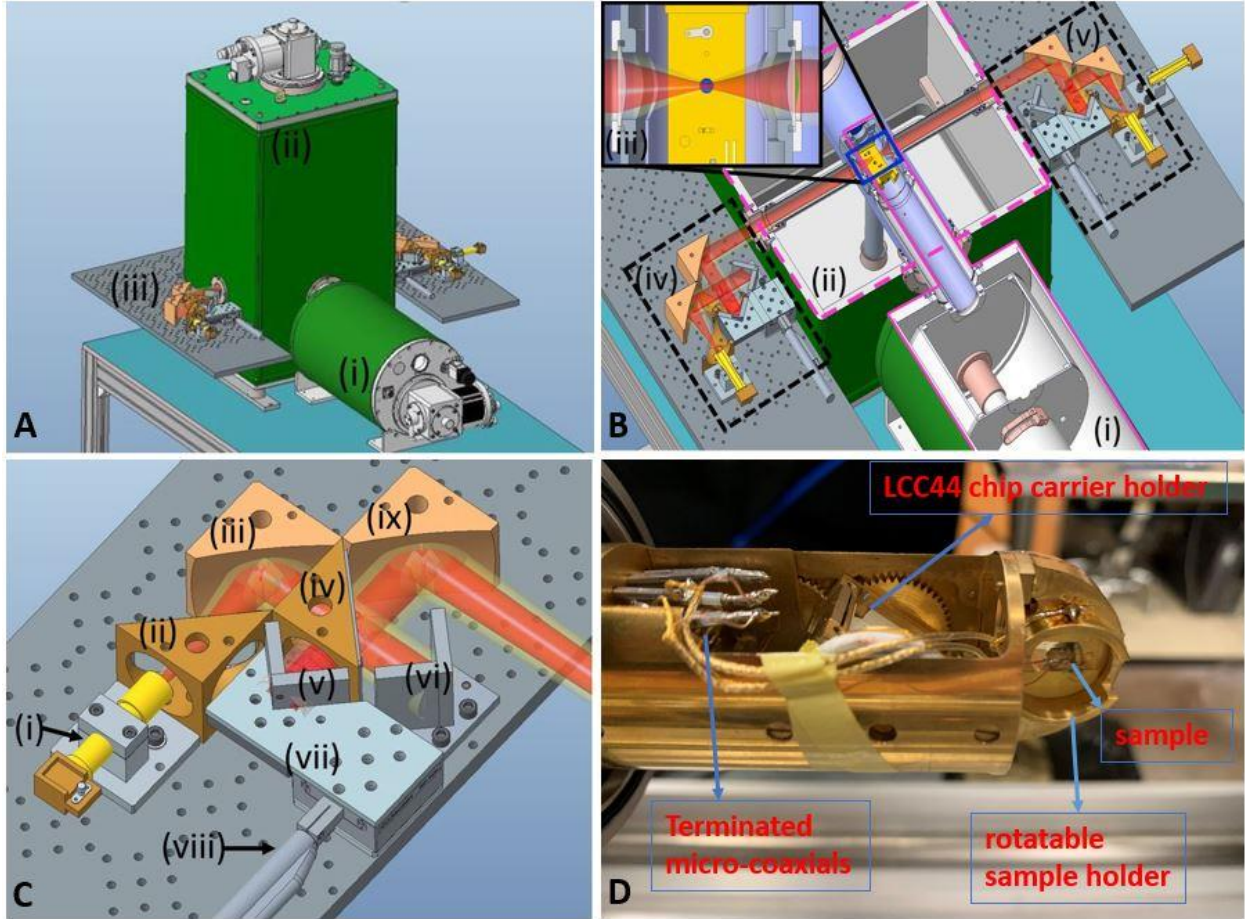


Figure 2.2: System description

(A) System design with parts (i), (ii) and (iii) representing VTC, CFM and quasi-optical system. The whole system stage is fixed to a movable station and can be moved from one lab to another. (B) Detailed sketch of system where cryostat is inserted into the magnet bore while aligning with the HFM beam (shown in red color). In this figure, (i) represents section of the cryostat showing its alignment in the system, (ii) represents section of magnet with cryostat inserted and beam passing through room temperature bores, (iii) represents sample holder region of cryostat where the HFM beam is focused on the sample position using specially designed impedance matched focusing lenses, the beam is collimated once it passes the second lens, (iv) and (v) represent transmitter and receiver side of the quasi-optic system respectively. (C) Components of transmit/receive side where (i) represents corrugated feed horn which is attached to either source or detector depending on its side and transmits/receives HFM beam from (to) the source (detector), (ii) represents a polarizing wire grid with wires in the horizontal direction which polarizes HFM beam to vertical linear polarization, (iii) and (ix) represent metallic parabolic mirrors which are used to focus and collimate the HFM beam, (iv) represents a beam splitter grid aligned at 45° which partially transmits and

reflects the incoming beam into two parts which are used in polarization rotation, (v) and (vi) represent roof mirrors which form part of M-P interferometer, (vii) represents a moving platform attached to the roof mirror (v) and (viii) represents a motorized actuator which is used to translate moving platform (vii) and is controlled remotely by a Newport ESP302 motion controller. (D) An image of a sample holder attached to the cold finger of cryostat showing a sample mounted at the rotatable sample position with two wire connections for electrical measurement.

The overall circuit with the HFM beam passing through the quasi-optical elements, magnet bore, and the cryostat is shown in Fig. 2.2(B). The window block has two sets of specially designed high frequency impedance matched lenses which allows focusing the collimated HFM beam into the sample position and re-collimating the outgoing beam as shown in the inset. When aligned properly, the sample sits at the center of the magnetic field while the HFM beam passing through it and allows us to study desired sample properties in the form of spectroscopic or electrical signal. The magnetic field, magnet bores, cryostat windows, sample position, and the HFM beam all are designed, and height adjusted such that there is no misalignment between any of these components. The quasi-optical system consists of a transmit-receive system on each side of the magnet across the 30 mm bore, shown as (iii) in Fig. 2.2(A). Both the transmitter and the receiver side contain metallic blocks with wire grids, parabolic mirrors, roof mirrors and feed horns, shown in detail with each element in Fig. 2.2(C). Each side with its own Martin-Puppet (M-P) interferometer allows polarization tuning of microwave at a given frequency as well as collimation of the HFM beam to allow passage through the magnet bore towards/away from the sample. In each M-P interferometer, one of the two roof mirrors has a translation stage, attached to a motorized actuator whose motion is assisted by a motion controller, making it possible to tune the polarization of the desired HFM on both the transmitter and the receiver sides of the system independently. An image of the fully installed system in the laboratory is shown in Fig. 2.3.

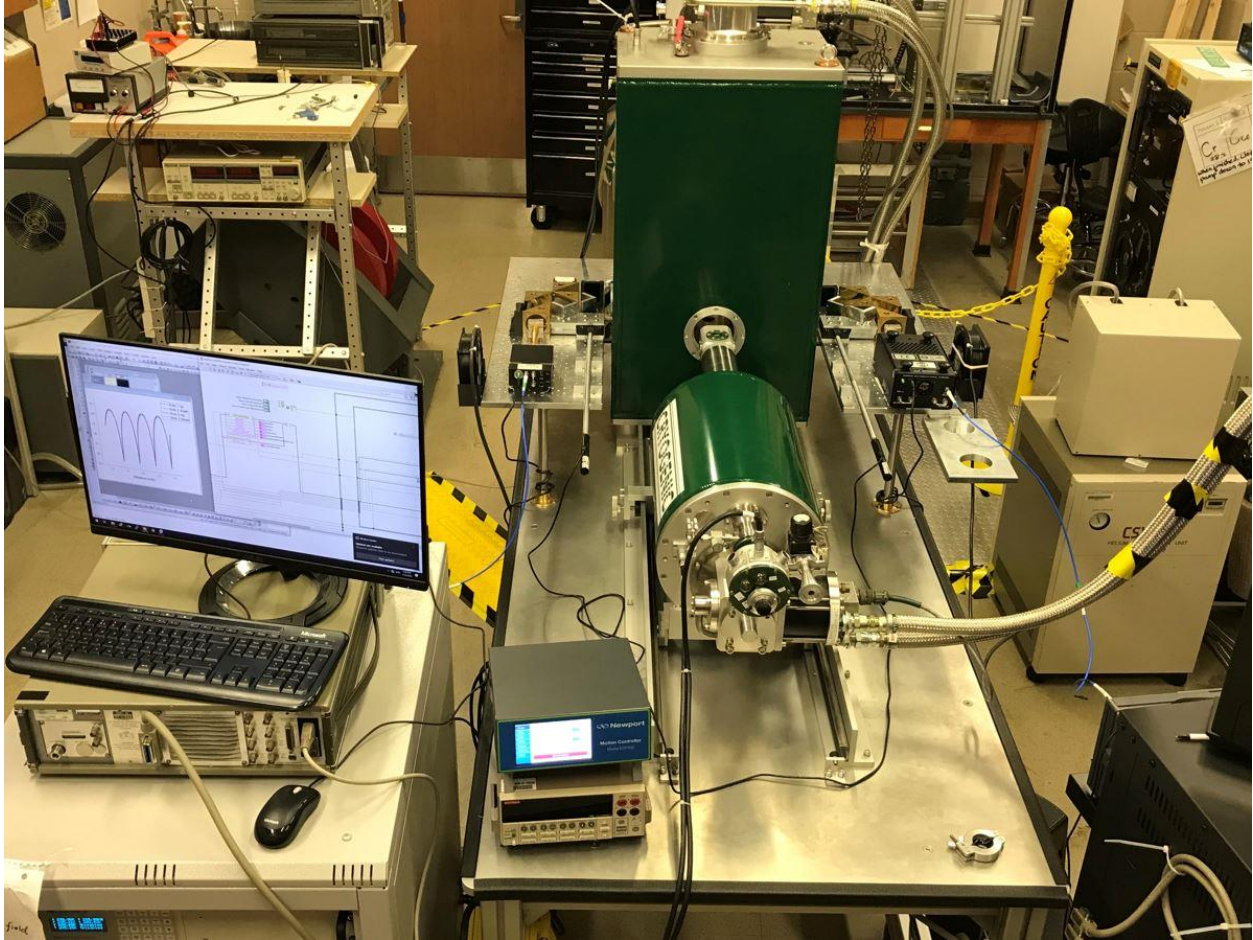


Figure 2.3: An image of the fully installed operating system in del Barco lab at UCF showing different components of the system described in the figure 2.2.

The HFM signal is generated using Virginia Diodes (VDI) high frequency extension modules. An HP sweep oscillator model 8350B, capable of generating microwave signals from 10MHz to 20GHz, is used as base unit to generate the original rf signal. Out of its frequency range, 9.259GHz - 13.89GHz at 10dBm power is used to drive a VDI Signal Generator Extender (SGX) module with multiplication factor of 9 giving an output frequency in the range 82.5 – 125 GHz. The output of the SGX module is connected to different frequency multipliers under different configurations to cover the entire range from 82.5GHz to 1.1THz, on the transmitter side, with a small gap from 125GHz to 170GHz. The average output HFM power levels on each of the frequency bands at the source output is given in table 2.1. Even though the system possesses

the capability of frequency generation below 220GHz, the minimum frequency the quasi-optical set up is optimized to work with is 220GHz. Below 220GHz the microwave signal cannot be collimated well enough to focus on the sample position within the space provided by the optical access ports in the magnet. Nevertheless, HFM below 220GHz can still be used as source to generate dynamics even in non-optimized circuitry.

Table 2.1: Installed HFM frequency bands and the available average output power level in each band

Frequency band (GHz)	Average output power from source (dBm)	Average power at the sample position (dBm)	Detection capability
82.5-125	+20	--	No
170-250	+10	+6.5	Only above 220GHz
250-375	+5	+3.5	Yes
340-500	-4	-6	Yes
500-750	-11	-15	Yes
750-1100	-16	-21.5	Yes

The desired HFM signal emitted from each SGX module configuration passes through a feed horn of a specific frequency range and gets directed into the quasi-optical system. The HFM signal passes through several different optical components of the transmit-receive system and the cryostat before it is received by the signal analyzer. This beam path is shown by the red beam in Fig. 2.2(B). On the receiver side, the HFM signal is received by VDI's Spectrum/Signal Analyzer Extension Modules (SAXs) through feed horns for the different specific frequency ranges, using frequency mixing to down convert the HFM into lower frequencies. The down converted signal is finally detected either by a state-of-the-art spectrum analyzer with an external mixer option operating in the frequency range 10Hz to 32GHz, or by a lock in amplifier using a diode detector. Four different SAX receiver modules are used to cover the entire range of the circuit working in the frequency ranges 220-330GHz, 330-500GHz, 500-750GHz and 750GHz-1.1THz. To set the system at a specific frequency configuration, all the required frequency multipliers are connected at the output end of the SGX module, and the total multiplication factor is calculated considering the multiplication of each of the multipliers used. The required driving frequency is then calculated by using the following equation:

$$\text{Driving frequency} = \frac{\text{Final Output frequency}}{\text{Total multiplication factor}} \quad (3)$$

Once this is determined, the *HP* sweep oscillator is set at the calculated frequency at +10dBm power level. In the case where a frequency sweep is required, the hp sweep oscillator is remotely set to increase its frequency in the steps required for the given measurement. On the receiver side, a proper ranged SAX module needs to be connected to receive the outcoming signal through a feed horn. The spectrum analyzer has to be set in the external mixer option with a right multiplication factor given for the corresponding SAX module used and a right frequency range must be selected to detect the outcoming frequency. For more accurate reading of the detected power level, a correction is applied to the frequency spectrum for the range of each SAX modules which account for the conversion loss while down converting the signal. It is also important to turn ON the signal ID (SID) option in the spectrum analyzer which removes any image signal in the observed spectrum. Moreover, each of the SAX modules have their damage power threshold limit. To ensure safe operation of the SAX modules, the signal from the transmitter side is attenuated on its path using a stack of microscope glass slides before the beam reaches the receiver side feed horn. This can be done before/after the sample placement depending on power requirement at the sample position.

In our first test measurement in the newly assembled system the power level abruptly dropped in the observed output spectrum at a magnetic field of about 4.2T. After a careful analysis of the whole system, we noticed the SGX module auto turning off at higher fields exceeding 4.2T. Later we discovered the cooling fans of internally cooled SAX and SGX module were turned off, within first few tesla ramping of the magnetic field, leading to overheat of the SGX module causing it to auto-turn off using a safety mechanism. This required a modification of the SGX module and installation of much stronger external ac fans which work unaffected up to 9T magnetic field. This external cooling mechanism is applied to both the SGX and the SAX modules and have been working great so far without any further issues.

2.3 Working Mechanism of the Quasi-Optical system for polarization tuning

The quasi-optical circuit system is used to direct the HFM to the sample and collimate it afterwards for the detection as well as to tune the polarization. Polarization tuning is done by using the M-P interferometer on both transmit as well as receive sides. As shown in Fig. 2.2(C), the HFM beam from a feed horn is directed to a horizontal grid which polarizes it vertically. A metallic parabolic mirror then collimates the vertically polarized (VP) HFM beam and directs it towards a 45° aligned polarizing wire grid which partially reflects and transmits the beam. The reflected part of the beam is sent to a movable roof mirror while the transmitted part is reflected by a fixed roof mirror. The reflected beams from these two roof mirrors recombine giving again a HFM beam of the same frequency but of a specific polarization, determined by the optical path difference of the two split beams. If the two beams have a path difference as an integral multiple of the microwave wavelength (λ) then the output is a linearly polarized beam similar to the original one. If the path difference is an odd integral multiple of $\lambda/4$ then the output is a circularly polarized beam of one handedness. And if the path difference is an integral multiple of $\lambda/2$ then the output is a linear polarized beam of the opposite type. In between the circular and linear polarization lies an elliptical polarization. In this way the polarization of the HFM beam can be continuously tuned from linear vertical to horizontal passing by left- and right-handed circular polarizations. This is the basic working principle of the M-P interferometer as described in the original article [48].

In the case of this new system, the degree of polarization can be continuously tuned by changing the position of the movable roof mirror on the source or the detector side by the use of the motorized actuator, as shown in Fig. 2.2(C). Fig. 2.4(A) shows how exactly the polarization cycles with respect to the motion of each of the moveable roof mirrors. In the case considered the wavelength is 1mm,

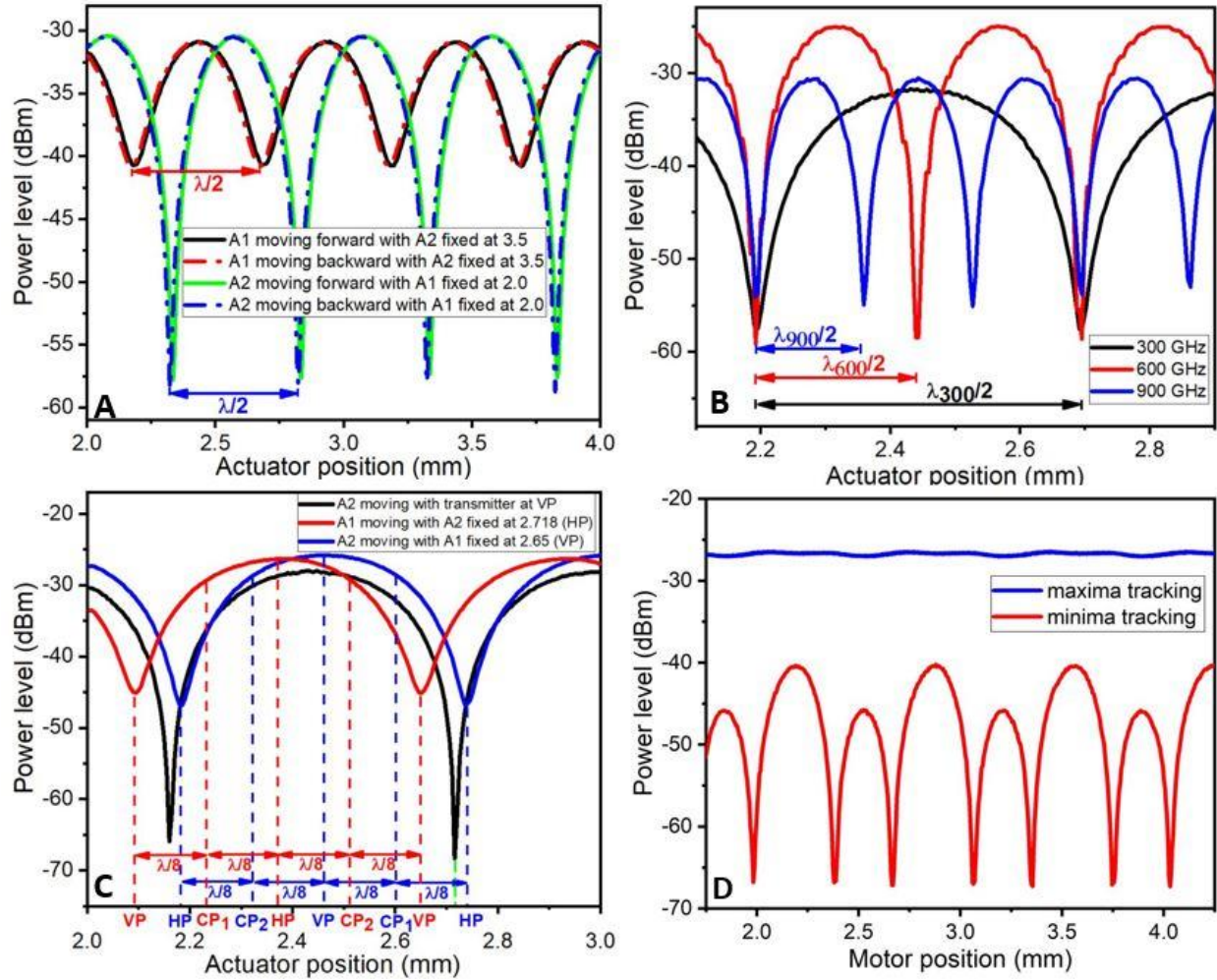


Figure 2.4: Illustration of working mechanism of quasi-optical system.

(A) shows the polarization cycling of 300GHz signal performed by moving actuators on transmitter and receiver side independently. Black and red (green and blue) curves respectively represent polarization cycling created by moving roof mirror on the transmitter (receiver) side forward and backward using actuator A1 (A2) while keeping the receiver (transmitter) side polarization constant. Red (blue) double sided arrows show the polarization cycling happening at $\lambda/2$ translation of roof mirrors on transmitter (receiver) side. (B) Polarization cycling for different frequencies with respect to the motion of roof mirror on transmitter side while keeping polarization of receiver side as constant. Black, red and blue color curves represent the polarization cycling for 300GHz, 600GHz and 900GHz respectively, with double headed arrows of corresponding color representing polarization cycling at $\lambda/2$ translation of roof mirror for a given frequency. (C) polarization tuning of source and detector side at 300GHz. Black curve represents polarization rotation of receiver side while forcing vertical linear polarization from the transmitter side. Red curve represents polarization rotation of transmitter side while fixing the receiver side at vertical linear

polarization determined from black curve (see description in the text for details). This calibrates polarization of transmitter side with respect to the motion of roof mirror1. Blue curve represents the recalibration of receiver side for any polarization done by fixing transmitter side at position of vertical polarization. This sets polarization of receiver side with respect to the motion of roof mirror2. Red (blue) vertical dotted lines represent position of different polarization transmitter (receiver) side with respect to the position of roof mirror set by movable actuator of corresponding side. Double headed arrows of corresponding color represent a distance of $\lambda/8$ for frequency at 300GHz. (D) shows graphics for tracking of same polarization (blue curve) and cross polarization (red curve) while moving the actuators on both sides at the same time.

corresponding to a 300GHz microwave signal used in the test. The black (red) curve shows the output power level detected on the receiver side while the roof mirror on the transmitter side is moved from 2-4mm (4-2mm) while the receiver side polarization remains constant. It is obvious to see the curve completing its cycle every $\lambda/2$ distance (i.e., 0.5mm), the roof mirror travels, which corresponds to an overall path difference of λ , 1mm, as the beam moves both forward to and backward from the movable roof mirror. The observed change in the detected signal intensity as a function of actuator position is due to the change in polarization of the HFM beam generated by the motion of the roof mirror. Even though more calibration is required to figure out which actuator position corresponds to which polarization, it is evident that the detected signal is maximum when both the transmit and receive systems are set on the same polarization and the detected signal intensity will be minimum when the transmit and receive system are set on cross polarization. For example, if the receiver system is set on vertical linear polarization (VP) then the maxima on the curve for detected power level vs actuator position of the transmit system corresponds to the VP of the transmit side. Likewise, a minimum actuator position in the same curve corresponds to horizontal linear polarization (HP) i.e. cross polarization for VP. In this way the detected signal intensity cycles as a function of actuator position as shown in each of the graphics in Fig. 2.4. One thing to notice is that there is a small amount of lag between the two set of curves in Fig. 2.4(A) for the motion of the roof mirror moving forward and backward. This corresponds to the backlash of the actuator motor used to move the roof mirror. In real measurements this is accounted by moving each of the movable roof mirror always

in one direction but can also be accounted by considering the backlash while moving the actuator in the opposite direction. A similar result is observed while moving the roof mirror in the receiver side while keeping the transmitter side at one arbitrary polarization, shown by green and blue curves. Again, we observe polarization cycling with actuator position displaced by $\lambda/2$ i.e., path difference λ .

Figure 2.4(B) shows polarization cycling at different frequencies, 300GHz, 600GHz and 900GHz, with respect to the motion of roof mirror on transmitter side while keeping the receiver side on any fixed position. Moreover, the curves are translated horizontally and vertically to bring the minima for all frequencies near 2.2mm for clear observation. At 300 GHz, the polarization cycles through every 0.5mm ($\lambda_{300}/2$) of the motor position displacement shown by the black curve. At 600GHz, the polarization cycles twice in the same roof mirror displacement corresponding to one cycle of 300GHz shown by the red curve. This observation is as expected and corresponds to a wavelength reduction to half, i.e., $\lambda_{600} = \lambda_{300}/2$. At 900GHz, the polarization cycles three times within one cycle of 300GHz corresponding to a reduction in wavelength by a factor of 3, i.e., $\lambda_{900} = \lambda_{300}/3$, shown by the blue curve. All these measurements at different frequencies show the effective operation of the quasi-optical system and M-P interferometer to cycle and tune the polarization of the HFM by moving the moveable roof mirror on each side independently. From this, one can also generalize that the polarization cycling and tuning works for the entire range of frequency i.e., from 220GHz to 1.1THz. Having tuned the polarization of the transmitter and the receiver side independently, this system can be used to send one polarization to the sample and detect any response created by the sample in a different polarization as well as to perform detailed polarization rotations generated by samples under study.

Even though the working principle of the system for polarization cycling on both the transmitter and the receiver side has been described so far, it is still required to explain the calibration method to distinguish which actuator position on each side corresponds to what specific polarization. We use our own method to tune the polarization of the system to know which actuator motor position or corresponding movable roof mirror position on either side corresponds to which specific polarization. To determine this,

first, we move the vertical polarization grid on the transmitter side from its original position to a position next to the second parabolic mirror just before the magnet bore, which can be seen in Fig. 2.2(B). This forces the VP to pass through the grid irrespective of any polarization produced by M-P interferometer beforehand. The data is given for 270 GHz, but this is true for any given frequency. The next step is to move the roof mirror on the receiver side to tuning the polarization to get a polarization cycling like the black curve in Fig. 2.4(C). In this curve, the minima correspond to the position of cross polarization i.e., HP and midway between two minima lies a maxima or same polarization i.e., VP. In this way we determine the polarization of the receiver side with respect to the vertical polarization coming from the source side. In a real case scenario, the transmit side has to be set for any type of incoming polarization so we need to tune both sides for any given polarization. Now we take one of the minima i.e., HP on the receiver side, 2.718mm in the graphic shown by the green vertical dotted line, to set the polarization of the transmitter side. After moving the vertical polarizing grid back to its normal position, we move the actuator (A1) of the transmitter side to change the polarization and obtain a polarization cycling similar to the red curve in Fig. 2.4(C). Since the receiver side is set to receive HP at its maximum, the minima on this graphic will correspond to the position of VP. If we move a distance $\lambda/8$ from the position of minimum we get to a position of circular polarization of one handedness, CP1. Moving in the same direction by another $\lambda/8$ distance will give the position of maximum i.e., HP. If we move a further distance by $\lambda/8$ in the same direction, we get to a position of another circular polarization opposite to that of earlier one i.e., CP2. Moving another distance of $\lambda/8$ brings us back to the position of another minimum or we come to our starting position in terms of polarization. This cycle of polarization rotation continues as a function of actuator position. The positions of different polarizations on the transmitter side obtained on a test calibration using 270 GHz frequency is shown clearly by the red curve and red dotted lines in Fig. 2.4(C). Now that the polarization of the transmitter side is tuned, one has to go back to the receiver side to tune the polarization for any arbitrary polarization coming from the transmitter side. For this one of the minimum positions on the red curve is taken and A1 is set on that particular position i.e. 2.65mm in Fig. 2.4(C) to set for VP. Then again A2 is moved to obtain a polarization rotation curve like the one shown in blue in the

graphic. In this case since the transmitter side is set at VP, any minima would correspond to HP, and by moving a distance $\lambda/8$ successively in each direction one can get to the position of CP2, VP, CP1 and so on as shown by the blue dotted lines in Fig. 2.4(C). In this way the polarization of both the transmitter and the receiver sides is tuned and each side's polarization can be set independently. One thing to note here is that for polarization dependent measurements it is important to tune the polarization of both sides for a given frequency as the wavelength changes and tuned polarization for one frequency does not work for another frequency in general.

Once the polarization of both sides is tuned, we can move both the actuators A1 and A2 at the same time to track the desired set of relative polarizations. With this one can continuously track both sides for the same relative polarization and cross polarization. Figure 2.4(D) shows two curves where the maxima and minima were tracked continuously in two different test measurements. The maxima tracking curve, corresponding to the same polarization of either side for each data point on the curve, is almost constant in power level, reflecting relatively constant set of maxima in the polarization cycling curves. On the other hand, the minima tracking curve, corresponding to the cross polarization on both sides for each data point in the curve, is modulated more than expected. We attribute this modulation to the sharp nature of the minima in the polarization cycling curve which is sensitive even to a micrometer misalignment between the cross-polarization positions of the two roof mirrors on both sides.

2.4 Test measurements to verify the system

A series of test measurements have been performed to verify this system using two different bulk samples of the well-known high frequency easy axis antiferromagnet (AFM) MnF_2 , which has a zero field resonance at 261GHz at low temperature [3]. A 500 μm thick polished bulk sample (sample 1) was used to perform a frequency dependent, angle rotation and polarization dependent measurement. Another sample of thickness about 3mm (sample 2) was used to perform a temperature dependent measurement, frequency sweeps and a polarization dependent measurement of a different kind.

2.4.1 Frequency dependent measurements

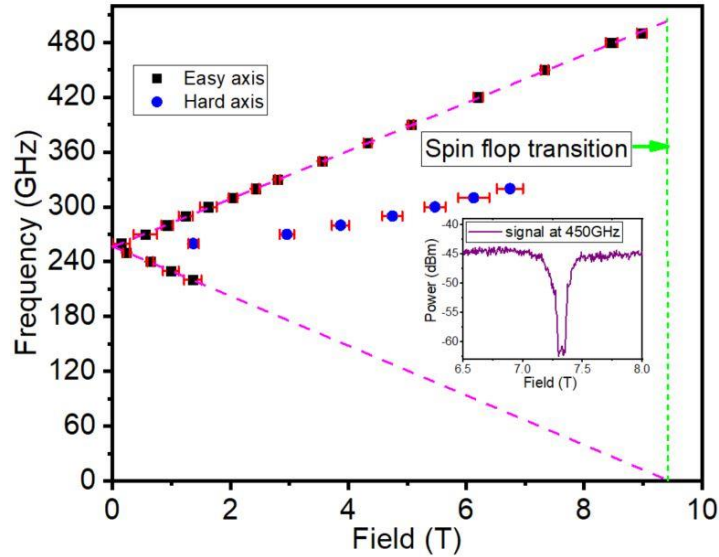


Figure 2.5: A Frequency vs field plot for the resonance position while applying field along the easy axis and the hard axis directions performed on sample1 at 12K. Dotted magenta lines are straight guidelines connecting resonance positions for field along easy axis. The zero-field resonance is observed at 257 GHz (see text for details). The inset shows a sample raw signal at 450GHz where a signal extinction can be clearly seen across the resonance position. The center of this extinction region is taken as the position of resonance and the width of extinction is taken as the error. The green vertical dotted line at 9.54T represents the spin flop transition of MnF_2 which is just beyond the capacity of our maximum field limit, 9T.

In Fig. 2.5 we show frequency dependent field sweep measurements on sample 1 while applying the field along the easy and the hard axis (black squares and blue spheres, respectively). These measurements were done at 12K and in a frequency range from 220GHz to 480GHz within the maximum field range for AFMR supported by our field limit of 9T. As shown in the sample AFMR signal in the inset of Fig. 2.5, we get complete extinction of the spectroscopic signal in the bulk sample within the dynamic range provided by the spectrum analyzer used in the measurement. Since there is no sharp resonance peak, the center of the resonance extinction region is taken as the resonance position in the plot for resonance position as a function of frequency and the width of the extinction as the error. In the graphic, magenta color lines are the guidelines connecting the resonance position and one can see the zero-field resonance around 256.75GHz. This zero-field resonance is almost 4GHz below the standard zero field resonance

described elsewhere [3, 47] and is attributed to the higher temperature, 12K, used in this measurement. From the easy axis data of the graphic, we get frequency mapping of the resonance position for both the upper branch and the lower branch eigen modes of MnF_2 . These two branches have opposite chiralities, the upper branch being right-handed circularly polarized and the lower branch being left-handed circularly polarized, which is a characteristic feature of easy axis AFMs like MnF_2 [3, 47]. The lower branch guideline crosses the field axis at 9.54T, obtained from a linear fit of the data, which corresponds to the spin flop transition of this sample, above which the magnetic sublattices rotate by 90° and the magnetization enters the quasi-ferromagnetic mode with further increase in field value as described in references [3, 47]. We also rotate the sample by 90° and perform measurements along the hard axis of this sample which are also shown in the same graphic. This signal behavior also agrees well with data from the literature [3].

2.4.2 Temperature dependent measurements

Temperature dependent field sweep measurements were performed at 260GHz on sample2 while aligning the sample easy axis along the field and the results are shown in Fig. 2.6. Raw spectrum plots at various temperatures are shown in the inset with color codes, and the resonance position and error bars are extracted and plotted on the main graph as temperature vs field. With increase in temperature the resonance position moves higher in field, and the increment results in two types of slopes which can be seen from the graphic. Below the AFM Neel temperature (67K), of this material the signal increases slowly towards higher field with increase in temperature, and after the Neel temperature the signal moves relatively faster towards the higher field. These two regions correspond to the antiferromagnetic and paramagnetic regions below and above the Neel temperature respectively. Other important information to note from the raw spectrum plot is the signal width, which is smaller for the antiferromagnetic regime and becomes broader and broader in the paramagnetic region with increase in temperature. This increase in signal width is represented by larger value of errors in the graphic.

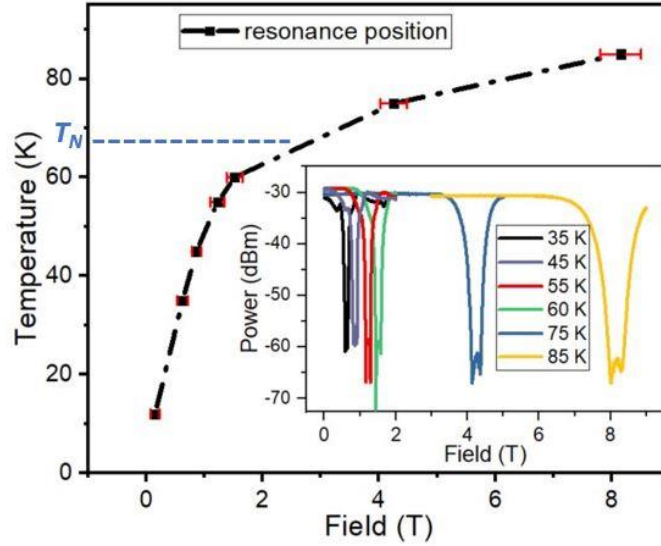


Figure 2.6: Temperature dependent measurements performed on sample2 at 260GHz. The resonance positions at different measurement temperatures are plotted as a function of magnetic field. Different trends of slopes across transition temperature (67K) denote antiferromagnetic nature of the signal at lower temperatures and paramagnetic the signal at higher temperatures. The inset shows the raw spectrum obtained at different temperatures. The resonance position was taken as center of the extinction region and the width of extinction was taken as the error.

2.4.3 Frequency sweep measurements

In Fig. 2.7, we show the frequency sweep measurements at different applied fields. This type of measurement displays one of the unique aspects of this system where one can sweep frequency in the high frequency range at a given temperature and magnetic field permitted by the system capability. As per available knowledge, there is no such system in the world where one can continuously sweep frequency there is no such system in the world where one can continuously sweep frequency in this region of HFMs. Here we have shown frequency sweep measurements on sample 2 at 25K and different applied fields up to 1T, where we see splitting of degenerate magnon mode with the application of magnetic field. We observe a very clear zero field degenerate resonance mode around 243GHz, shown by black curve. With the application of magnetic field, the degeneracy lifts and we start to see both upper and lower branch signals as shown in red, green and blue color curves for 0.25T, 0.75T and 1T fields respectively. As expected from

the measurements [3, 47] and our own data in Fig. 2.5, the split mode in the high frequency side moves higher in frequency with increase in field in contrast to the one in lower frequency side.

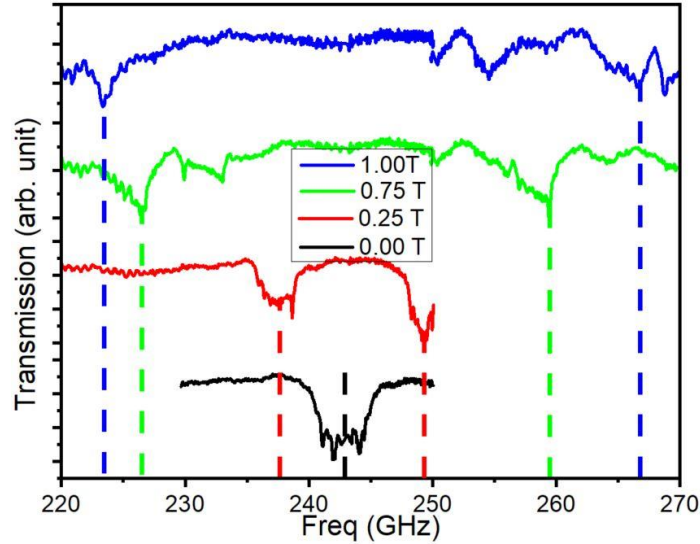


Figure 2.7: Frequency sweep measurements done at fixed field values on sample2 at temperature 35K. Black, red, green and blue curves represent frequency sweeps at 0.00, 0.25, 0.75 and 1.00T respectively. Vertical lines of corresponding color represent resonance positions for that sweep.

Here, the observation of the zero-field mode at lower frequency, 243GHz, compared to standard 261GHz is attributed to the higher temperature used in the measurement. As per our knowledge, this is the first set of data observed on this AFM system in a frequency sweep mode. We are working on increasing the sensitivity of these frequency sweep measurements by modulating the frequency and the magnetic field while sweeping. We also expect to see an improvement in the signal quality by setting the transmit and receive sides at specific known polarizations, which requires a detailed study of frequency sweep measurements which is out of the scope of this study.

2.4.4 Sample rotation measurements

This system also has capability of performing sample rotation measurements with respect to the direction of magnetic field, in plane rotation by $\pm 110^\circ$ from a reference 0° in fine steps of 0.25° and out of

plane rotation by $\pm 15^\circ$ in steps of 1° . This rotation capability allows the user to study magnetic anisotropies while characterizing magnetic samples as well as to find the direction of the symmetry axes like the easy axis in case of uniaxial AFMs. In Fig. 2.8 we show results from angle rotation measurements performed in sample1 to pinpoint the direction of easy axis at 420GHz HFM frequency.

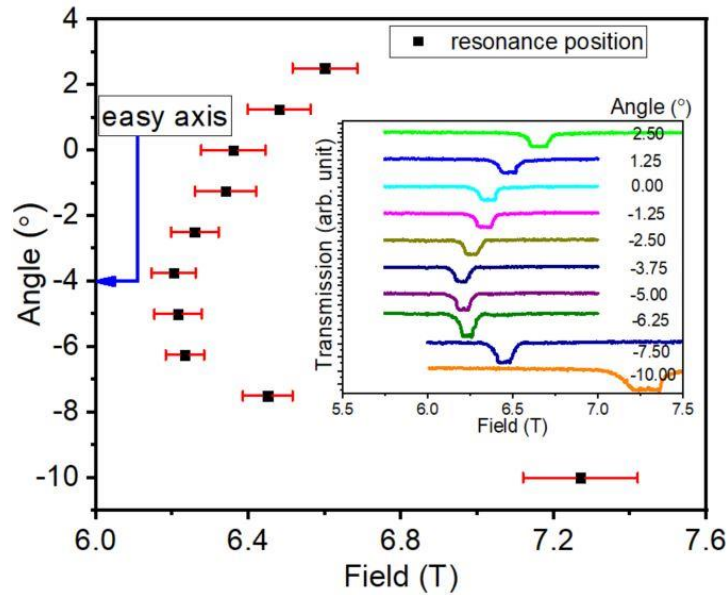


Figure 2.8: Angle rotation measurements done on sample 1 at 420GHz and 12K with sample alignment close to the easy axis. The resonance field positions are plotted against alignment angle relative to a reference line taken for the sample alignment. Center of the signal at the extinction region is taken as the resonance position and the width of the extinction is taken as the error. The raw spectrum is given in the inset. The resonance position has a minimum around -4° which represents the direction of the easy axis.

The 420GHz frequency was taken from the frequency mapping shown Fig. 2.5 for two reasons: the misalignment becomes more prominent towards the spin flop field [47] and the resonance must lie within the field range of our system while covering the deviation coming from the misalignment. Initial measurements were done in larger steps to get a rough estimate of the direction of the easy axis. After that, more detailed measurements were done in steps of 1.25° around the easy axis as shown in Fig. 2.8. The raw spectrum data for the chosen range of angles is shown in the inset. Resonance positions and corresponding errors were taken from the center of the signal extinction region and the width of the extinction respectively

as described earlier for other types of measurements. As shown in the graphic, the angle vs resonance field plot clearly displays the minimum field position occurring around -4° shown by the blue arrow. From this observation, the direction of the easy axis is determined to be aligned along $(-4^\circ \pm 1^\circ)$ with respect to the reference 0° chosen in the sample crystal. An image of the MnF_2 sample used for this measurement is shown in Fig. 2.9. In this figure, the blue horizontal arrow points in the direction of the reference line and the red arrow points in the direction of the easy axis. The angle shown in the image is not to the scale.

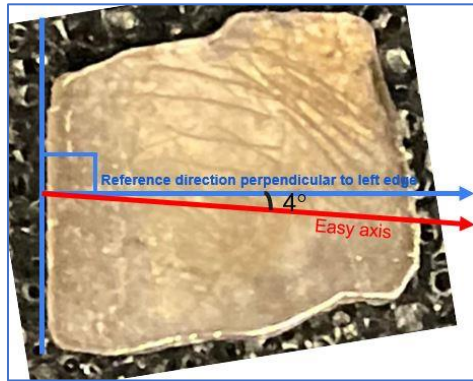


Figure 2.9: MnF_2 sample (sample1) used in the angle rotation measurement for localization of easy axis. Bulk MnF_2 crystal was polished to smoothen down surface roughness to 2nm (rms) and 4nm Pt was deposited on top for next set of transport measurements.

2.4.5 Polarization dependent measurements

Another benefit of this system relies on the continuous polarization tunability at a given frequency. With the help of the movable roof mirrors in the M-P interferometer, one can tune the polarization of the transmitter and the receiver side independently. Fig. 2.11(A) and (B) show plots of some polarization dependent measurements performed on both samples. Fig. 2.11(A) shows polarization dependent measurements on sample1 performed at 240GHz frequency and 12K temperature when both transmitter and receiver sides are tuned to the same polarization. The graphic shows data when both the transmitter and the receiver were tuned to horizontal linear polarization (HP-HP), circular polarization of one handedness (CP1-CP1), vertical linear polarization (VP-VP) and circular polarization of the other handedness (CP2-

CP2), which are shown in blue, green, red and black respectively. To track the polarization of both sides continuously, the roof mirrors on either side were simultaneously set at the position of HP and then moved in opposite directions in steps of distance $\lambda/4$ for successive measurements on other polarizations. The observed signal is strongest for HP-HP configuration and weakest for VP-VP polarization. In between these two signals, the signal for circular polarization is stronger for CP1-CP1 than for CP2-CP2. In addition, the resonance shape also changes from one type of polarization to another type. We attribute this to the polarization selective absorption from the sample.

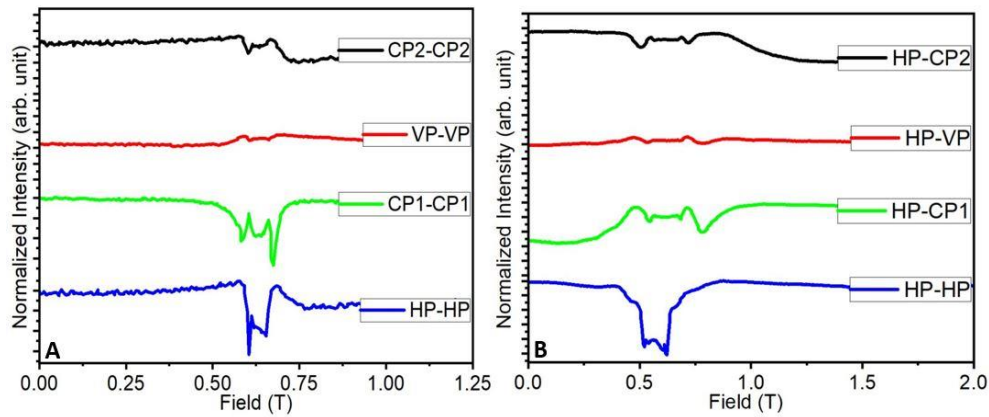


Figure 2.10: Results for polarization dependent measurements (A) shows polarization dependent measurements performed on sample1 at 240GHz and 12K for the case where both transmitter and receiver side are set at same type of polarization. Blue, green, red and black curves represent data taken when polarization of both sides was fixed at HP, CP1, VP and CP2 respectively. (B) shows polarization dependent measurements performed on sample2 at 260GHz and 35K when the polarization of transmitter side was fixed at HP and that of receiver side was rotated around. Blue, green, red and black curves represent data taken when receiver side polarization was set at HP, CP1, VP and CP2 respectively.

Figure 2.11(B) shows data for polarization dependent measurements performed on sample2 at 260GHz where the polarization on the transmitter side was kept constant at HP while the receiver side was changed to different polarizations. As shown in the graphic, a signal with maximum intensity was observed when both the transmitter and the receiver sides were tuned at same polarization i.e., HP-HP. The signal

intensity was minimum when two sides were tuned at cross polarization i.e., HP-VP. In the case when the receiver was tuned on circular polarization, the signal was stronger when the receiver was in CP1 than in CP2 polarization, which makes sense for the circular polarization dependent sample used in the measurement. This also gives a clue about the chirality of HFM at CP1 and CP2. The applied HMF frequency lies on the upper branch of MnF_2 , right-handed circularly polarized, and gives a higher intensity signal for the CP1 position than for the CP2 indicating the receiver side being tuned to the right-handed circularly polarized position at CP1 and the left circularly polarized position at CP2. In addition, the signals for HP-CP1 and HP-CP2 combinations are of opposite nature in terms of line shapes. A detailed study on the phase of nicely resolved spectroscopic signal can give information about the change in the signal phase caused by the sample. This newly built system has the capability for phase sensitive measurements in terms of polarization rotation caused by samples which can be used to extract information about the sample under the investigation. A detailed study on phase sensitive measurements is out of scope of this study.

2.5 Frequency extension plans

The existing high frequency THz circuitry described heretofore is soon to be expanded to continuously cover the range of microwave frequencies between 60GHz and 1.5THz on both the transmitter and the receiver sides (necessary funding already approved). This expansion will make it possible to study many AFM materials which display their dynamical acoustic and optical spin modes below 220GHz and above 1.1THz, respectively. The expansion will involve the addition of necessary electronic components both below and above the currently existing frequency range, and the modification of the quasi-optical circuitry to focus and transport a coherent beam of microwaves below 220GHz. The required electronic components include two new SGX modules (with output frequencies in the range 60-90GHz and 110-170 GHz) and four new SAX modules (with detection capabilities in the range 60-90 GHz, 90-140 GHz, 140-220GHz and 1.1-1.5 THz). In addition, several new frequency multipliers and amplifiers will be used not only to cover the source frequency up to 1.5THz but also to provide higher microwave powers, in several

bands, necessary for an efficient charge-spin interconversion in AFM spintronic devices. The power amplified bands will be 60-115 GHz (20dBm), 115-170 GHz (~25dBm), 250-270 GHz (17dBm), 290-340GHz (18dBm), 500-540 GHz (7dBm), 600-640 GHz (9dBm) and 900-1000 GHz (0dBm).

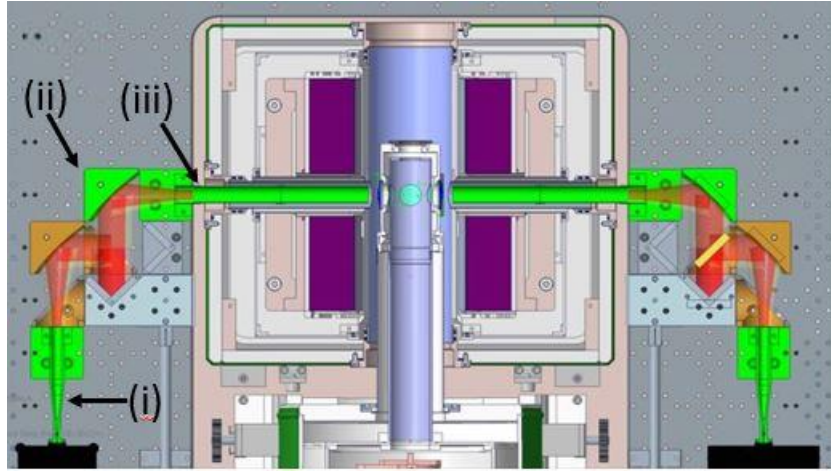


Figure 2.11: A design showing the upgraded THz circuitry. The components to be added to the existing circuitry (shown in figure 1 (b)) is marked in green. In the figure (i), (ii) and (iii) represent the corrugated feed horn, a collimating parabolic mirror and a corrugated waveguide respectively.

To address the limitation imposed by the small aperture of the access to the magnet core for the broad microwave beam below 220GHz, a series of corrugated waveguides, corrugated feed horns, focusing mirrors and collecting cryostat lenses will be acquired. The modified circuitry for the low frequency is shown in green in Fig. 5 where the items labelled (i), (ii) and (iii) represent a corrugated feed horn, a collimating parabolic mirror, and a corrugated waveguide, respectively. The corrugated feed horns will produce a gaussian beam for the microwave coming out from the multipliers and feed the signal to be detected by the SAX module. The specially designed corrugated waveguide will allow the coherent transport of the beam collimated by a parabolic mirror to and from the sample. A set of specially designed impedance matched high frequency lenses will be used to focus the beam to the sample position and recollimate the outgoing beam towards the transmitter side. In addition, a set of specially designed NIR reflective blockers will also be used inside the lenses to improve the low end of the operating temperature of the system.

This upgraded system will cover a broad range of frequencies and provide the necessary high-power levels required for efficient spin-charge interconversion in AFM spintronic devices across the available frequency spectrum.

2.6 Conclusion

In summary, a unique frequency tunable high frequency spectroscope operating in the THz gap region is designed, successfully installed and test measurements are performed using well known MnF₂ samples. In addition to normal spectroscopy, the system can also be used for transport measurements with high frequency microwaves, optical and UV radiation as well as ultrafast laser pulses. The system has continuous frequency tunability from 220GHz to 1.1THz and will be soon expanded into 60GHz-1.5THz for spectroscopic measurements and the system polarization can be tuned on the transmitter and the receiver side independently for a given frequency using two M-P interferometers, one on each side. Measurements can be performed at varied temperatures from 5K to 300K in a range of magnetic fields up to 9T, and samples can be rotated in as well as out of the sample plane with respect to the magnetic field. A unique system like this, with all the features described in this paper, has opened an exciting research opportunity to work in the frequency range abandoned by the THz gap.

2.7 References

- [1] D. B. Gopman, J. W. Lau, K. P. Mohanchandra, K. Wetzlar, and G. Carman, "Determination of the exchange constant of Tb 0.3 Dy 0.7 Fe 2 by broadband ferromagnetic resonance spectroscopy," *Physical Review B*, vol. 93, no. 6, p. 064425, 2016.
- [2] Z. Celinski, K. B. Urquhart, and B. Heinrich, "Using ferromagnetic resonance to measure the magnetic moments of ultrathin films," *Journal of Magnetism and Magnetic Materials*, vol. 166, no. 1, pp. 6-26, 1997/02/01/ 1997, doi: [https://doi.org/10.1016/S0304-8853\(96\)00428-3](https://doi.org/10.1016/S0304-8853(96)00428-3).
- [3] K. K. M. Hagiwara, H. Yamaguchi, M. Tokunaga, I. Yamad, M. Gross, and P. Goy, "A complete frequency-field chart for the antiferromagnetic resonance in MnF₂," *International Journal of Infrared and Millimeter Waves*, vol. 20, 1999.
- [4] J. M. Shaw, H. T. Nembach, T. J. Silva, and C. T. Boone, "Precise determination of the spectroscopic g-factor by use of broadband ferromagnetic resonance spectroscopy," *Journal of Applied Physics*, vol. 114, no. 24, p. 243906, 2013.
- [5] R. E. Kopp, C. Z. Nash, A. Kobayashi, B. P. Weiss, D. A. Bazylinski, and J. L. Kirschvink, "Ferromagnetic resonance spectroscopy for assessment of magnetic anisotropy and magnetostatic interactions: A case study of mutant magnetotactic bacteria," *Journal of Geophysical Research: Solid Earth*, vol. 111, no. B12, 2006.
- [6] V. M. Kovalev and I. G. Savenko, "Paramagnetic resonance in spin-polarized disordered Bose-Einstein condensates," *Sci Rep*, vol. 7, no. 1, p. 2076, May 18 2017, doi: 10.1038/s41598-017-01125-4.
- [7] B. M. Weckhuysen, R. Heidler, and R. A. Schoonheydt, "Electron spin resonance spectroscopy," *Characterization I*, pp. 295-335, 2004.
- [8] B. Bleaney and K. W. H. Stevens, "Paramagnetic resonance," *Rep. Prog. Phys.*, vol. 16, no. 108.
- [9] P. G. de Gennes, P. A. Pincus, F. Hartmann-Boutron, and J. M. Winter, "Nuclear Magnetic Resonance Modes in Magnetic Material. I. Theory," *Physical Review*, vol. 129, no. 3, pp. 1105-1115, 02/01/ 1963, doi: 10.1103/PhysRev.129.1105.
- [10] E. R. Andrew, "Nuclear magnetic resonance," *Nuclear Magnetic Resonance*, 2009.
- [11] C. Kittel, "On the Theory of Ferromagnetic Resonance Absorption," *Physical Review*, vol. 73, no. 2, pp. 155-161, 1948, doi: 10.1103/PhysRev.73.155.
- [12] J. H. E. Griffiths, "Anomalous High-frequency Resistance of Ferromagnetic Metals," *Nature*, vol. 158, no. 4019, pp. 670-671, 1946/11/01 1946, doi: 10.1038/158670a0.
- [13] S. V. e. Von Sovskii, *Ferromagnetic resonance: the phenomenon of resonant absorption of a high-frequency magnetic field in ferromagnetic substances*. Elsevier, 2016.
- [14] F. Keffer and C. Kittel, "Theory of Antiferromagnetic Resonance," *Physical Review*, vol. 85, no. 2, pp. 329-337, 1952, doi: 10.1103/PhysRev.85.329.
- [15] T. Nagamiya, "Theory of Antiferromagnetism and Antiferromagnetic Resonance Absorption, II," *Progress of Theoretical Physics*, vol. 6, no. 3, pp. 350-355, 1951, doi: 10.1143/ptp/6.3.350.

- [16] M. Goswami, A. Chirila, C. Rebreyend, and B. de Bruin, "EPR Spectroscopy as a Tool in Homogeneous Catalysis Research," *Topics in Catalysis*, vol. 58, no. 12-13, pp. 719-750, 2015, doi: 10.1007/s11244-015-0414-9.
- [17] J. E. Wertz and J. R. Bolton, in *Electron Spin Resonance—elementary Theory and Practical Applications*: Chapman and Hall, 1969.
- [18] C. L. Hawkins and M. J. Davies, "Detection and characterisation of radicals in biological materials using EPR methodology," *Biochimica et Biophysica Acta (BBA) - General Subjects*, vol. 1840, no. 2, pp. 708-721, 2014/02/01/ 2014, doi: <https://doi.org/10.1016/j.bbagen.2013.03.034>.
- [19] A. K. Shukla, *EMR/ESR/EPR spectroscopy for characterization of nanomaterials*. Springer, 2017.
- [20] R. S. Macomber, "A complete introduction to modern NMR spectroscopy," *Nova York*, 1998.
- [21] N. Tjandra and A. Bax, "Direct measurement of distances and angles in biomolecules by NMR in a dilute liquid crystalline medium," *Science*, vol. 278, no. 5340, pp. 1111-1114, 1997.
- [22] P. Mansfield and A. A. Maudsley, "Medical imaging by NMR," (in eng), *Br J Radiol*, vol. 50, no. 591, pp. 188-94, Mar 1977, doi: 10.1259/0007-1285-50-591-188.
- [23] I. L. Pykett, "NMR imaging in medicine," *Scientific American*, vol. 246, no. 5, pp. 78-91, 1982.
- [24] J. C. Kim and S. I. Woo, "Characterization of cobalt clusters nucleated on CoNay by ferromagnetic resonance spectroscopy and carbon monoxide hydrogenation," *Applied catalysis*, vol. 39, pp. 107-121, 1988.
- [25] Z. Zhou *et al.*, "Probing electric field control of magnetism using ferromagnetic resonance," *Nature communications*, vol. 6, no. 1, pp. 1-7, 2015.
- [26] D. Micheli, R. Pastore, A. Vricella, A. Delfini, M. Marchetti, and F. Santoni, "Chapter 9 - Electromagnetic Characterization of Materials by Vector Network Analyzer Experimental Setup," in *Spectroscopic Methods for Nanomaterials Characterization*, S. Thomas, R. Thomas, A. K. Zachariah, and R. K. Mishra Eds.: Elsevier, 2017, pp. 195-236.
- [27] R. Kleiner, "Filling the Terahertz Gap," *Science*, vol. 318, no. 5854, pp. 1254-1255, 2007, doi: 10.1126/science.1151373.
- [28] V. Petrov, A. Pyattaev, D. Moltchanov, and Y. Koucheryavy, "Terahertz band communications: Applications, research challenges, and standardization activities," presented at the 2016 8th International Congress on Ultra Modern Telecommunications and Control Systems and Workshops (ICUMT), 2016.
- [29] R. J. Wylde, "Millimeter-wave gaussian beam-mode optica and corrugated feed horns," *IEEE proceedings*, vol. 131, no. 4, p. 5, 1984.
- [30] J. van Tol, L. C. Brunel, and R. J. Wylde, "A quasioptical transient electron spin resonance spectrometer operating at 120 and 240 GHz," *Review of Scientific Instruments*, vol. 76, no. 7, 2005, doi: 10.1063/1.1942533.
- [31] T. V. Can *et al.*, "Overhauser effects in insulating solids," *J Chem Phys*, vol. 141, no. 6, p. 064202, Aug 14 2014, doi: 10.1063/1.4891866.
- [32] A. G. Davies, E. H. Linfield, and M. B. Johnston, "The development of terahertz sources and their applications," *Phys Med Biol*, vol. 47, no. 21, pp. 3679-89, Nov 7 2002, doi: 10.1088/0031-9155/47/21/302.

- [33] S. S. Dhillon and *e. al.*, "The 2017 terahertz science and technology roadmap," *J. Phys. D: Appl. Phys.*, vol. 50, no. 043001, 2017.
- [34] I. S. Jacobs, S. Roberts, and P. E. Lawrence, "Antiferromagnetic Resonance in CoCl_2 and FeCl_2 ," *Journal of Applied Physics*, vol. 36, no. 3, pp. 1197-1198, 1965, doi: 10.1063/1.1714167.
- [35] E. S. Dayhoff, "Antiferromagnetic Resonance in Cr_2O_3 ," *Physical Review*, vol. 107, no. 1, pp. 84-91, 1957, doi: 10.1103/PhysRev.107.84.
- [36] H. J. Fink and D. Shaltiel, "High-Frequency Resonance of A Weak Ferromagnet: MnCO_3 ," *Physical Review*, vol. 130, no. 2, pp. 627-631, 1963, doi: 10.1103/PhysRev.130.627.
- [37] R. C. Ohlmann and M. Tinkham, "Antiferromagnetic Resonance in FeF_2 at Far-Infrared Frequencies," *Physical Review*, vol. 123, no. 2, pp. 425-434, 1961, doi: 10.1103/PhysRev.123.425.
- [38] Z. Wang *et al.*, "Magnetic field dependence of antiferromagnetic resonance in NiO ," *Applied Physics Letters*, vol. 112, no. 25, 2018, doi: 10.1063/1.5031213.
- [39] G. J. G. P. R. Elliston, "Some antiferromagnetic resonance measurements in Fe_2O_3 ," *J. Phys. C: Solid State Phys.*, vol. 1, no. 169, 1968.
- [40] R. Cheng, D. Xiao, and A. Brataas, "Terahertz Antiferromagnetic Spin Hall Nano-Oscillator," *Phys Rev Lett*, vol. 116, no. 20, p. 207603, May 20 2016, doi: 10.1103/PhysRevLett.116.207603.
- [41] R. Khymyn, I. Lisenkov, V. Tiberkevich, B. A. Ivanov, and A. Slavin, "Antiferromagnetic THz-frequency Josephson-like Oscillator Driven by Spin Current," *Sci Rep*, vol. 7, p. 43705, Mar 6 2017, doi: 10.1038/srep43705.
- [42] O. R. Sulymenko, O. V. Prokopenko, V. S. Tiberkevich, A. N. Slavin, B. A. Ivanov, and R. S. Khymyn, "Terahertz-Frequency Spin Hall Auto-oscillator Based on a Canted Antiferromagnet," *Physical Review Applied*, vol. 8, no. 6, 2017, doi: 10.1103/PhysRevApplied.8.064007.
- [43] O. R. Sulymenko, O. V. Prokopenko, V. S. Tyberkevych, and A. N. Slavin, "Terahertz-Frequency Signal Source Based on an Antiferromagnetic Tunnel Junction," *IEEE Magnetics Letters*, vol. 9, pp. 1-5, 2018, doi: 10.1109/lmag.2018.2852291.
- [44] A. Safin *et al.*, "Electrically tunable detector of THz-frequency signals based on an antiferromagnet," *Applied Physics Letters*, vol. 117, no. 22, 2020, doi: 10.1063/5.0031053.
- [45] G. Consolo, G. Valenti, A. R. Safin, S. A. Nikitov, V. Tyberkevich, and A. Slavin, "Theory of the electric field controlled antiferromagnetic spin Hall oscillator and detector," *Physical Review B*, vol. 103, no. 13, 2021, doi: 10.1103/PhysRevB.103.134431.
- [46] A. Safin, S. Nikitov, A. Kirilyuk, V. Tyberkevych, and A. Slavin, "Theory of Antiferromagnet-Based Detector of Terahertz Frequency Signals," *Magnetochemistry*, vol. 8, no. 2, 2022, doi: 10.3390/magnetochemistry8020026.
- [47] P. Vaidya *et al.*, "Subterahertz spin pumping from an insulating antiferromagnet," *Science*, vol. 368, no. 6487, pp. 160-165, 2020, doi: doi:10.1126/science.aaz4247.
- [48] D. H. Martin and E. Puplett, "Polarised interferometric spectrometry for the millimetre and submillimetre spectrum," *Infrared Physics*, vol. 10, p. 6, 1969.

CHAPTER 3: LOW FREQUENCY SPECTROSCOPY OF 2D VAN DER WAALS ANTIFERROMAGNETIC TOPOLOGICAL INSULATOR $\text{MnBi}_2\text{Te}_4(\text{Bi}_2\text{Te}_3)_n$ FOR $n = 1$ AND 2

3.1 Introduction

Magnetic topological insulators (MTIs) [1-4] are gaining scientific interest since their discovery due to the richness of physics associated with the combination of non-trivial electronic structure and the magnetism found in these compounds. These materials provide a platform for the realization of exotic phenomena like quantum anomalous Hall effect [5-7], chiral Majorana fermions [8-10], topological axion insulators [11, 12], and the topological magnetoelectric effect [13, 14]. The realization of these unusual phenomena in MTIs make them also attractive candidates for applications in spintronics. Indeed, topological insulators (TIs) are already being explored in the field of spintronics attending to properties such as high spin orbit coupling [15, 16], topological surface states [17, 18], and spin-momentum locking [19, 20]. The addition of magnetism to TI characteristics makes them even more powerful materials where one can imagine the realization of self-operating spintronics devices without the need of the heterostructures needed in conventional spintronics [21, 22]. The recent discovery of 2D vdW MTIs [3, 4, 23-27] adds another aspect to the unique properties of MTIs, enabling the possibility of developing spintronics devices of reduced dimensions [28-30] while utilizing exotic topological properties.

$\text{MnBi}_2\text{Te}_4(\text{Bi}_2\text{Te}_3)_n$ (with $n = 0-2$) is a family of magnetic 2D vdW MTIs displaying an easy axis antiferromagnetic ordering below the corresponding transition temperatures. A great emphasis has been given to the study of electronic, magnetic, and thermodynamic properties of this system by using techniques like ARPES, transport and magnetometry, but a detailed magnetic resonance spectroscopy at low frequency probing the magnetic behavior of these materials is still lacking. So far, high-frequency magnetic resonance spectroscopy studies on MnBi_2Te_4 ($n=0$ compound) reveals its easy axis AFM ordering and a high-frequency zero-field dynamical mode [31]. The same high-frequency studies concluded that MnBi_4Te_7 ($n=1$ compound) behaves ferromagnetically [31-33].

Here we describe low-frequency spectroscopy experiments performed on compounds MnBi_4Te_7 ($n=1$) and $\text{MnBi}_6\text{Te}_{10}$ ($n=2$). Neel temperatures for these two compounds have been reported to be 13K [27, 33] and 11k [27], respectively. From the field rotation measurements, we observe the existence of the easy axis anisotropy with a corrugated hard plane in both compounds. Temperature dependent measurements show a unique behavior across the transition temperature suggesting an AF origin of the signals. Our measurements show how the change in stoichiometry affects the strength of the exchange coupling between the two magnetic layers in the compounds.

3.2 Samples and the measurement set up

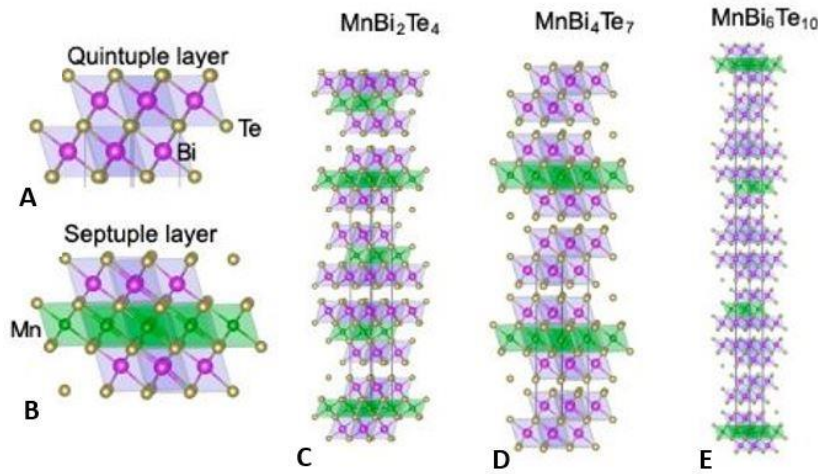


Figure 3.1: Crystal structures of $\text{MnBi}_2\text{Te}_4(\text{Bi}_2\text{Te}_3)_n$ for $n = 0-2$. (A) and (B) respectively show the crystal structures of quintuple and the septuple layers which are the building blocks of the $\text{MnBi}_2\text{Te}_4(\text{Bi}_2\text{Te}_3)_n$ family. (C) shows the crystal structure of the parent compound MnBi_2Te_4 ($n=0$) where the individual septuple layers are stacked together in layers. (D) shows the crystal structure of MnBi_4Te_7 ($n=1$) compound where a non-magnetic quintuple layer is inserted between the two septuple layers of MnBi_2Te_4 . (E) shows the structure of $\text{MnBi}_6\text{Te}_{10}$ ($n=2$) compound where two non-magnetic septuple layer is inserted between the two layers of MnBi_2Te_4 . (Image source: J. Q. Yan et. al., *Phys. Rev. Materials* 4, 054202 (2020))

$\text{MnBi}_2\text{Te}_4(\text{Bi}_2\text{Te}_3)_n$ forms a series of compounds, for different values of n , based on the stacking of two types of layers: the non-magnetic quintuple layer and the magnetic septuple layer as shown in Fig. 3.1(A) and (B) respectively. In the quintuple layer the Bi and the Te atoms are arranged to form a Bi_2Te_3

structure as shown in Fig. 3.1(A) whereas in the septuple layer the addition of the Mn atoms forms the MnBi_2Te_4 structure as shown in Fig. 3.1(B). The presence of the Mn atoms with unpaired electrons in the quintuple layer gives rise to the birth of magnetism in this class of compounds. The magnetic moments of each of the Mn atoms in the layer align in the out of plane direction to the layer giving a net magnetic moment and the individual quintuple layer acts like a ferromagnet [34]. The first compound of the series, MnBi_2Te_4 ($n=0$), is formed by successive stacking of septuple layers on top of each other giving rise to the structure as shown in Fig. 3.1(C). The magnetic layers are found to be coupled by an exchange interaction giving AFM ordering below the Neel transition temperature of this material [3]. In the case of MnBi_4Te_7 ($n=1$ compound), a non-magnetic septuple layer is inserted between the two magnetic quintuple layers of MnBi_2Te_4 giving the structure shown in Fig. 3.1(D). The magnetic layers are spaced out by the addition of the septuple layer which reduces the antiferromagnetic coupling between the two magnetic layers. In the case of $\text{MnBi}_6\text{Te}_{10}$ ($n=2$ compound), the magnetic quintuple layers are further spaced out by the addition of one more septuple layer. The crystal structure of the $\text{MnBi}_6\text{Te}_{10}$ compound is shown in Fig. 3.1 (E). In all these compounds, with $n=0-2$, the adjacent layers (septuple or quintuple) are held in position by a weak van der Waals force making it possible for the exfoliation of these materials. The coupling between the magnetic layers decreases with increasing inter-magnetic layer separation and only the compounds with $n=0-2$ are found to be coupled by antiferromagnetic coupling. In this study we have used epitaxially grown single crystals of MnBi_4Te_7 and $\text{MnBi}_6\text{Te}_{10}$ compounds.

A highly sensitive low temperature magnetic spectroscopy system was used for the measurement where a Helium-3 cryostat was used to cool down the sample and a vector network analyzer (VNA) was used to perform the microwave transmission studies at a varied range of frequencies while applying a magnetic field at arbitrary directions using a 3D superconducting vector magnet. This system allows for spectroscopic measurements up to 50GHz in frequency in a range of temperatures from 250mK to 300K, and in a magnetic field up to 7T, 1.2T and 1.2T along three orthogonal directions. The different components of the measurement system are shown in Fig. 3.2, where (A) is a microscope image of an MnBi_4Te_7 single

crystal sample used for the measurement. (B) is a microscope image of a coplanar waveguide (CPW) which is mounted to a housing box and the sample in (A) is mounted on it using a small amount of a vacuum grease, seen as a shiny part in the image. (C) is an image of the cryostat used for the measurement which allows for the variable temperature measurements to the sample sitting under a vacuum inside it. (D) represent the measurement set up in the lab where the cryostat is inserted into a Helium Dewar of the 3D superconducting vector magnet and the VNA is connected to the cryostat coaxials through the black cables.

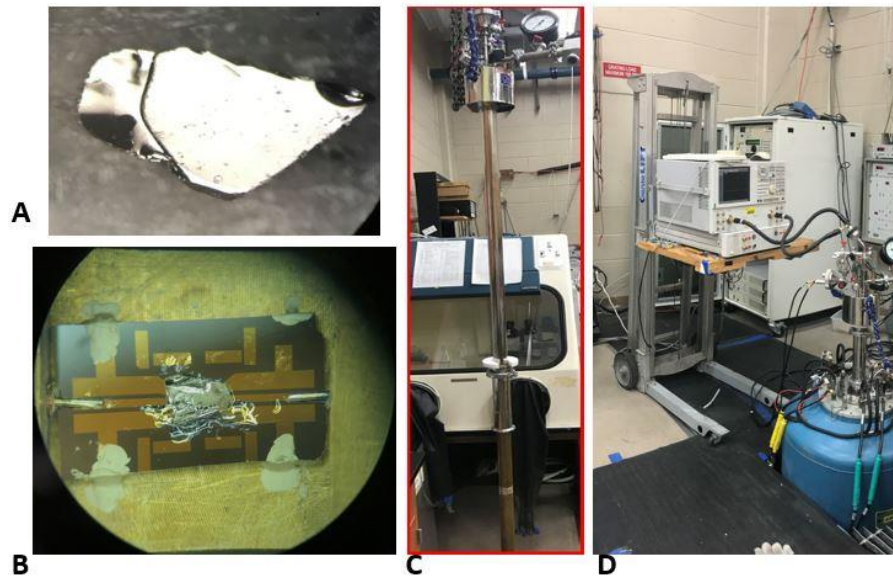


Figure 3.2:(A) A microscope image of an MnBi_4Te_7 single crystal used in the measurement. (B) A microscope image of a CPW mounted on a housing box where the two central lines of coaxial cable make connection to the central line of the CPW while the ground planes are grounded to the housing box using conductive silver paint. (C) An image of the Helium-3 cryostat used for the measurements. (D) An image showing the spectroscopic measurement set up in the lab where the cryostat shown in (C) is inserted in the magnet Dewar filled with liquid helium and a VNA is connected to the cryostat.

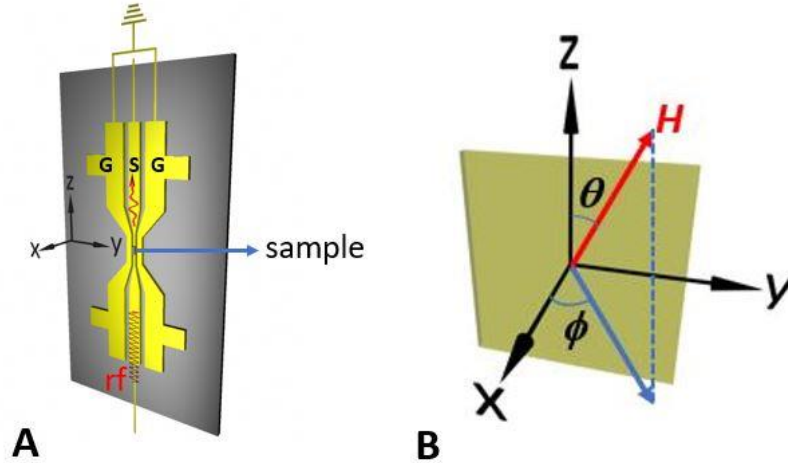


Figure 3.3: (A) A sketch of a CPW with G-S-G configuration used in the measurement. The two ground planes are grounded while the central line on both sides connects to the central line of coaxials coming from the housing box. The sample sits on top of the highly sensitive constricted central region of the CPW. The chosen coordinate system with respect to the CPW is also shown. (B) relative field orientation at the sample sitting on top of the CPW. A planar sample lies on the y-z plane of the chosen coordinate system with x-axis pointing out of the sample plane. z-axis represents the direction parallel to the flow of ac current. Angles θ and ϕ represent the polar angles for the direction of applied magnetic field \mathbf{H} in the chosen coordinate system.

A home fabricated highly sensitive coplanar waveguide (CPW), sketch shown in Fig. 3.3(A), was used for the transmission of microwaves through the sample. The two ends of the source line (S in Fig. 3.3(A)) of the CPW connect to the central lines of coaxial cables in a housing box which eventually connect to the VNA ports through two long coaxials of the cryostat. The two ground planes (G in Fig. 3.3(A)) of the CPW were grounded to the housing box. The central region of the CPW is highly constricted for an enhancement of the microwave field at the sample position while maintaining the 50 Ohm impedance matching requirement for optimal microwave transmission through the circuit. This constriction leads to a much higher sensitivity of our CPW compared to commercially available ones and often makes it possible for the detection of weaker signals. As shown in Fig. 3.3(A), the microwaves flow through the central line of the CPW along the z-axis of the considered coordinate system where the CPW plane lies in the y-z plane, with the x-axis being out of the plane (OOP) direction. This chosen direction of the microwave ac current with respect to the CPW geometry gives no rf magnetic field in the z-axis. The rf field felt by a thin film

sample position directly atop the CPW lies along the y-axis, with a small component along the x-axis, corresponding to the relatively smaller thickness of the CPW compared to the width of its central line. Correspondingly, the rf field can be written as $(H_{\text{rfx}}, H_{\text{rfy}}, 0)$. The relative orientation of the applied static field at the sample position with respect to the chosen coordinate system is shown in terms of the polar angles θ and ϕ in Fig. 3.3(B). This choice of coordinate system with respect to the CPW and a planar sample mounted on top of it ensures the sample plane being the y-z plane and the x-axis being the direction perpendicular to the sample plane. We will be referring to this coordinate system while explaining the results of our spectroscopic measurements.

3.3 Results and discussion

The results of our low frequency spectroscopic measurements are described based on the stoichiometric composition of the samples used and each part is further classified into many different parts prevailing to the nature of the measurement. A comparative analysis based on the results for the two stoichiometric samples is performed in the end of this section.

3.3.1 Measurements on MnBi_4Te_7 sample

We have performed a series of measurements on MnBi_4Te_7 ($n=1$) as a function of the direction of the applied field, the temperature, and the frequency used. These results are classified into field rotation measurements, temperature dependent measurements, frequency dependent measurements, and 18GHz measurements. Additional results for the high temperature measurements are discussed together for both stoichiometric compounds in a separate section.

3.3.1.1 Field rotation measurements at low frequency

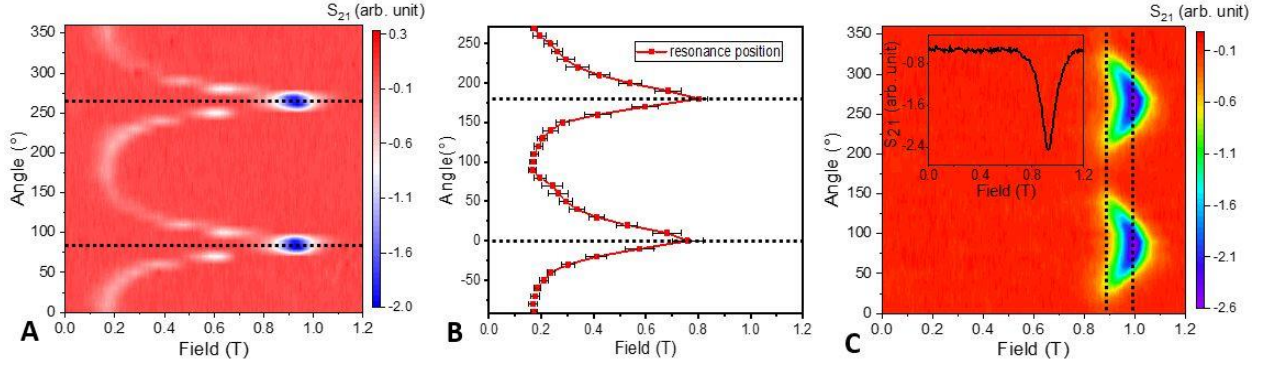


Figure 3.4: Results for the field rotation measurements performed on MnBi_4Te_7 at $T = 7\text{K}$ and $f = 7\text{GHz}$ frequency. A sample resonance signal is shown in the inset in (C). (A) A contour plot for the field rotation measurements performed along the x - y plane (OOP) direction where the angle values correspond to θ of the considered field orientation system. 0° and 90° on the contour correspond to the $+x$ - and the $+y$ -axis respectively and it continues to rotate in that way until coming back to the starting position. The two horizontal dotted lines passing through 85° and 265° represent angle positions corresponding to the maximum field position of the signal. (B) A plot for the resonance position as a function of field angle along the OOP direction defined by z - x plane i.e., θ rotation for ϕ fixed at 0° . 0° and 90° on the contour correspond to $+z$ - and $+x$ -axes respectively and it continues to rotate in that way until coming back to the starting position. The two horizontal dotted lines passing through 0° and 180° show angle positions corresponding to the maximum field position of the signal and represent the positions for applied field along the in-plane (IP) direction. (C) A contour plot for the field rotation measurements performed along the corrected IP direction (see the next section (3.3.1.2) for details) defined as a plane perpendicular to the easy axis defined by 88.5° and 355° for the values of θ and ϕ respectively. Angles 0° and 90° on the contour correspond to the corrected $+z$ - and $+y$ -axes of the newly defined sample plane respectively, and the rotation continues along the modified $+z$ to $+y$ to $(-)$ z direction. The two vertical dotted lines represent the maximum and minimum field positions for the signal.

A set of measurements for the rotation of the applied magnetic field were performed in all the three planes defined by the principal axes shown in Fig. 3.3(B) on a MnBi_4Te_7 single crystal at $T = 7\text{K}$ and $f = 7\text{GHz}$. A rotation in the y - z plane represents the in plane (IP) rotation while the rotations in x - y and x - z planes represent the out of plane (OOP) rotations with respect to the planar sample used in the measurement. A sample resonance curve obtained for the applied field along $+y$ -axis is shown in the inset of Fig. 3.4(C). A set of three detailed rotations were performed in step of 10 degrees along all three principal planes and observed results for the x - y , z - x and y - z planes are shown in Fig. 3.4(A), (B) and (C) respectively. Fig. 3.4(A) presents the contour plot for field rotation measurements performed in the x - y plane, i.e., rotation

by an angle ϕ while keeping θ constant at 90° . In Fig. 3.4(A), 0° corresponds to the direction of the field along the $+x$ -axis, 90° corresponds to the direction of the field along the $+y$ -axis, and it continues to rotate in that way until coming back to the starting position at 360° . A clear modulation of the signal by about 0.8T is observed with respect to the applied field angle. The modulation is sharp around the maximum positions which correspond to the IP direction and relatively flat around the minima positions, corresponding to the field along the OOP direction. The modulating behavior of the observed signal reveals the axial nature of this system where the position of the minima, i.e., the OOP direction, corresponds to the easy magnetic axis, and the position of the maxima, i.e., the IP direction, corresponds to the hard plane of the system. This observation agrees with the predicted easy axis nature of this compound. From the position of the sharp maxima, occurring at 85° and 265° , the minima are determined to lie at 355° (or -5°) and 175° . Under normal circumstances, for a planar sample like the one used in this measurement, one would expect 90° and 270° to be the positions of the maxima, differing by 5° in our observation. We attribute this 5° mismatch between the expected and observed positions to the misalignment of the sample/sample holder in the magnetic field. Further measurements were carried out correcting this misalignment during the field sweeps.

Fig. 3.4(B) shows the angle versus field plot for the measurements along the other OOP direction, i.e., x - z rotation. The resonance positions and the corresponding error, proportional to the signal width, were extracted from the resonance curves and plotted as a function of the applied field angle in Fig. 3.4(B). In the figure, 0° (180°) corresponds to the IP direction (along the $+(-)$ z -axis), while 90° (270°) corresponds to the OOP direction (along $+(-)$ x -axis). Unlike in the case of the x - y rotation, the maxima lie in the expected positions of IP field directions i.e., at 0° (180°). This means the minimum positions lie along the considered OOP direction for this plane and the direction of the magnetic easy axis is determined to lie along 90° . There is a little shift in the data points around 90° and 270° , from the expected parabolic nature and occurs in two identical positions separated by 180° which is assumed to be related to the crystallography of the studied sample crystal. Both the OOP field rotations i.e., x - y and x - z rotations, show the easy axis

nature of the MnBi_4Te_7 compound with the magnetic easy axis along the OOP direction shifted by 5° in the ϕ direction of the considered coordinate system and the signal modulation shows the change in anisotropy while moving from OOP to IP direction or vice-versa.

Fig. 3.4(C) shows the contour plot for the field rotation measurements within the sample plane using a corrected IP direction. With our initial observation for the IP rotation not matching with the expected isotropic nature of the sample plane (original IP rotation direction), we adjusted the rotation algorithm to account for the misalignment observed in the x-y rotation as well as the possible misalignments that could be caused while mounting the sample/sample holder in the cryostat by adopting rotations along the corrected IP directions. From this analysis we determined the magnetic easy axis to be aligned along the direction defined by $\theta_{\text{ea}} = 88.5^\circ$ and $\phi_{\text{ea}} = 355^\circ$ in the considered coordinate system (see the next section (3.3.1.2) for more details). A field rotation measurement was then performed along a plane perpendicular to the direction of the newly defined easy axis. The contour plot shown in Fig. 3.4(C) represents the result obtained for the corrected IP rotation. Compared to all other rotations performed for the IP rotation of this sample under similar conditions, this rotation has the lowest modulation in field ($\sim 0.1\text{T}$) and is more symmetric around the expected IP (90° and 180°) directions of the applied field (see section 3.3.1.2 for details on different IP rotations performed). Two points to note from this plot are: (i) The observation of a small but finite modulation for this IP rotation, even after correcting for the misalignments, illustrates the existence of a small in plane anisotropy in this compound (i.e., corrugated hard anisotropy plane); and (ii) The signal strength is maximum when the dc and rf fields are parallel (y-axis) while the resonance vanishes when the dc field is perpendicular to the rf field. As discussed in the following section, this is contrary to the expectation in a ferromagnetic system and points towards an antiferromagnetic origin of the resonances observed in these systems.

3.3.1.2 In plane measurements and corrugated sample plane

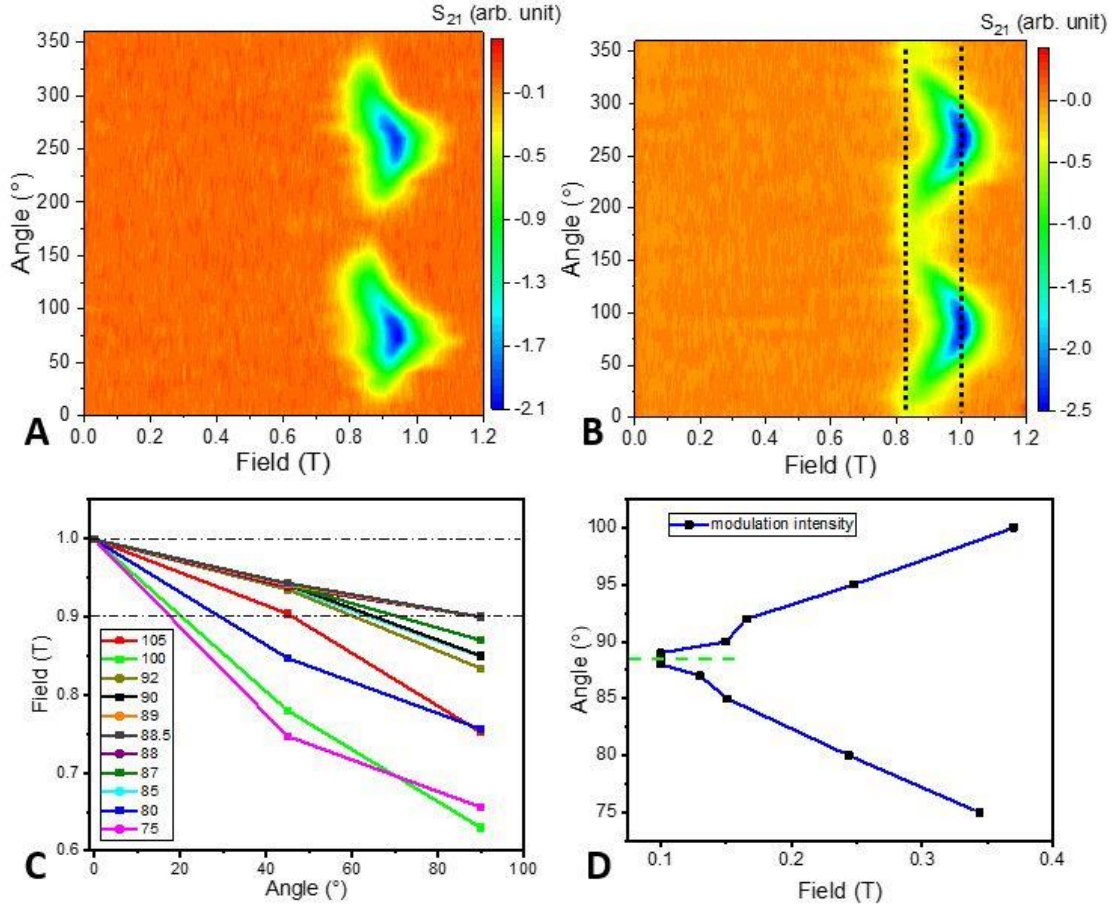


Figure 3.5: (A) Contour plot for the in-plane (IP) field rotation measurement on $MnBi_4Te_7$ at 7GHz and 7K along the y-z plane of the considered coordinate system. In the plot 0° and 90° correspond to + z and +y axis respectively and rotation completes in that direction. (B) represent the contour plot for the modified sample plane which is perpendicular to the easy axis defined by 80° and 355° for the angles θ and ϕ respectively. In the plot 0° and 90° correspond to modified + z and +y axis respectively and rotation completes in that direction of rotation. (C) A plot of the resonance positions of three different rotation angle values: 0° , 45° and 90° for different θ planes defined by the angles in the legend. In this graphic, the 90° curve corresponds to the field rotation in the z-x plane. (D) A plot of the θ plane angle vs the maximum modulation obtained from the rotations in plot (c). The θ value for the direction of the easy axis is given by the minimum field modulation plane i.e., 88.5° represented by the green dotted line.

Different in-plane (IP) field rotation measurements were performed at $T = 7K$ and $f = 7GHz$ to determine the nature of the anisotropy within the sample plane. Figure 3.5(A) presents the contour plot for the IP field rotation, i.e., rotation along the y-z plane, where 0° corresponds to the + z-axis, 90° corresponds

to + y-axis and the rotation completes in the (-) y to + z to + y direction of the chosen coordinate system. In this graphic, we observe a slight modulation, of about 0.1T, in the signal position for the IP rotation which is suggestive of the existence of an IP asymmetry breaking the isotropic hard plane anisotropy. The signal is also not symmetric with respect to the positions of the y- and the z-axis field directions across which it is supposed to be symmetric considering proper sample alignment. We observe symmetric positions to be off by 10° from their expected positions of the applied field which are supposed to lie along the principal axes directions.

To account for this observed IP modulation and the symmetricity of the signal, we considered the 5° misalignment observed in the x-y rotation (see Fig. 3.4(A)) and the 10° off positioning of the expected symmetry positions in the y-z rotation. Considering both these effects, the easy axis should lie along the direction defined by $\theta_{ea} = 80^\circ$ and $\phi_{ea} = 355^\circ$ respectively. The plane perpendicular to this newly defined easy axis was considered to be the sample plane and a new field rotation measurement was performed in the new plane. The results are shown in Fig. 3.5(B). From this contour plot, the signal is highly symmetric with respect to the position of 0° and 90° but the observed modulation is even higher than in the previous case. From this we conclude that the considered ϕ coordinate of the easy axis, which was defined by the x-y rotation, is reliable but the θ angle is to be determined again. Then by fixing phi at 355° , we performed field rotation measurements along different theta planes for 0° , 45° and 90° , and the corresponding resonance positions were plotted as shown in Fig. 3.5(C) where each curve represent the data for corresponding θ plane given in the legend. From these curves the maximum observable field modulation for each θ plane was calculated as the difference in the resonance position for the angles 0° and 90° of the applied field and was plotted as a function of the corresponding plane angle as shown in Fig. 3.5 (D). In the Fig. 3.5 (D), the modulation is minimum for 88° - 89° range which correspond to the theta plane passing through the magnetic easy axis. In this way the theta coordinate for the easy axis was determined to be 88.5° . From this determination of the easy axis, we performed another IP field rotation measurement for the corrected sample plane perpendicular to the easy axis determined by the coordinates (88.5° and 355°)

in the chosen coordinate system and obtained the plot shown in Fig. 3.5 (C) of the main text. Even after correcting the easy axis position, we still observe the field modulation shown in the plot which indicates the existence of a small in plane symmetry breaking giving rise to a corrugated hard anisotropy plane.

3.3.1.3 Temperature-dependent measurements

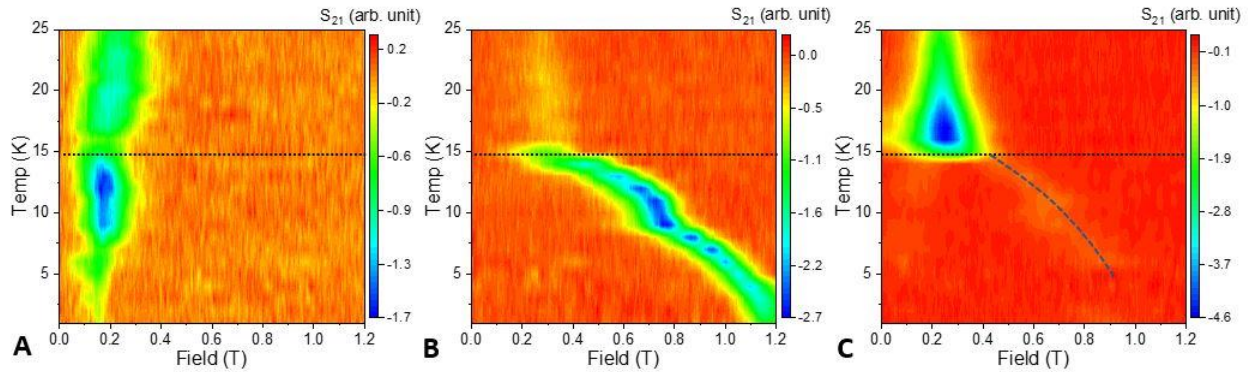


Figure 3.6: Results from the temperature and the frequency dependent measurements are shown in upper and lower panels respectively. (A), (B) and (C) represent the contour plots for the temperature dependent measurements performed at $f = 7\text{GHz}$ in the temperature range from 1K to 25K for the direction of the applied field along the x-, y- and z-axes respectively. The horizontal dotted lines in each of the plots correspond to the transition temperature for this material.

Temperature-dependent measurements were performed in the 1-25K at $f = 7\text{GHz}$ for the magnetic field along all three principal axes of the chosen coordinate system. The effect from the misalignment discussed in the previous section is considered to be minimal and the overall picture is assumed to be unaffected by this. Fig. 3.6(A), (B) and (C) represent contour plots for the temperature-dependent measurements for the magnetic field applied along the x-, y- and z- axes, respectively. As seen in Fig. 3.6(A), the resonance position remains almost constant with increasing temperature up to around 15K, corresponding to the Neel transition temperature (shown by dotted horizontal line), after which it widens and moves slightly towards higher fields with further increasing the temperature. The signal linewidth, which is very narrow at low temperatures, gradually increases up to around 10K and remains almost constant with further increase, although the resonance presents a change in shape around the transition temperature as well. The signal in Fig. 3.6(B) for the measurement along y-direction shows a drastic change

in behavior at the transition temperature, in terms of both intensity and modulation. The signal, which is strong below the transition temperature, becomes very weak and almost disappears above the transition temperature. Also, the resonance moves to lower fields in increasing temperature, staying constant above the transition temperature. This abrupt change in behavior is observed for the first time in this compound, and we attribute it to the antiferromagnetic nature of the signal below the transition temperature, as discussed below. A slight change in signal behavior around 7K is attributed to a systematic factor related to the change in the sensor used to read the temperature of the sample. In Fig. 3.6(C) for the measurement for the field along the z -direction, we observe a similar behavior in terms of signal modulation to that of the y -axis measurement but with a completely opposite trend of the signal intensity with respect to the other IP measurement. Unlike in the y -axis temperature dependence, the signal intensity for the z -axis measurement is weak at temperatures below the transition temperature and becomes strong above the transition temperature with the onset of a strong signal across the transition temperature. In the plot, the signal behavior below the transition temperature is illustrated by a dashed line to guide the eye. As discussed in the previous section this is indicative of the antiferromagnetic nature of the resonance mode below the transition temperature, which becomes paramagnetic/ferromagnetic at higher temperatures. Note that above the transition temperature, the resonance vanishes when the field is applied parallel to the rf field, as seen in Fig. 3.6(B) (y -axis), and becomes strong when the field is applied perpendicular to the rf field, as seen in Fig. 3.6(C) (z -axis), as expected from the orthogonality required in spectroscopy between the applied magnetic field and the quantization axis of the system (here set by the magnetic field in the paramagnetic/ferromagnetic case). The fact that the relative strength of the resonances reverses below the transition temperature means that the quantization axis is determined by the antiferromagnetic interaction and not the applied field, resulting in a strong/weak resonance when the applied field is parallel/perpendicular to the rf field, contrary to the paramagnetic/ferromagnetic case. We understand this still as a result of the applied field, which tilts the sublattice magnetizations (the Neel vector) to a direction perpendicular to the applied dc field above the spin flop transition. In other words, when a field is applied, the Neel vector (quantization axis) rotates into a direction orthogonal to the applied field. When the applied

field is parallel to the rf field (y-axis), indeed, the Neel vector is perpendicular to the rf field, fulfilling the requirement for the absorption of the photon (i.e., rf field perpendicular to the magnetic quantization axis). These results are different from the ones observed in measurements at high-frequency by other groups [31-33], where they observe no such drastic change in the signal behavior across the transition temperature and attribute to a ferromagnetic origin.

3.3.1.4 Frequency dependent measurements

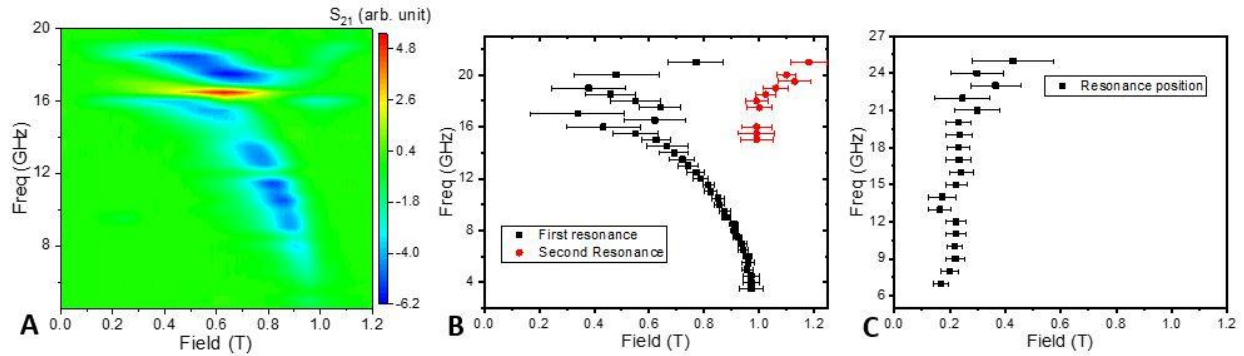


Figure 3.7: Results for the frequency dependent measurements performed at $T = 7K$. (A) A contour plot for the frequency dependence along the IP direction (y-axis) of the applied field. (B) A frequency vs field plot for the data corresponding to (a). (C) A frequency vs field plot for the frequency dependence along the OOP direction (x-axis) of the applied field. The errors in (B) and (C) are proportional to the width of the corresponding signals.

Frequency dependent measurements were performed for the field along two orthogonal directions of the sample. Fig. 3.7(A-C) present the results for the frequency dependent measurements performed at 7K for the applied magnetic field along the IP and the OOP directions. Fig. 3.7(A) shows the contour plot for the IP frequency dependence and Fig.3.7(B) shows the corresponding frequency versus field plot for the resonance positions and the corresponding error proportional to the signal width. In both of these graphs, we observe a very clear resonance at frequencies up to around 14GHz, after which the signal becomes broad and starts to behave differently. At frequencies above 15GHz, an additional weaker resonance appears at high field, which is shown as a second resonance in Fig. 3.7(B). Up to 16GHz, the resonance marked as first resonance decreases non-linearly with increasing frequency, which is a unique observation for this

system. At around 17GHz a transition occurs, with a change in sign (the resonance becomes a peak instead of a dip), as can be clearly seen as a change in the color on the contour plot in Fig. 3.7(A). At higher frequencies, both resonances appear to move towards higher fields with increasing frequency and become broader. For the OOP frequency dependence (Fig. 3.7(C)), the resonance responds less to the applied field, moving slightly towards high fields in increasing frequency. We observe similar behavior for both frequency dependences at 4K measurements (see the next section (3.3.1.5) for details). This frequency behavior is definitively different from that expected from a ferromagnetic sample, but does not either correspond to the expectation from a simple easy axis antiferromagnetic system below the spin-flip transition. Although we lack a clear interpretation of the frequency modulation of the observed resonances, this complex behavior and others observed in this sample and described in the following sections make us conclude that they result from the competition of closely commensurate in-plane ferromagnetic and inter-plane antiferromagnetic interactions, leading to an antiferromagnetic system with low ordering temperature, low zero-field dynamical modes, and low spin-flip transition fields, and making the field-frequency-temperature range experimentally explored to coincide with a complex energy landscape associated to the magnetic modes of the system.

3.3.1.5 Frequency dependent measurements at 4K

Low temperature frequency dependent measurements were performed on the MnBi₄Te₇ sample at 4K for the applied field along the IP and the OOP direction. Fig. 3.8(A) and (B) respectively represent the IP and the OOP frequency versus field plots where the resonance positions and the corresponding errors, proportional to the signal width, were extracted from the raw spectrum. From Fig. 3.8(A) for the IP frequency dependence, we observe almost the same behavior to that of the 7K measurements (see Fig. 3.7(B)). The signal moves towards lower fields with increasing frequency in a non-linear manner and we also observe double resonance features at frequencies above 15GHz. The signal width also increases with increasing frequency beyond 14GHz. The only observable difference between the measurements at 4K and 7K is the behavior of the signal at the higher frequencies. In the case of the 4K measurements both

resonances move towards lower fields even after 14/15GHz where they showed a different trend in the 7K measurement. Fig. 3.8(B) for the OOP frequency dependence at 4K show a similar behavior to that observed in the case of the 7K measurement. There is a weak frequency dependence of the resonance mode to the applied field, moving higher in field with increasing frequency. As discussed in the previous section for the 7K frequency dependent measurements we attribute this to the complex energy landscape associated to the magnetic modes of the system.

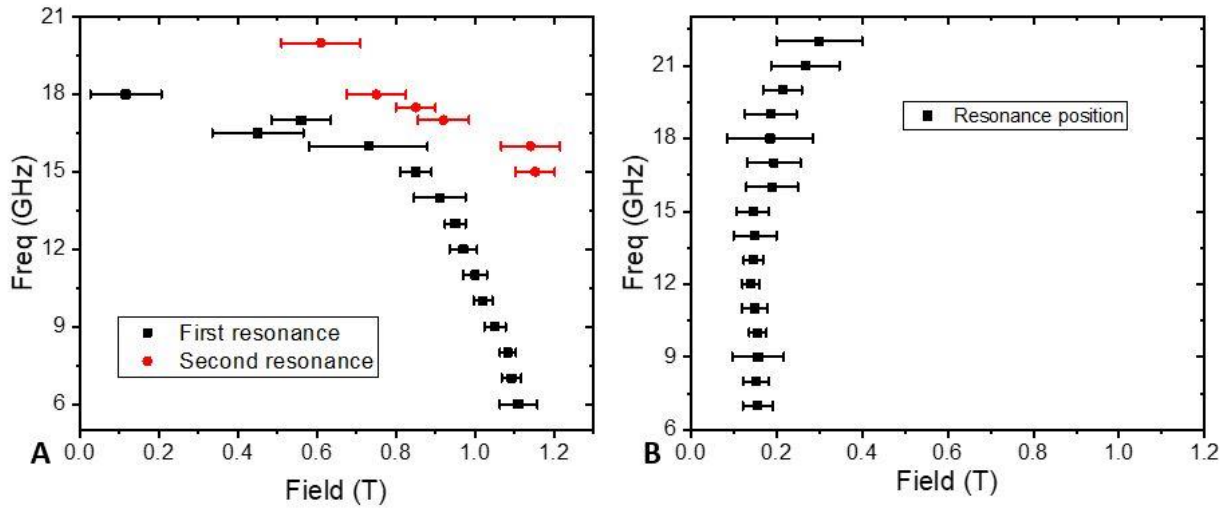


Figure 3.8: Results for the frequency dependent measurements performed on the $MnBi_4Te_7$ sample at 4K. (A) IP frequency dependence for the applied field along the y-axis of the considered coordinate system. (B) OOP frequency dependence for the applied field along the x-axis. The errors in both the data are proportional to the width of the corresponding signals.

3.3.1.6 Field rotation measurements at high frequency

Trying to shed light into the nature of the observed resonances we have performed a series of different measurements rotating the magnetic field at a fixed frequency (18GHz) and varying the temperature while fixing the applied field at the three characteristic directions.

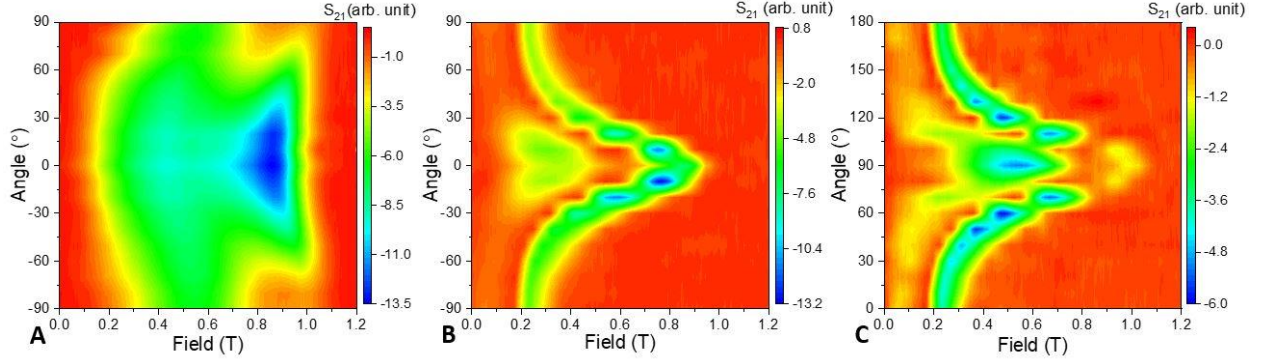


Figure 3.9: Results for the field rotation measurements performed at $f = 18\text{GHz}$ and $T = 7\text{K}$. (A)-(C) represent the contour plots for the field rotations along the y-z, x-z and x-y planes respectively. In (A) the θ rotation is performed keeping ϕ at 90° from (-) y-axis (-90°) to +y-axis (90°) through +z-axis (0°). In (B) the θ rotation is performed keeping ϕ at 0° from (-) x-axis (-90°) to +x-axis (90°) through +y-axis (0°). In (C) the ϕ rotation is performed keeping θ at 90° from +x-axis (0°) to (-) x-axis (180°) through +y-axis (0°)

Field rotation measurements at $f = 18\text{GHz}$ and $T = 7\text{K}$ were performed along all three principal planes of the considered coordinate system to follow the evolution of the two peaks observed at high frequencies in the IP frequency-dependent measurement shown in Fig. 3.7(B). Fig. 3.9(A) represents the field rotation measurement performed in the sample plane direction where -90° , 0° and $+90^\circ$ represent the applied field along + y-, + z- and (-) y- axis, respectively. As shown in Fig. 3.4(C) for 7GHz, the nature of the modulation of these broad signals is in the similar direction, where the signal along the y-axis appears to be at higher field compared to the one along the z-axis for both resonances. But the signal intensity for these resonances show opposite behavior as that seen at 7GHz, i.e., maximum intensity for the rf and the dc field perpendicular to each other and minimum intensity when they are parallel. The signal at the higher field becomes much weaker in intensity compared to the signal at the lower field for the applied field along the \pm y-axis while both of them remain relatively strong for the field along the z-axis. Fig. 3.9(B) shows the contour plot for the field rotation along the OOP direction in the x-z plane where -90° , 0° and 90° represent the applied field along + x-, + z- and (-) x-axis, respectively. Both resonance modes follow the trend of the modulation seen in the out of plane rotation at 7GHz and 7K shown in Fig. 3.4(A). This behavior again supports the expected easy axis nature of the measured sample. Moreover, the resonance at higher field is

strong enough to be observable along the OOP directions (0° and 180°) and hence we see it in the frequency dependent measurement shown in Fig. 3.7(C), while the lower field resonance becomes very weak when moving away from the IP direction (90°) and is not clearly observed in the OOP frequency dependent measurement. The alternative OOP rotation for the x-y plane is shown in Fig. 3.9(C) where 0° , 90° and 180° correspond to the field direction along + x-axis, + y-axis and (-) x-axis, respectively. In this case the signal behavior is very similar to that in Fig. 3.9(B) in terms of modulation and intensity of the resonances, with the exception of the IP direction, where the intensity is higher for the mode at lower field than the one at the higher field, opposite to that of the x-z plane rotation. We associate this again to the orthogonality between the rf field and the magnetic quantization axis of the system required by FMR and the antiferromagnetic nature of the system, as discussed above.

For completion, a set of three temperature-dependent measurements at 18GHz were also performed in the range of temperatures from 250mK to 25K by applying the magnetic field along all three principal axis directions. Fig. 3.10(A), (B) and (C) represent contour plots for the 18GHz temperature-dependent measurements for the field along x-, y- and z-axes, respectively. All these contour plots involve combination of two contours, one in the temperature range from 250mK to 6K with data taken in steps of 0.25K and other one from 6K to 25K with data taken in steps of 1K. Three different resonance behaviors are observed in all the three plots. In Fig. 3.10(A), there is a mode at temperatures below 5K at a field around 0.17T which appear to split into two around that temperature with the mode at the lower field being weak and almost constant in field with further increasing temperature, while the other relatively strong signal at the higher field moves slowly towards higher fields up to around 14K, corresponding to the transition temperature. Around the transition temperature the signal at the lower field disappears while the signal at the higher field continues to move higher in field non-monotonically, becoming almost constant at the highest temperatures. In Fig. 3.10(B) for the applied field along the y-axis, we can see a broad and relatively strong signal in the higher field position at the lower temperatures and a weak signal towards the lower field position. Around 5K the signal at the higher field becomes broader and splits into two, one

broad and strong at lower field and other relatively weak and narrow at the higher field. The strong broad split signal moves towards lower fields and gets merged with the weak signal of low field side. The combined signal then moves slowly towards lower fields and disappears around the transition temperature. The other split signal moves slowly towards lower fields until around 20K and becomes almost constant in field with further increasing temperature. The signal intensity of the signal surviving at the higher temperature decreases with increasing temperature, like the one observed for the 7GHz measurement shown in Fig 3.6(B). In Fig. 3.10(C) for the z-axis signal, we observe a similar trend of different resonances as that of Fig. 3.10(B), with the only difference in terms of relative intensity of the resonances. Difficult to see in this plot, there are also three distinct resonances at low temperature. The signal appearing towards the lower field at lower temperatures and the signal which continues to survive at high temperatures are much stronger than the ones observed in Fig. 3.10(B). The merging of the three resonances into two observed in Fig. 3.10(B) also occurs here at 5K, and the combined resonance finally disappears around the transition temperature.

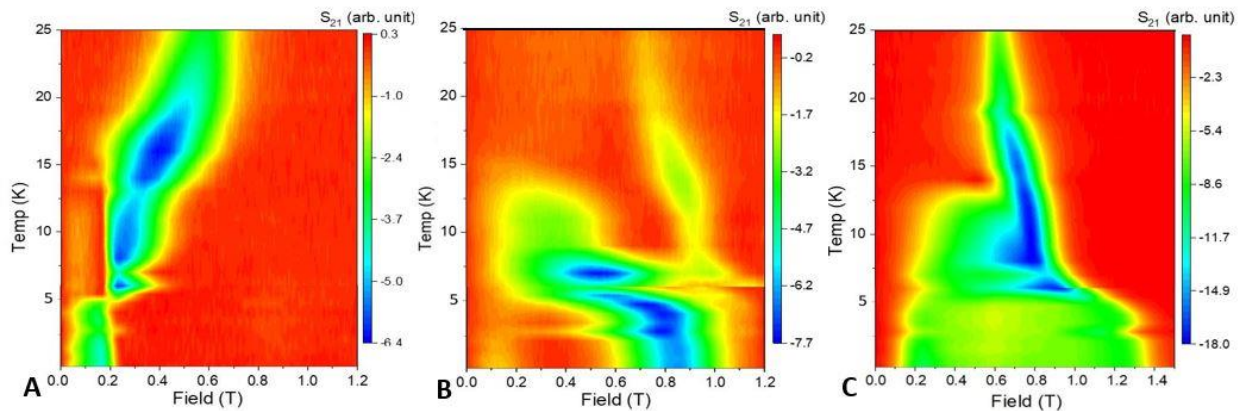


Figure 3.10: Results for the temperature dependent measurements performed in the range 250mK to 25K at $f = 18\text{GHz}$ for the applied field along all three principal axes directions of the considered coordinate system. (A)-(C) respectively represent the contour plots for the applied field along x-, y-, and z-axes.

These measurements reveal a very complex behavior likely associated to a sophisticated set of AF dynamical modes arising from the close competition of the in-plane ferromagnetic and inter-layer

antiferromagnetic interactions. Further detailed field rotation measurements at low temperatures revealing the complex dynamical behavior of the multiple resonances observed in figure 3.7 are detailed in the next section (3.3.1.6). Although we lack a complete understanding of the observed behaviors, we are confident in the overall interpretation of the magnetic behavior of this sample in terms of antiferromagnetic ordering with a characteristic and sophisticated energy landscape, as probed by the energy-field-frequency range of our experiments.

3.3.1.7 18GHz low temperature measurements on the $MnBi_4Te_7$

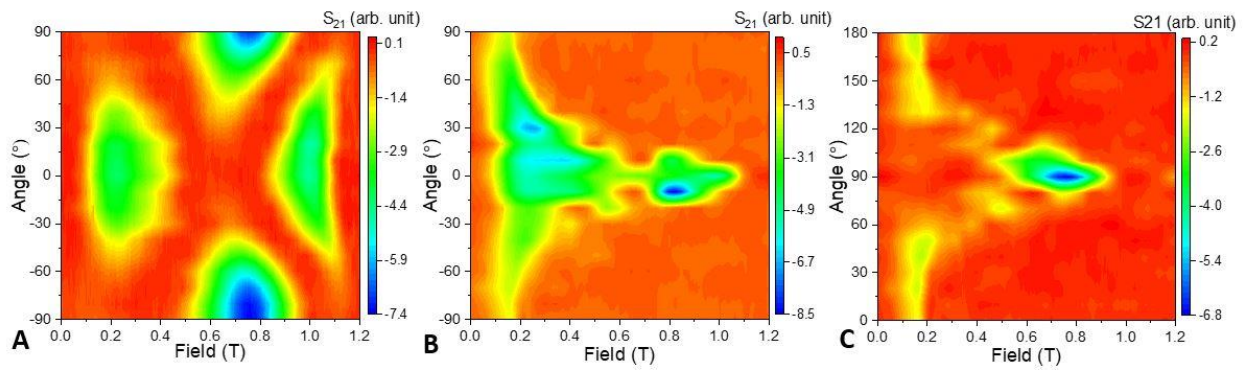


Figure 3.11: Field rotation measurements at 18GHz frequency and 4K temperature. In the figure, (A), (B) and (C) represent the contour plots for the applied field along y-z, x-z and x-y planes respectively. In plot (A) the θ rotation is performed keeping ϕ at 90° from (-) y-axis (-90°) to + y-axis (90°) through + z-axis (0°). In plot (B) the θ rotation is performed keeping ϕ at 0° from (-) x-axis (-90°) to + x-axis (90°) through + y-axis (0°). In plot (C) the ϕ rotation is performed keeping θ at 90° from + x-axis (0°) to (-) x-axis (180°) through + y-axis (0°).

In addition to the 18GHz measurements discussed in the previous section, more field rotation measurements at lower temperatures and a temperature dependent measurement along an intermediate IP field direction were performed to follow the nature of the multi-resonance behavior observed at lower temperatures in $MnBi_4Te_7$ (see the previous section (3.3.2) for details). Fig. 3.11 shows plots for the field rotation measurements performed at 4K along all three principal planes of the considered coordinate system. In Fig. 3.11(A) for the IP rotation, one can see three clear resonance features at some angles (e.g., 45°), which modulate in terms of field and intensity with change in the applied field direction and only one or

two of them becomes visibly clear at some other angles like at 0° and $\pm 90^\circ$. The two resonances at the higher field positions modulate in the similar pattern but they differ in terms of the signal intensity. The resonance at the highest field position is strong when the rf and the dc field are perpendicular to each other i.e., at 0° along the z-axis, and weak when they are parallel to each other, i.e., at $\pm 90^\circ$ along the $\pm y$ -axis. The opposite is true for the signal observed in the intermediate fields, but a similar pattern is observed for the signal at the lowest field position which appears to modulate in the opposite direction to that of the two resonances at the higher field positions. In Fig. 3.11(B) for the OOP rotation along the x-z plane, one can see a similar behavior of the two signals in terms of the modulation as seen at the 7K (see Fig. 3.9 for details). The resonance towards the higher field position moves to the lower field quickly while moving away from the IP direction i.e., 0° . Also, as evident from Fig 3.11(A), we only see two clear features while applying the field along z-direction where the other signal, clear along $\pm y$ -axis, doesn't appear clearly in this OOP rotation. Only one clear signal is observed while applying the field close to the OOP direction i.e., at $\pm 90^\circ$. Fig. 3.11(C) for another OOP rotation for the x-y plane shows a similar behavior of the signal modulation for the observed signal which moves quickly towards the lower field while moving away from the IP direction i.e. 90° .

To investigate the behavior of the three resonances observed at 4K IP rotation measurements, another IP field rotation at 250mK was performed and the result is shown in Fig. 3.12(A). From this plot, the nature of all three resonances can be clearly seen both in terms of the field modulation and the signal intensity. The resonances at the lowest and the highest field positions behave in a similar way in terms of the signal intensity for which they have a maximum signal when the rf and the dc field are perpendicular to each other i.e., at 0° along +z-direction, and minimum when they are parallel to each other i.e., at $\pm 90^\circ$ along $\pm y$ -direction, but they modulate in opposite directions. The resonance in the intermediate field has the opposite nature in terms of the signal strength to that of the other two features but modulates like the one observed in the higher field position. These results illustrate the complexity associated with the behavior of the AFM dynamical modes in this sample.

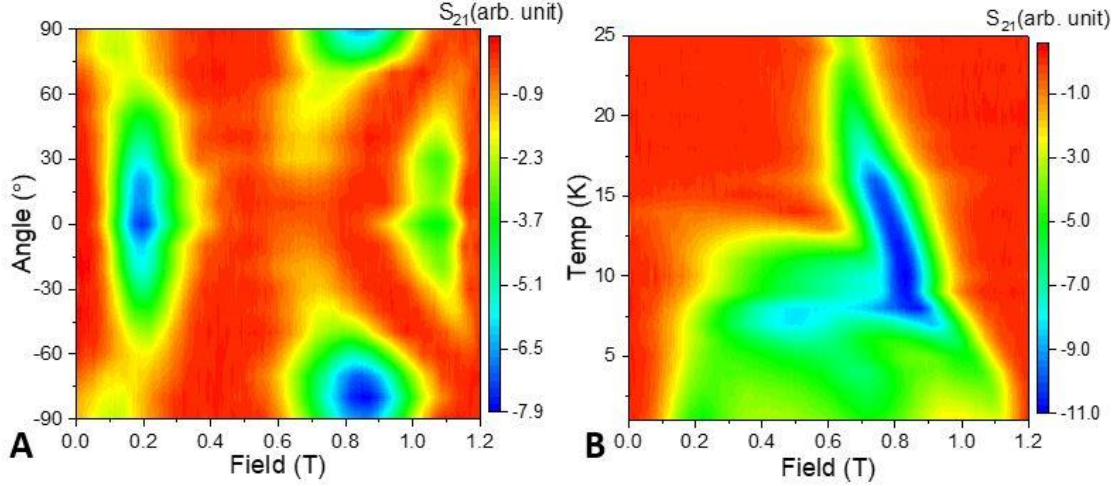


Figure 3.12: (A) contour plot for the field rotation measurement performed at 18GHz and 250mK along the y-z plane. In the measurement the θ rotation is performed keeping ϕ at 90° from (-) y-axis (-90°) to + y-axis (90°) through + z-axis (0°). (B) contour plot for the temperature dependent measurement performed at 18GHz in the range 1K to 25K in step of 1K while applying the field along -40° direction of plot (A).

For a better understanding of the temperature dependence of the three resonances observed in the 250mK IP field rotation, we performed another temperature dependent measurement along the field direction corresponding to -40° in Fig. 3.12(A) along which all three resonances are clear and obvious to follow. Fig. 3.12(B) represent the contour plot for that temperature dependent measurement performed in the range 1K to 25K in step of 1K. In the plot, the two resonances at the lower fields merge at a temperature around 6K and the combined broad signal slowly becomes weak, finally disappearing around the transition temperature (14K). The other signal at the higher field position moves slowly towards the lower field with increasing temperature and changes slope across the transition temperature. At higher temperature this signal becomes almost constant in field with further increasing temperature. The nature of the signals in this plot is like the ones at the temperature dependent measurements at 18GHz with the applied field along the y-axis and the z-axis given in the main text (see Fig. 3.10 for details) but all the three signals are clearer and easy to follow.

3.3.2 Measurements on the $\text{MnBi}_6\text{Te}_{10}$ sample

We have also performed a series of measurements on the $\text{MnBi}_6\text{Te}_{10}$ ($n=2$) compound. In this system there is another non-magnetic Bi_2Te_3 layer between the two magnetic layers of MnBi_4Te_7 . Like in the case of MnBi_4Te_7 , measurements were performed as a function of magnetic field strength and direction of application, temperature, and frequency using the same CPW and the results are summarized in the following sections.

3.3.2.1 Field rotation measurements

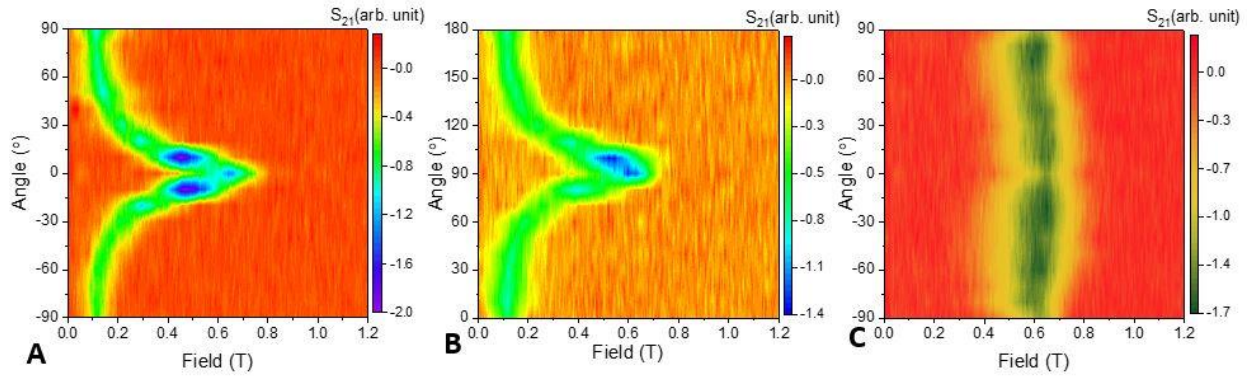


Figure 3.13: Results for the field rotation measurements performed on the $\text{MnBi}_6\text{Te}_{10}$ sample at $f = 8\text{GHz}$ and $T = 7\text{K}$. In the figure, (A)-(C) represent the field rotation measurements the x - z , x - y and y - z planes of the considered coordinate system respectively. In (A) the θ rotation is performed keeping ϕ at 0° from (-) x -axis (-90°) to + x -axis (90°) through + z -axis (0°). In (B) the ϕ rotation is performed keeping θ at 90° from + x -axis (0°) to (-) x -axis (180°) through + y -axis (0°). In (C) the θ rotation is performed keeping ϕ at 90° from (-) y -axis (-90°) to + y -axis (90°) through + z -axis (0°).

The field rotation measurements were performed at $f = 8\text{GHz}$ and $T = 7\text{K}$ sweeping the magnetic field at different at different directions along all three principal planes of the considered coordinate system. Fig. 3.13(A), (B) and (C) represent the contour plots for the field rotation measurements along the x - z , x - y and y - z planes, respectively. The y - z plane corresponds to the plane of the sample within a minimal experimental error. From the two OOP field rotation measurements shown in Fig. 3.13(A) and 7(B), the resonance behaves in a similar way to that of the MnBi_4Te_7 sample in terms of the nature of the signal modulation, with the resonance lying at low field ($\sim 0.12\text{T}$) while applying the field along the OOP direction,

($\pm 90^\circ$ in Fig. 3.13(A), and 0° and 180° in the Fig. 3.13(B)), and moving to a maximum field position ($\sim 0.6\text{T}$) when applying the field along the IP direction (0° in the Fig. 3.13(A) and 90° in the Fig. 3.13(B)). This is again indicative of an axial symmetry of the system. The observed resonance intensity is maximum for the field along/close to the IP direction and decreases while moving towards the OOP direction. In both OOP rotations, the maxima in the field position are along the IP direction of the sample. This means the OOP direction of the considered coordinate system corresponds to the magnetic easy axis of the sample. Fig. 3.13(C) is the contour plot for the IP rotation measurement, where 0° and 180° correspond to the field applied along the $\pm y$ -axis, and 90° corresponds to the field along the z -axis. In this case the signal is also slightly modulated ($\Delta H \sim 0.05\text{T}$), but clearly not as much as in the case of MnBi_4Te_7 . We also attribute this small in plane modulation to a corrugation of the hard anisotropy plane of the sample.

3.3.2.2 Temperature-dependent measurements

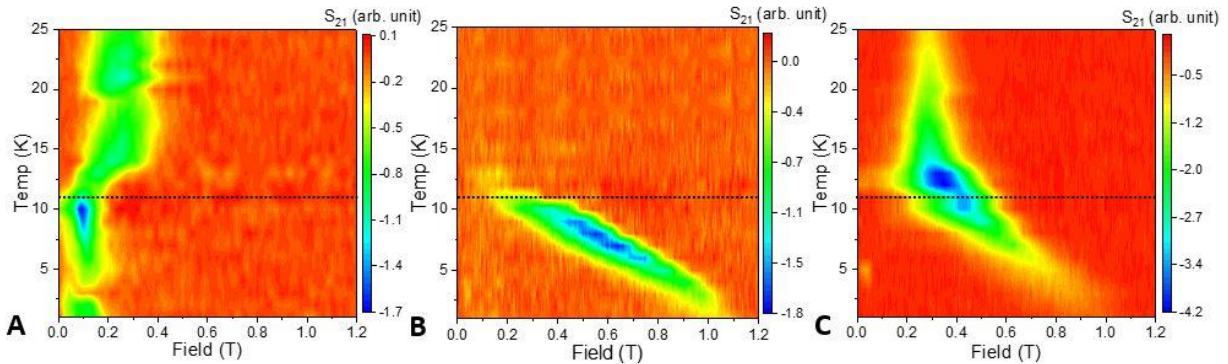


Figure 3.14: Results for the temperature dependent measurements on $\text{MnBi}_6\text{Te}_{10}$ sample performed at $f = 8\text{GHz}$ in the range 1K to 25K . (A)-(C) represent the contour plots for the measurements with applied field along the x -, y - and z -axes, respectively. The horizontal dotted lines in each plot correspond to the transition temperature.

Temperature-dependent measurements were performed for the $\text{MnBi}_6\text{Te}_{10}$ sample at $f = 8\text{GHz}$ in the range 1K to 25K in steps of 1K for the field applied along all three principal axes of the considered coordinate system. The results for these measurements are shown as contour plots in Figure 3.14(A), (B) and (C) for the field along the x -, y - and z -axes, respectively. In Fig. 3.14(A), for the x -axis temperature

dependence, the resonance remains almost constant with increasing temperature up to about 11K (Neel transition temperature for $\text{MnBi}_6\text{Te}_{10}$), and then it moves towards higher fields with further increasing temperature. In Fig. 3.14(B), for the y-axis temperature dependence, the resonance moves towards low field with increasing temperature. The relatively strong intensity at lower temperatures drops abruptly around 11K after which it becomes very weak and difficult to follow. In Fig. 3.14(C), for the z-axis temperature dependence, the resonance, which is relatively weak at low temperature, moves down in field within increasing temperature and becomes stronger and constant above the transition temperature (11K). The behavior of the signal in all these observations is similar to that observed for MnBi_4Te_7 (Fig. 3.6), but in this case the z-axis signal is clear enough to be observable in the contour plot even below the transition temperature. As in the case of MnBi_4Te_7 we attribute this unique temperature dependent behavior to the antiferromagnetic nature of the resonance below the transition temperature, with the system becoming paramagnetic/ferromagnetic at higher temperatures. The lower transition temperature observed in this system is consistent with an expected weaker antiferromagnetic interaction between the magnetic layers due to an increased distance as a result of the added non-magnetic Bi_2Te_3 layer.

3.3.2.3 Frequency dependent measurements

Frequency dependent measurements were performed for the $\text{MnBi}_6\text{Te}_{10}$ sample with the applied field along the IP and OOP directions. Fig. 3.15(A) and (B) represent the frequency versus field plots for the field applied along the y-axis (IP) and x-axis (OOP), respectively. The resonance positions and the corresponding errors, proportional to the signal width, were extracted from the observed spectrum for each frequency. In Fig. 3.15(A), the resonance moves towards low field non-linearly with increasing frequency, almost similar to the case of the MnBi_4Te_7 sample, but with broader resonances occurring at lower magnetic field positions overall as it corresponds to a lower AF interaction energies. Fig. 3.15(B) for the OOP frequency dependence shows a weaker dependence of the resonance position on the applied field, with the resonance moving slowly towards high field with increasing frequency. As explained in the case of MnBi_4Te_7 , these frequency dependence behaviors are attributed to a close competition between the in-plane

ferromagnetic and inter-plane antiferromagnetic interactions, with the latter being even weaker in the case of this sample.

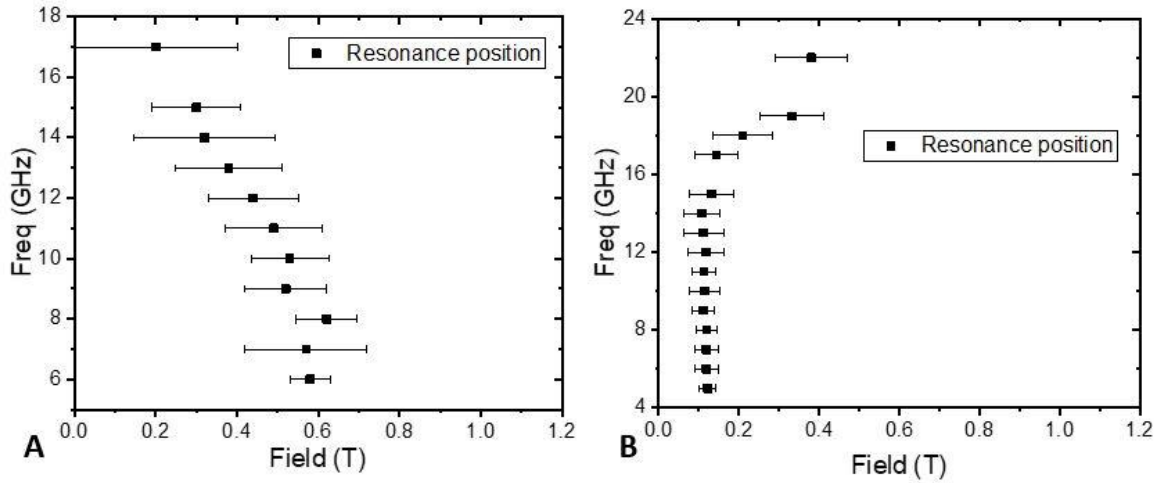


Figure 3.15: Results for the frequency dependent measurements performed on $MnBi_6Te_{10}$ sample at $T = 7K$. (A) represents the data for the IP measurement for the direction of the applied field along the y-axis. (B) represents the data for the OOP measurement for the direction of the applied field along the x-axis. In both the plots the errors are proportional to the width of the corresponding signals.

3.3.3 High temperature measurements in both samples

To understand the behavior of the observed resonances beyond the transition temperature (i.e., 14K for $MnBi_4Te_7$ and 11K for $MnBi_6Te_{10}$) we performed high temperature measurements (25K) of the frequency dependence of the resonance. Figures 3.16(A) and (B) represent the frequency versus field plots for the frequency dependent measurement on $MnBi_4Te_7$ and $MnBi_6Te_{10}$ compounds, respectively, with the field applied along all three principal axes of the considered coordinate system. The result for each direction is represented by a different color (the resonance was not clear enough to be followed at the lowest frequencies). For both compounds and in all directions the resonances move linearly and overlap with each other within the considered error margins. In Fig. 3.16(A) for the 25K frequency dependence for $MnBi_4Te_7$, the data points for the different field directions at a given frequency lie almost on top of each other giving

no signal modulation, even in the OOP rotation, as observed for the 7K measurements as shown in Fig. 3.4(A) and (B). The resonance plot for the field along the y-axis lies slightly right compared to the other curves but still within the considered error margin for the overlap and we attribute this to the existence of a small in plane anisotropy, even at higher temperatures, which is reported in measurements by other groups [32]. In Fig. 3.16(B) for the 25K temperature dependence on $\text{MnBi}_6\text{Te}_{10}$, the data points for different field directions at a given frequency lie almost on top of each other suggesting no signal modulation in the field rotation measurement, even for the OOP rotation.

The observed linear frequency dependence at 25K suggests normal paramagnetic origin of the observed signal at temperatures well above the transition temperature in both compounds.

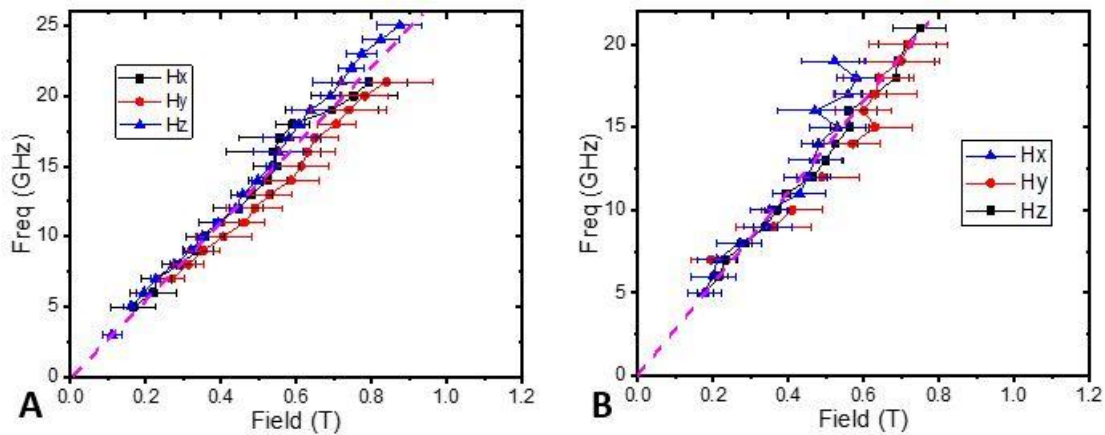


Figure 3.16: Results for the frequency dependent measurements performed at 25K in both sample. Plots (A) and (B) represent the frequency dependent measurements for the MnBi_4Te_7 and $\text{MnBi}_6\text{Te}_{10}$ compounds respectively for the applied field along all three principal axes directions represented by different colors. The magenta lines are the arbitrary lines passing through the representative data of either compound and the origin.

3.3.4 Comparative study at 7GHz between two different stoichiometric samples

Figure 3.17(A) and (B) show the OOP field rotation measurements along the x-y plane of the considered geometry at $f = 7\text{GHz}$ and $T = 7\text{K}$ performed on the MnBi_4Te_7 and the $\text{MnBi}_6\text{Te}_{10}$ compounds respectively. From Fig. 3.17(A), the signal for MnBi_4Te_7 has a modulation of about 0.8T while going from

OOP (the easy axis) direction to IP (the sample plane) direction while that for $\text{MnBi}_6\text{Te}_{10}$ sample is about 0.5T as shown in Fig 3.17(B). This decrease in the field modulation indicates a decrease in the anisotropy energy of this system, which may also be associated to the weaker antiferromagnetic exchange coupling between the two magnetic septuple layers with the insertion of an additional non-magnetic quintuple layer in $\text{MnBi}_6\text{Te}_{10}$ sample. The observation of the field modulation for the OOP rotation in both the compounds correspond to their easy axis anisotropy which is strongly temperature dependent as evident from the temperature dependent measurements on each compound discussed in the main text. We also observe a clear dependence of the observed signals on the transition temperature which depends on the sample stoichiometry. Our measurements show a transition temperature slightly below 15K for the MnBi_4Te_7 and around 11K for the $\text{MnBi}_6\text{Te}_{10}$ compound.

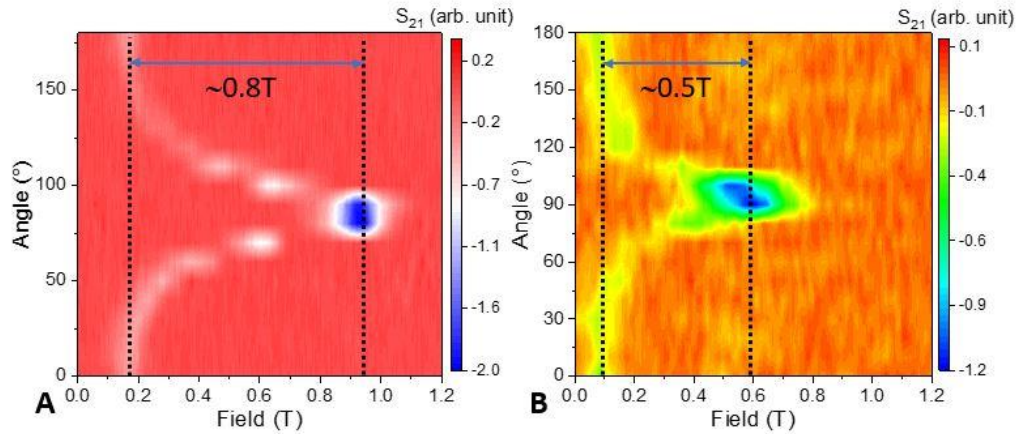


Figure 3.17: Plots for the 7K and 7GHz OOP field rotation measurements along y - z plane performed on the two stoichiometric compounds. Plots (A) and (B) respectively represent the results for the MnBi_4Te_7 and the $\text{MnBi}_6\text{Te}_{10}$ compounds. In both the plots 0° , 90° and 180° represent the field direction along the $+x$ -, $+y$, and $(-)$ x -axis respectively. The two vertical dotted lines in each plot are straight lines passing through the maximum and the minimum signal position whose difference gives the strength of field modulation for each case.

3.4 Conclusion

We have performed a detailed spectroscopic study of single crystals of novel 2D antiferromagnetic topological insulators MnBi_4Te_7 and $\text{MnBi}_6\text{Te}_{10}$ ($n = 1$ and 2 within the $\text{MnBi}_2\text{Te}_4(\text{Bi}_2\text{Te}_3)_n$ family). The

motions of the resonance field positions in the OOP field rotation measurements performed below the transition temperature for each of the compounds show the easy magnetic axis nature of both systems. The small modulation of the resonance signal in the IP field rotation measurements at low temperatures indicates a presence of a small in plane anisotropy within the sample plane in both compounds (corrugated hard anisotropy axis). The IP rotation measurements show a unique behavior in the signal intensity which is opposite to that of the ferromagnets and consistent with the antiferromagnetic nature of the dynamical modes expected in these systems at low temperatures. The temperature dependent measurements confirm a phase transition associated to magnetic ordering as a result of antiferromagnetic coupling between magnetic layers in both systems, with a transition temperature smaller for $\text{MnBi}_6\text{Te}_{10}$ (11K) than for MnBi_4Te_7 (14K) as a result of the increased distance between magnetic layers and a corresponding weakening of the inter-layer antiferromagnetic interaction. Our measurements provide solid evidence for the antiferromagnetic origin of the observed dynamical modes which was not evident in high frequency experiments conducted by other groups [31-33]. The temperature dependent measurements at high temperatures suggest a paramagnetic behavior only for temperatures above the transition temperature, which is further confirmed by the linear frequency dependencies of the resonances observed in experiments conducted at 25K for both compounds.

3.5 References

- [1] Y. Tokura, K. Yasuda, and A. Tsukazaki, "Magnetic topological insulators," *Nature Reviews Physics*, vol. 1, no. 2, pp. 126-143, 2019/02/01 2019, doi: 10.1038/s42254-018-0011-5.
- [2] J. Li *et al.*, "Intrinsic magnetic topological insulators in van der Waals layered MnBi₂Te₄-family materials," *Science Advances*, vol. 5, no. 6, p. eaaw5685, 2019, doi: doi:10.1126/sciadv.aaw5685.
- [3] M. M. Otrokov *et al.*, "Prediction and observation of an antiferromagnetic topological insulator," *Nature*, vol. 576, no. 7787, pp. 416-422, Dec 2019, doi: 10.1038/s41586-019-1840-9.
- [4] C. Hu *et al.*, "A van der Waals antiferromagnetic topological insulator with weak interlayer magnetic coupling," *Nat Commun*, vol. 11, no. 1, p. 97, Jan 7 2020, doi: 10.1038/s41467-019-13814-x.
- [5] C.-Z. Chang *et al.*, "Experimental Observation of the Quantum Anomalous Hall Effect in a Magnetic Topological Insulator," *Science*, vol. 340, no. 6129, pp. 167-170, 2013, doi: doi:10.1126/science.1234414.
- [6] J. Wang, B. Lian, and S.-C. Zhang, "Quantum anomalous Hall effect in magnetic topological insulators," *Physica Scripta*, vol. T164, p. 014003, 2015/08/25 2015, doi: 10.1088/0031-8949/2015/t164/014003.
- [7] S. Wu *et al.*, "Observation of the quantum spin Hall effect up to 100 kelvin in a monolayer crystal," *Science*, vol. 359, no. 6371, pp. 76-79, 2018.
- [8] S.-Y. Xu *et al.*, "Discovery of a Weyl fermion semimetal and topological Fermi arcs," *Science*, vol. 349, no. 6248, pp. 613-617, 2015, doi: doi:10.1126/science.aaa9297.
- [9] L. He Qing *et al.*, "Chiral Majorana fermion modes in a quantum anomalous Hall insulator–superconductor structure," *Science*, vol. 357, no. 6348, pp. 294-299, 2017/07/21 2017, doi: 10.1126/science.aag2792.
- [10] D. Takane *et al.*, "Observation of chiral fermions with a large topological charge and associated Fermi-arc surface states in CoSi," *Phys Rev Lett*, vol. 122, no. 7, p. 076402, 2019.
- [11] R. Li, J. Wang, X.-L. Qi, and S.-C. Zhang, "Dynamical axion field in topological magnetic insulators," *Nature Physics*, vol. 6, no. 4, pp. 284-288, 2010/04/01 2010, doi: 10.1038/nphys1534.
- [12] C. Liu *et al.*, "Robust axion insulator and Chern insulator phases in a two-dimensional antiferromagnetic topological insulator," *Nature materials*, vol. 19, no. 5, pp. 522-527, 2020.
- [13] V. Dziom *et al.*, "Observation of the universal magnetoelectric effect in a 3D topological insulator," *Nature communications*, vol. 8, no. 1, pp. 1-8, 2017.
- [14] D. Zhang, M. Shi, T. Zhu, D. Xing, H. Zhang, and J. Wang, "Topological axion states in the magnetic insulator MnBi₂Te₄ with the quantized magnetoelectric effect," *Phys Rev Lett*, vol. 122, no. 20, p. 206401, 2019.
- [15] M. Jamali *et al.*, "Giant spin pumping and inverse spin Hall effect in the presence of surface and bulk spin–orbit coupling of topological insulator Bi₂Se₃," *Nano letters*, vol. 15, no. 10, pp. 7126-7132, 2015.
- [16] Y. Fan *et al.*, "Magnetization switching through giant spin–orbit torque in a magnetically doped topological insulator heterostructure," *Nature materials*, vol. 13, no. 7, pp. 699-704, 2014.

- [17] H. Wang *et al.*, "Surface-State-Dominated Spin-Charge Current Conversion in Topological-Insulator-Ferromagnetic-Insulator Heterostructures," *Phys Rev Lett*, vol. 117, no. 7, p. 076601, Aug 12 2016, doi: 10.1103/PhysRevLett.117.076601.
- [18] M. Safdar, Q. Wang, M. Mirza, Z. Wang, K. Xu, and J. He, "Topological surface transport properties of single-crystalline SnTe nanowire," *Nano letters*, vol. 13, no. 11, pp. 5344-5349, 2013.
- [19] J. Tian, I. Childres, H. Cao, T. Shen, I. Miotkowski, and Y. P. Chen, "Topological insulator based spin valve devices: Evidence for spin polarized transport of spin-momentum-locked topological surface states," *Solid State Communications*, vol. 191, pp. 1-5, 2014.
- [20] Z. Jiang *et al.*, "Enhanced spin Seebeck effect signal due to spin-momentum locked topological surface states," *Nature communications*, vol. 7, no. 1, pp. 1-7, 2016.
- [21] J. F. Sierra, J. Fabian, R. K. Kawakami, S. Roche, and S. O. Valenzuela, "Van der Waals heterostructures for spintronics and opto-spintronics," *Nature Nanotechnology*, vol. 16, no. 8, pp. 856-868, 2021.
- [22] A. A. Baker, A. I. Figueroa, L. J. Collins-McIntyre, G. van der Laan, and T. Hesjedal, "Spin pumping in Ferromagnet-Topological Insulator-Ferromagnet Heterostructures," *Scientific Reports*, vol. 5, no. 1, p. 7907, 2015/01/20 2015, doi: 10.1038/srep07907.
- [23] J. Li *et al.*, "Intrinsic magnetic topological insulators in van der Waals layered MnBi₂Te₄-family materials," *Science Advances*, vol. 5, no. 6, p. eaaw5685, 2019.
- [24] I. I. Klimovskikh *et al.*, "Tunable 3D/2D magnetism in the (MnBi₂Te₄)(Bi₂Te₃)_n topological insulators family," *npj Quantum Materials*, vol. 5, no. 1, pp. 1-9, 2020.
- [25] H. Wang *et al.*, "Above room-temperature ferromagnetism in wafer-scale two-dimensional van der Waals Fe₃GeTe₂ tailored by a topological insulator," *ACS nano*, vol. 14, no. 8, pp. 10045-10053, 2020.
- [26] L. Ding, C. Hu, F. Ye, E. Feng, N. Ni, and H. Cao, "Crystal and magnetic structures of magnetic topological insulators MnBi₂Te₄ and MnBi₄Te₇," *Physical Review B*, vol. 101, no. 2, p. 020412, 2020.
- [27] J. Q. Yan *et al.*, "A-type antiferromagnetic order in MnBi₄Te₇ and MnBi₆Te₁₀ single crystals," *Physical Review Materials*, vol. 4, no. 5, p. 054202, 05/14/ 2020, doi: 10.1103/PhysRevMaterials.4.054202.
- [28] M. S. Cao *et al.*, "Electromagnetic response and energy conversion for functions and devices in low-dimensional materials," *Advanced Functional Materials*, vol. 29, no. 25, p. 1807398, 2019.
- [29] C. Smith, "Low-dimensional quantum devices," *Reports on Progress in Physics*, vol. 59, no. 2, p. 235, 1996.
- [30] M. C. Wang *et al.*, "Prospects and opportunities of 2D van der Waals magnetic systems," *Annalen der Physik*, vol. 532, no. 5, p. 1900452, 2020.
- [31] A. Alfonsov, K. Mehlawat, A. Zeugner, A. Isaeva, B. Büchner, and V. Kataev, "Magnetic-field tuning of the spin dynamics in the magnetic topological insulators MnBi₂Te₄(Bi₂Te₃)_n," *Physical Review B*, vol. 104, no. 19, p. 195139, 11/22/ 2021, doi: 10.1103/PhysRevB.104.195139.
- [32] A. Alfonsov *et al.*, "Strongly anisotropic spin dynamics in magnetic topological insulators," *Physical Review B*, vol. 103, no. 18, 2021, doi: 10.1103/PhysRevB.103.L180403.

- [33] R. C. Vidal *et al.*, "Topological Electronic Structure and Intrinsic Magnetization in MnBi₄Te₇: A Bi₂Te₃ Derivative with a Periodic Mn Sublattice," *Physical Review X*, vol. 9, no. 4, 2019, doi: 10.1103/PhysRevX.9.041065.
- [34] G. Xiao, C. Zhu, Y. Ma, B. Liu, G. Zou, and B. Zou, "Unexpected Room-Temperature Ferromagnetism in Nanostructured Bi₂Te₃," *Angewandte Chemie International Edition*, vol. 53, no. 3, pp. 729-733, 2014, doi: <https://doi.org/10.1002/anie.201309416>.

CHAPTER 4: STABLE UNIVERSAL 1- AND 2-INPUT SINGLE-MOLECULE LOGIC GATES

The work presented in this chapter is recently published in *Advanced Materials* [1].

4.1 Introduction

Effective control of electronic properties of molecular junctions for stable rectification [2, 3], switching [4, 5], memory [6, 7] and logic operation [8-13] is critical for reducing the area and power consumption of electrical circuits. Important advances have been made in the design of multifunctional molecular devices that employ external stimuli (*e.g.*, chemical, light, magnetic or electric field) to modulate electron transport through molecular junctions [3, 4, 6, 10, 11, 14-20]. The modulations typically rely on stimulus-induced changes in molecular electronic states [6, 17, 21] and therefore the functional diversity and signal stability of molecular devices depend on the availability of different stable electronic states and efficient conversions between them [3, 4, 11, 22]. As all-electrical-driven devices, three-terminal solid-state single-electron transistors (SETs) [15, 19, 23-29] not only reflect the quantum behavior of intramolecular electron transport, such as Coulomb blockade [16, 18, 30, 31], Zeeman effect [18, 20], thermoelectric properties [26, 27] and Kondo effect [20, 32-34], but also have the unique advantage of controlling the molecular orbitals (MOs) by applying external electrostatic potentials [15, 24, 34-37], thereby providing new opportunities for the ultra-miniaturization of computing elements [38-41]. However, there are still two key challenges in utilizing SETs in single-molecule functional devices. First, the background electrostatic potentials of molecular junctions that affect the absolute energy of MOs are difficult to control, and so the resonance regions determined by MOs are normally different for different junctions formed with the same molecule [16, 18, 30, 41]. Second, the multifunctional implementation requires clear boundaries between Coulomb blockade and resonance regimes [18, 25, 31], which are complicated by the electrode-induced energy-level broadening of MOs [15, 25, 29].

Targeting these two challenges, we screened Au/S-(CH₂)₃-Fc-(CH₂)₉-S/Au (Fc=ferrocene) SETs from five different kinds of Fc-based gated SET junctions and designed a prototype Single-Electron Logic Calculator (SELC). First, instead of relying on absolute currents affected by the uncertainty of background electrostatic potentials, we employ current conversions between two sturdy and well-defined resonance regimes rendered by two adjacent conductive MOs of Fc. The MOs have a stable, small energy separation of around 100 meV and sit close to the Fermi energy of the electrodes in all five different Fc-based SETs and our DFT calculations show that this energy signature is not dependent on the conformation of the molecule inside the transistor [23, 27, 42, 43]. Crucially, our measurements and calculations show that the current conversions due to the modulation of MOs by gate (V_g) and bias (V_b) voltages are stable. Second, we used n-alkyl $-(\text{CH}_2)_n-$, $n \geq 3$) linkers to weaken the coupling between the molecule and the electrodes, *i.e.*, to minimize the broadening of the MO energy levels [27] on the Fc moiety by effectively isolating Fc from the electrodes [19, 44, 45]. Hence, we obtained a sharp-edged diamond-shaped Coulomb blockade regime in Au/S-(CH₂)₃-Fc-(CH₂)₉-S/Au SETs that allows the generation of clear current switching signals. The small energy separation of the two adjacent conductive MOs of Fc supports logic operations at low input voltages ($|V_b| \leq 80$ mV, $|V_g| \leq 2$ V) far below the 1.5-5 V drive voltage and 3-15 V gate voltage of CMOS (Complementary Metal Oxide Semiconductor). By implementing all universal logic gates (the four 1-input gates YES, NOT, PASS_1, and PASS_0 and the seven 2-input gates AND, XOR, OR, NAND, NOR, INT, and XNOR), we demonstrate reliable programmable logic operations based on one single-molecule SET.

4.2 The SELC sample preparation

To prepare the ferrocene-based (Fc-based) SELCs, it is important to obtain a well fabricated chip deposited with nanoelectrodes and back-gate. In the fabrication process, a 1-10ohm-cm 380 μm Silicon N/Phosphorous wafer was used. Fig. 4.1 shows the chip images scanned by scanning electron microscope (SEM) at different fabrication stages. The first two layers are the layers for conducting leads, shown as A. The third layer is the layer for back-gate electrode, shown as B. These three layers were patterned via photolithography. The first layer was deposited with 5 nm/10 nm Ti/Pd (shown as the dark grey small step)

on the 1.0 μm oxide Si/SiO₂ wafer surface (shown as the grey flat background). The second layer was deposited on top of the first layer with 15 nm/70 nm Ti/Pd (shown as the light grey pattern). The third layer was deposited in the center between the left and right leads with 35 nm Al₂O₃/Al (the thickness of the Al₂O₃ on the surface of Al is about 1nm). The thin insulating layer isolates the gate from the nanoelectrodes (the fourth and fifth layers) and molecules. In Fig. 4.1(C) and (D), the 15 nm thin Au nanowire (fourth layer) and the 60 nm thick Au nano pads (fifth layer) were patterned via ebeam-lithography and deposited, respectively. Figure 4.1(D) is the zoom-in picture of the center of (C). It shows the bow-tie shaped nanowire on top of the Al₂O₃/Al back-gate between two bright grey nano-pads. The constricted part of the nanowire (the center of the bow-tie) is 50 nm wide [27]. In the fabrication process, a Reactive Ion Etcher (RIE) is used at each step to remove the residual chemicals on the surface of the chip through oxygen plasma.

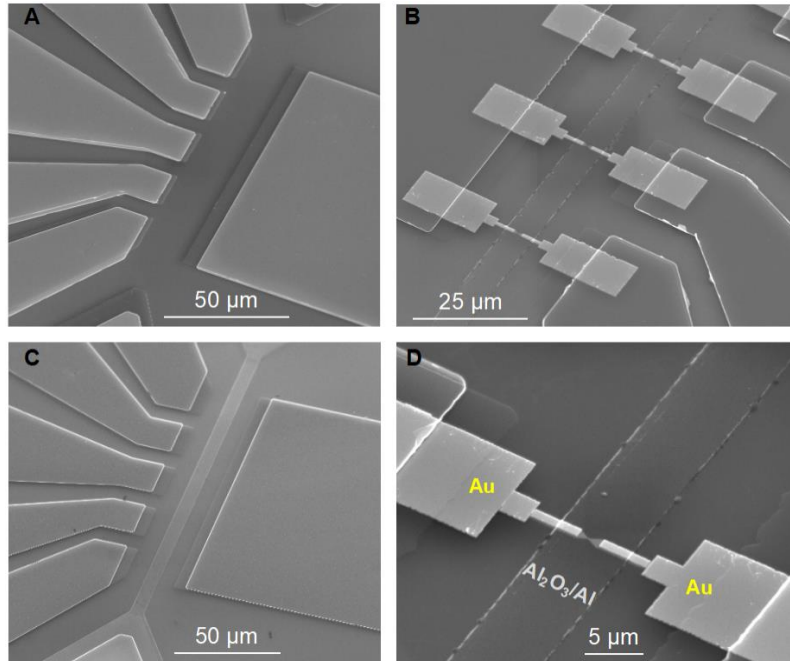


Figure 4.1: The SEM images for chip at different stages. (A) The pattern of the first two layers (the conducting-leads layers). (B) The third layer (Al₂O₃/Al back-gate electrode) is deposited between the patterns formed by the first two layers. (C) The fourth and fifth layers (Au nanowires and Au nano-pads) are deposited on top of the first three layers. (D) The zoom-in picture shows the nanowire has been deposited on the back-gate electrode. The constricted part of the nanowire is 50 nm wide and 15 nm thick.

The molecule solution was dissolved in ethanol for the preparation of SELCs. The 0.01 mM molecular solution was mixed with 1 ml ethanol, stirring until it was completely mixed. 15 μ l of the solution was then diluted with 1.5 ml ethanol to fully dissolve it and the solution was left at room temperature for one day. After the chip had been completely fabricated, the clean chip was immersed into the diluted molecular solution for about 30 to 40 minutes, so that the molecules were firmly adsorbed on the surface of the gold nanowires through the thiolate anchoring groups. We then gently washed the chip several times with the molecular solution and then soaked it in pure ethanol for 3 to 5 minutes. The chip was then blown dry with N_2 to remove the excess molecular solution before being mounted on the chip holder in the home-made probing box.

We use a current feedback-controlled electromigration method to gradually induce Au atom migration from the central region of the bow tie, thereby narrowing the nanowire [27, 46]. Fig. 4.2 shows the I-V curves of the electromigration process of four samples. These samples clearly show molecular transmission characteristics in the measured Current Map after the nanowires are broken. The blue curve in the figure shows the nanowire narrowing process at room temperature. Once the current flowed through the nanowire, the feedback program would not stop until the resistance of the nanowire exceeded 13 $K\Omega$ (corresponding to $1G_0$). This resistance indicates a universal single-channel Au-Au connection has been formed in the nanowire [47].

After the nanowire had been narrowed, the chip was transferred immediately into a Helium-3 cryostat and dipped into liquid helium filled magnet Dewar to cool down. The low temperature can effectively reduce the further uncontrolled breaking of the nanowire caused by the vibration of atoms and the surface tension. Then, further electromigration was used at low temperature to break the $1G_0$ connection (the single Au-Au atom contact) to form the molecular junction. The red curves in Fig. 4.2 show the further electromigration process of the nanowires at 4 K. The insert plots of Resistance vs Bias Voltage indicate that, before the final breaking, the resistances of the nanowires were steadily around 13 $K\Omega$. As the bias voltage increased to 1.5 ~ 2.3 V, the nanowires met their final breaking points [47]. Once the resistance

suddenly increased by more than 10 times, the current was stopped immediately. Then the low-temperature nanowire rupture was completed.

After the breaking of the gold nanowire, the molecule previously absorbed on the surface bridged the gap to form a molecular junction. The high threshold voltage of the low-temperature nanowire rupture leads to a temporary high reducibility of the gold surface in the ruptured area, which promotes the formation of Au-S bonds between the molecular terminal groups and the gold nanoelectrodes [48], and so further strengthening the molecular junction[49]. After the molecular junction was formed, the immediate current dropping can prevent the molecule from being damaged due to high bias voltage. In our measurements, there were 231 nanowires showing proper current feedback-controlled electromigration curves out of 320 from 8 chips. 214 of the 231 showed 10 to 100 K Ω resistance after the room temperature electromigration process. Of these, 37 showed electromigration curves like those in Fig. 4.2, with the $1G_0$ point before low-temperature splitting and 1~100 M Ω resistance at near-zero bias after splitting, which is different from a simple tunnel junction. To minimize the probability of several molecules bridging one nanogap, we controlled the coverage of molecules on an array of gold electrodes such that <20% of the junctions (*i.e.*, 37 in an array of 214 broken junctions) showed the resistance of molecules. Of these 37, a total of 9 nanowires showed the stable and well-defined resonant current regions that vary linearly with V_g over -100 to 100 meV bias voltage range and -3 to 3 V gate voltage range. From these statistics we conclude that the low yield of devices with the desired signal characteristics is mainly due to the uncertainty of the gap size created by the electromigration method [50], the low coverage of the molecules, and the very specific, narrow effective range of the gate voltage. However, the molecular junctions can be easily pre-screened for the desired properties, as we found that those nanojunctions with electromigration curves like Fig. 4.2 are likely to exhibit a molecular Coulomb blocking pattern. In future work, further optimization of the electromigration process and gate fabrication will improve the controllability of nanoelectrode creation and molecular electronic states for large-scale production of stable SELCs based on this first prototype.

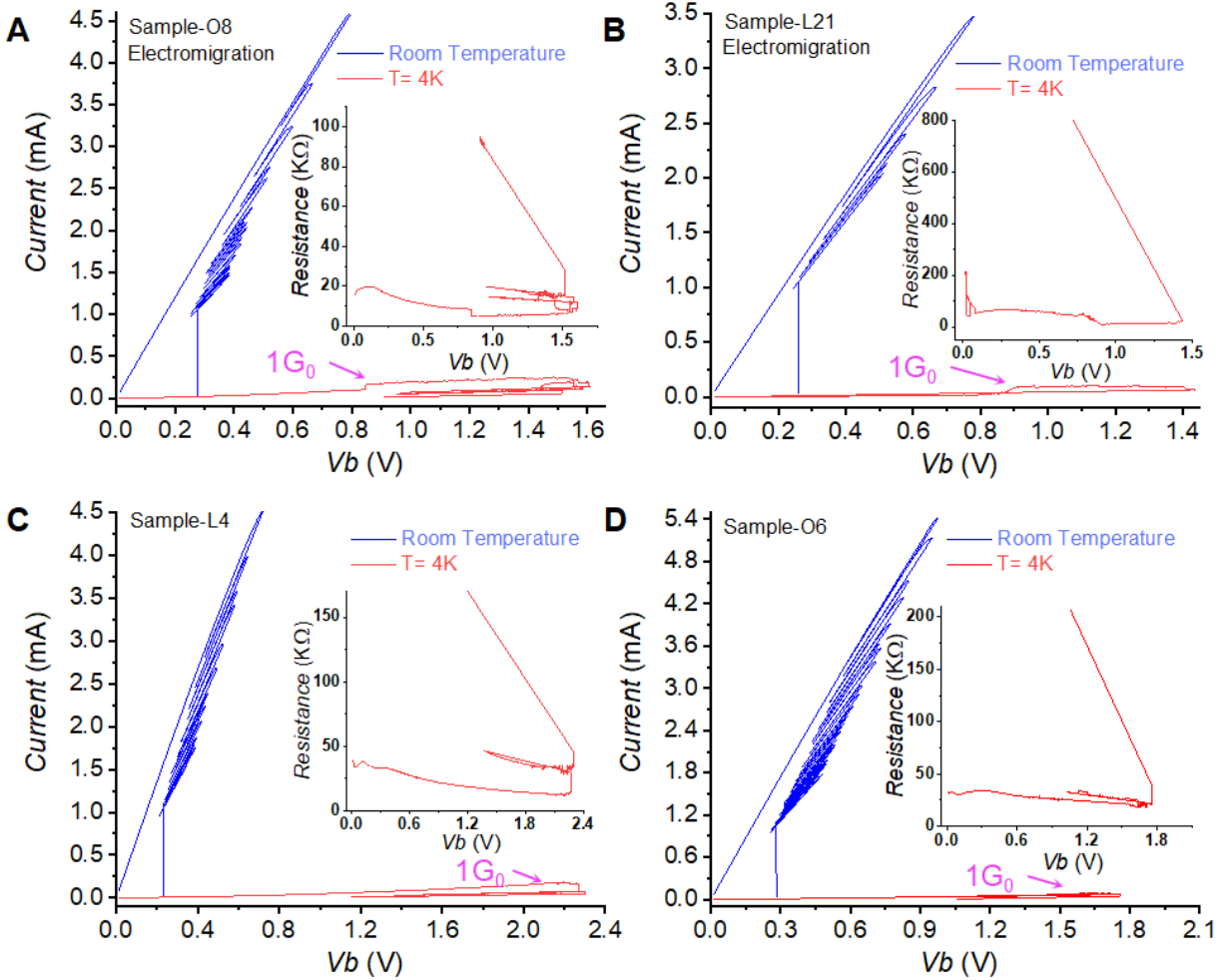


Figure 4.2: The current feedback-controlled electromigration I-V curves of four nanowires that show the molecular conductance signal after breaking. (A) The blue curve is the electromigration curve of the nanowire at room temperature and pressure. The red curve is the electromigration curve at 4 K. For the whole electromigration processes, the starting resistance was 155Ω , the middle state resistance was $13 K\Omega$, and the final breaking resistance was $\sim 1 M\Omega$. The inset is the corresponding resistance of the low temperature electromigration process. (B) The electromigration processes in a second successful experiment. The resistance starts with 200Ω and ends with $\sim 4 M\Omega$. (C) The electromigration processes in a third successful experiment. The resistance starts with 150Ω and ends with $\sim 2 M\Omega$. (D) The electromigration processes in a fourth successful experiment. The resistance starts with 182Ω and ends with $\sim 3 M\Omega$. Five additional working SELC nanowire prototypes were found, giving a total yield of 9 from the total of 37 devices with these characteristic electromigration curves.

4.3 The SELC Design

Figure 4.3 (A) and (B) show the schematic configuration and circuit design of the three-terminal SELC comprising the functional $Au/S-(CH_2)_3-Fc-(CH_2)_9-S/Au$ molecular junction, strung over an Al back-

gate (third terminal) with Al_2O_3 as the insulating layer between the junction and the gate. Along the junction, the Fc moiety is electronically isolated by the $-(\text{CH}_2)_3-$ and $-(\text{CH}_2)_9-$ linkers on either side and the molecule is connected to the source and drain nano-electrodes by thiolate–metal bonds. Studies of similar Fc-based molecules in three-terminal SETs [23, 27] and SAM-based junctions [44, 51, 52] have shown that asymmetric $-(\text{CH}_2)_n-$ linkers cause unequal coupling between the molecule and the electrodes, leading to current rectification [44] and thus providing a natural route to encode information *via* orthogonal modulations of the MOs by V_g and V_b . To minimize the probability of several molecules bridging one nanogap, we created low coverage of molecules on an array of gold electrodes [20], as explained in the sample preparation section. In the experiment, after electromigration, 37 of the 214 correctly broken nanowires showed a molecular signal (current of nA scale, shown in Fig. 4.2) different from a bare tunneling. That is, less than 20% of the nanogaps could be covered by molecules, which indicates the low possibility of multiple molecules binding in the same nanogap at the same time.

Figure 4.3 (C) and (D) show representative I - V_g and I - V_b curves measured from the three-terminal junction at different values of V_b and V_g , respectively. The distinct current bi-plateau feature and the linear variation of the switch points and widths of the plateaus with V_g and V_b indicate that the molecular junction has been formed and the current through it can be effectively controlled by V_g and V_b .

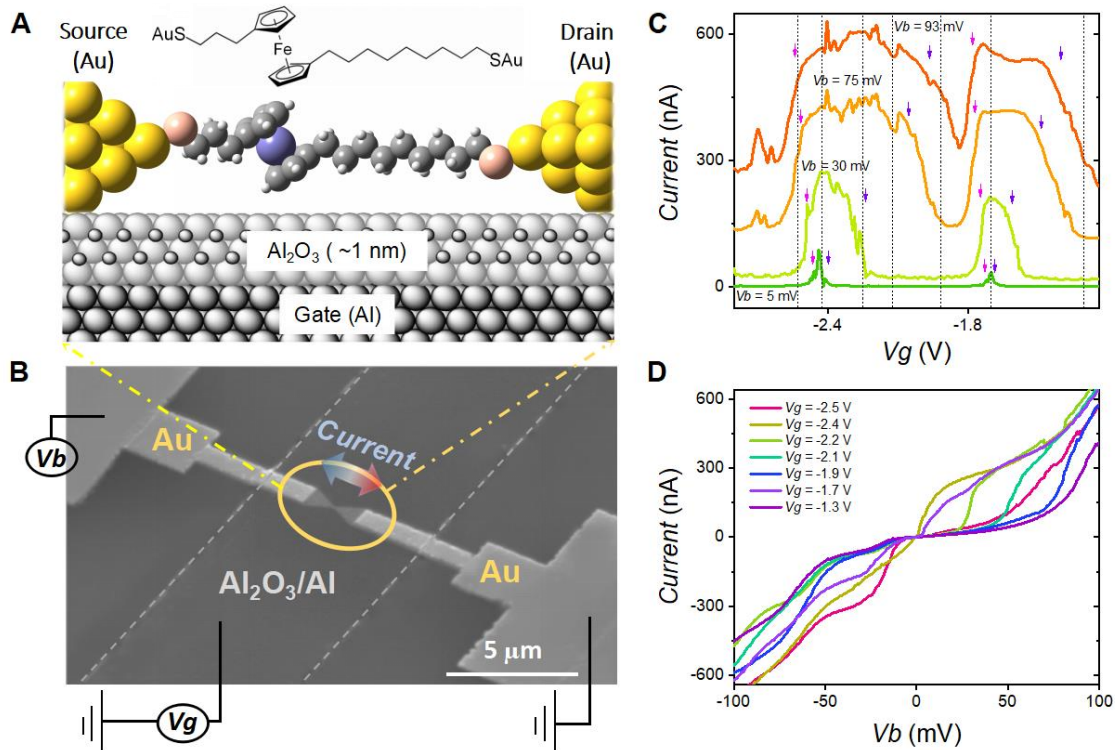


Figure 4.3: The design of SELC. (A) Chemical structure and schematic of a $S-(CH_2)_3-Fc-(CH_2)_9-S$ molecule bridging the nanogap between two nano-electrodes. (B) SEM image of a SELC showing the Au nanowire on the Al_2O_3/Al back-gate on a Si wafer and positions where V_b and V_g are applied. The nanowire and the back-gate were patterned by electron-beam and optical lithography, respectively [53]. The molecular junction formed in the center of the nanowire was produced using current feedback-controlled electromigration [15, 27, 46]. (C) Representative $I-V_g$ curves for different values of V_b measured at 225 mK with 231 points per curve. The arrows mark the switch points of the current plateaus. The dashed lines indicate the V_g values corresponding to the seven $I-V_b$ curves in (D). (D) Representative $I-V_b$ curves for the seven different V_g values, with 231 points per curve. $T = 225$ mK.

4.4 Results and Discussion

4.4.1 Current map measurements and calculations

The color-map of the measured current through the SELC as a function of V_b and V_g is shown in Fig. 4.4 (B). The color code divides the map into different transmission regimes. The red and blue colors respectively indicate the positive and negative currents in the resonance regime, where the energy levels of the conductive MOs (ϵ_1 : HOMO-1 and ϵ_2 : HOMO-2, described in detail in reference [1], SI-S3 (2)) lie

within the bias window, are well-separated, and are conductive due to their coupling to both electrodes (in contrast to ϵ_0 : HOMO, where the long-alkyl chain isolates the Fc-centered level from one electrode). In the map, ϵ_1 and ϵ_2 indicate their resonance regions. One distinct characteristic, which is shared by all five different kinds of Fc-based gated SETs, is evident in Fig. 4.4, showing that ϵ_1 and ϵ_2 overlap at around ± 100 meV. The left (r') and right (r'') dashed lines indicate the edges of the ϵ_1 resonance region. Clear transitions between the resonance regime and the Coulomb blockade regime (white diamond-shaped areas) are shown in the corresponding differential conductance (dI/dV) map of Fig. 4.4 (D). '1', '3' and '5' indicate the Coulomb blockade regions under different gate voltages near zero-bias. They correspond directly to the energy diagram in Fig. 4.4 (A), with both MO levels above/below the Fermi energy for region '1'/'5', respectively, and with the electrostatic potential of the leads sandwiched between the two MO levels for region '3', *i.e.*, the bias window sits within the energy gap between the two MOs. This creates the diamond-shaped Coulomb blockade region trapped within a ~ 100 mV bias voltage range which corresponds to the energy difference between the two MOs ($\Delta MOs = \epsilon_1 - \epsilon_2$), as marked by the crossing of the ϵ_1 and ϵ_2 resonance boundaries. The computed electron transmission spectrum (Ts) overlaid in Fig. 4.4 (A) (state '5') is the zero-bias Ts of the molecular junction calculated by DFT-NEGF method (described in details in reference [1], SI-S3 (2)). The energy difference between the two Ts peaks describes the calculated ΔMOs , which is about 110 meV in good agreement with the measurements and is robust even for different conformations of the molecule and different electrode distances in the SET (see reference [1], SI-Figure S5 and Figure S6 for details). The narrow widths of the peaks represent the small broadenings of the MOs, ensuring small currents in the Coulomb blockade region. Due to the asymmetry of the $-(CH_2)_9-$ and $-(CH_2)_3-$ linkers, the molecule–electrode couplings under positive and negative biases are different, resulting in different extensions of the Ts peaks. Consequently, the background (blockade) current under negative bias voltage is higher than at positive bias (as seen in Fig. 4.4 (B and C), corresponding to the measured and calculated current maps, respectively). In addition, no Kondo effect was observed in the experiment and the molecule is in the ground state ($S = 0$), described later in section 4.4.11. DFT calculations show the spin degeneracy of the ground state molecule in the absence of magnetic field. The experiments reported in this

work were conducted at 225 mK. In our previous work [27], where similar molecules were studied, well-defined conductance excitations within the Coulomb blockade regime can persist up to 120 K, suggesting that the operations reported in the present work can be feasible at much higher temperatures.

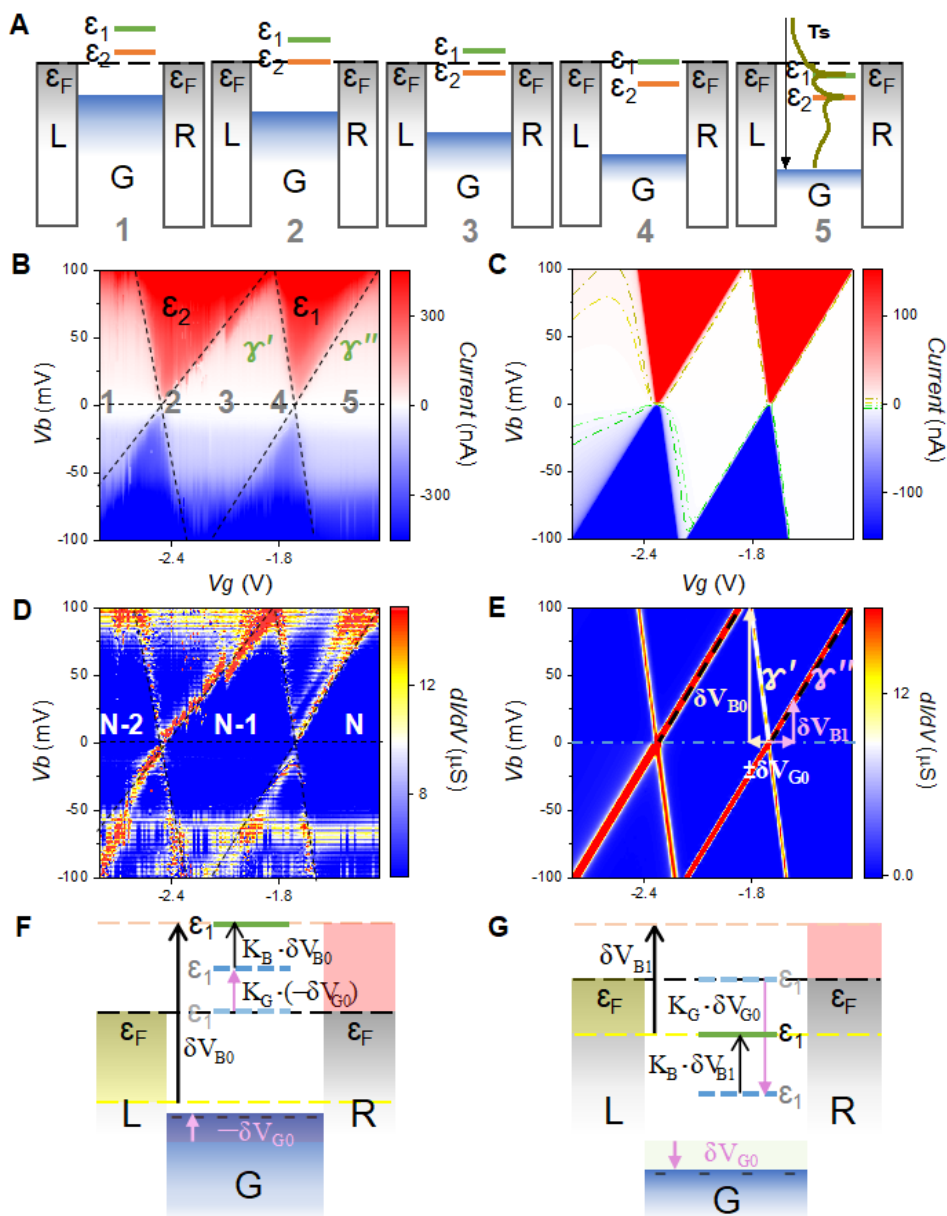


Figure 4.4: The current modulation of SELC.

(A) Schematic diagrams of the shift of MOs manipulated by the gate voltage at zero-bias. The T_s of state '5' indicates that the conductive MOs (ϵ_1 : HOMO-1, ϵ_2 : HOMO-2) are below the Fermi energy when V_g is close to zero. At charge points '2' and '4', ϵ_1 and ϵ_2 are respectively aligned with the Fermi level of the

electrodes. **(B)** Measured current map at 225 mK with V_b : 231 \times V_g : 231 points. The red/blue colors indicate positive/negative resonance currents, respectively. The numbers correspond to the diagrams in (A). ϵ_1 and ϵ_2 resonance regions correspond to the MOs. **(C)** Calculated current map with V_b : 101 \times V_g : 142 points (V_b : 2 mV per step; V_g : 11 mV per step). The background pattern (marked by the dashed contour lines) is contributed by the extension of transmission peaks. **(D)** Measured differential conductance map highlighting the edges between resonance and Coulomb blockade regimes. ‘N-2’, ‘N-1’ and ‘N’ indicate the number of fully occupied MOs. **(E)** The calculated differential conductance map. $-\delta VG_0$ and $+\delta VG_0$ indicate charging and discharging of the Gate. δVB_0 and δVB_1 indicate the increase of V_b from 0 V to r' and r'' edges, respectively. **(F and G)** schematically show how the energy of ϵ_1 MO modulated by V_b and V_g aligns with the Right and Left electrode Fermi levels. The light blue dashed line indicates the initial energy of ϵ_1 . The dark blue dashed line indicates the energy of ϵ_1 when V_g changes ((F) $-\delta VG_0$ or (G) $+\delta VG_0$). The green line indicates the final energy of ϵ_1 after adding the change of V_b (δVB_0 or δVB_1). K_B and K_G are the energy change rates.

Due to the monotonic evolution of the energy eigenvalues of MOs under bias and gate voltages [15, 37], we developed a theoretical model to describe the energy change rates (K_B and K_G) of MOs, which are directly related to the molecular dipole moments along the directions of voltages described in detail in SI-S3 (1) in reference [1]. Thus, K_B and K_G can be calculated by the shift rates of Ts under bias and gate voltages, respectively (see SI-S3 (3) of reference [1]) [37, 54]. However, K_B , K_G and the MO energy shift (*MOs Shift*) are directly related to the configuration and background electrostatic potential of the molecular junction. Thus, to understand the junction configuration in the experiment, we calculated 12 different configurations for the 3-terminal molecular junction of the same molecule (see reference [1], SI-S3 (4)) and analyzed their corresponding K_B , K_G , ΔMOs and *MOs Shift* values as described in detail in reference [1], SI-S3 (5) Table S1. The data show that ΔMOs remains near constant (~ 110 meV) for the different configurations, in line with the experimental observations and proving that the Coulomb region lies stably within a well-defined and easily accessed bias voltage range, described in detail in reference [1], SI-S4, despite the potentially shifted current maps for different junction configurations. Indeed, the experimental K_B and K_G can be extracted from the slopes of r' and r'' edges for both MO resonance regions [15] as (described in detail in reference [1], SI-S3 (5)): $K_B = (r' + r'')/2(r' - r'')$, $K_G = -r'r''/(r' - r'')$. Figure 2F and

G illustrate the combined modulation of the shifts of ε_1 energy level in terms of the energy change rates K_B and K_G .

The corresponding DFT-NEGF calculated current and differential conductance (dI/dV) maps of the junction, given in detail in SI-S3 (6) of reference [1], are shown in Fig. 4.4 (C and E), respectively. The Ts not only reproduces the asymmetric background of Coulomb blockade regions under bias reversal, but also resolves the different widths of the r' and r'' edges (see Fig. 4.4 E and D), which can be understood by the directional shift of the Ts towards the bias window controlled by the gate voltage (note the asymmetric Ts peaks in Fig. 4.4 (A)-5, discussed in SI-S3 (6)) of reference [1]. Since the K_B and K_G values correspond directly to the electronic structure of the conductive MOs, they reflect the dipole moments of each MO. The similarity between the experiment and theoretical calculations on the parallel evolution of the two MOs along the gate-bias voltage (see reference [1], Figure S6) is a good indication of the presence of a single molecule in the junction. Two independent molecules, for example, would present very different slopes due to substantial differences of the coupling to the electrodes at the microscopic level [30]. Thus, the agreement between the theoretical calculations and experimental measurements (data for different Fc-based SETs are shown in SI-S8) strongly demonstrates that the electrostatic modulation of the two conductive MOs of the Fc moiety provides a two-state Coulomb blockade region at $V_b=1\sim 100$ mV. The differences between the theoretical current map (Fig. 4.4 (C)) and the measured results (Fig. 4.4 (B)) are due to the effect of the gate voltage field on the molecular configuration, the leaking currents from the source/drain to the gate electrode, and the inelastic electron tunneling (IET) current of the molecule, which are all effects not considered in the calculations. As discussed in SI-S7 of reference [1], Fig. 4.4 (B) shows the current shift in the high gate voltage region ($|V_g| > 2.2$ V), which is caused by a small change in the molecular configuration under high gate electrostatic field. Furthermore, the current in the Coulomb blockade region of Fig. 4.4 (B) is > 0.1 nA resulting from leakage through the gate (described later in leaking current section), while the blockade current in the theoretical case can be $< 10^{-3}$ nA. Finally, the measured IET spectra and corresponding

vibrational modes shown in SI-S9 of reference [1] also provide strong evidence that an individual molecule is responsible for the transport behavior.

4.4.2 Working principle of the resettable SELC

Using the two-state diamond-shaped Coulomb blockade feature provided by the two MOs, we establish SELC by using the current as Output signal, and the gate (Input1: V_g) and the bias (Input2: V_b) voltages as two orthogonal Input signals. Figure 4.5 summarizes the working principle of our SELC. Fig. 4.5(A) shows the detailed current map. Four input ranges of V_g and three of V_b are determined based on the current oscillation signal (described in next topic) across the Coulomb diamond region, labelled A (-1.82 V '0' to -2.02 V '1'), A' (-1.67 V '0' to -1.82 V '1'), A'' (-1.77 V '0' to -1.82 V '1'), AA' (-1.67 V '0' to -2.02 V '1') and B (70 mV '0' to 80 mV '1'), B' (30 mV '0' to 70 mV '1'), BB' (30 mV '0' to 80 mV '1'). The (1, 1) input represents the V_g and V_b both at high states in their own ranges, which is opposite to the (0, 0) input, for instance. Correspondingly the (1, 0) input means that the V_g is at high state while the V_b is at low state, opposite to the (0, 1) input. The current (Output) is represented by the color code in the map, red indicating high current state (>300 nA, 'on', '1') and blue the low current state (<300 nA, 'off', '0'). The white rectangles indicate logic operation areas, defined by two orthogonal input ranges (*i.e.*, one V_g range and one V_b range). The horizontal/vertical black dashed arrows represent the operating ranges of the gate/bias voltage under a particular bias/gate voltage.

We take the 2-input logic operation along AA' and BB' as an example to introduce the working principle of the logic gates within a set operating area. Fig. 4.5(B) is the corresponding logic diagram in the differential conductance map. The arrows in the white rectangle illustrate how V_g and V_b are combined to govern the current switching across the edges of the resonance and Coulomb blockade regions. The black arrow indicates that the changes of V_g (along the short-green-left arrow of AA') and V_b (along the short-green-up arrow of BB') are in the same phase (0°). The corresponding multi-cycle logic input and output signals are shown in Fig. 4.5(E). As the input gate signal and input bias signal change in phase from (0, 0) to (1, 1), the signal of output current changes from '0' (off) to '1' (on). Thus, high V_g and high V_b inputs

(1,1) lead to high output current '1', while low V_g and low V_b inputs (0,0) lead to low output current '0'. However, when the change of V_g (along the short-green-left arrow of AA') and V_b (along the short-orange-down arrow of BB') are out of phase (180°), the logic operation changes (Fig. 4.5F). In this case, as V_g and V_b change from (0, 1) to (1, 0), output current changes from '1' (on) to '0' (off).

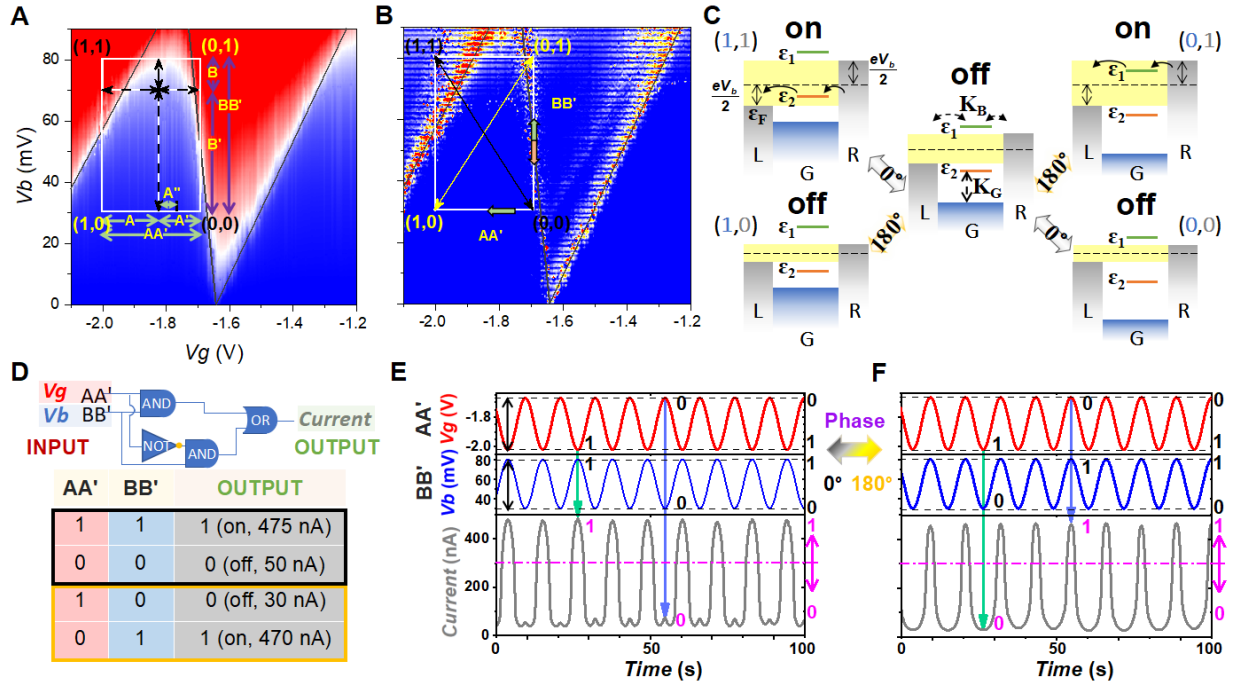


Figure 4.5: Logic calculation based on resonance excitations of MOs. (A) Measured 231×231 points current map at 225 mK marked with logic operating voltage-ranges. A, A', A'', AA' and B, B', BB' are the voltage-ranges of input-gate and input-bias, respectively. White rectangles mark 2-input logic operation areas. Input (1, 1) means high-gate and high-bias voltages, (0, 0) is the opposite case. Input (1, 0) means high-gate and low-bias voltages, (0, 1) is the opposite. (B) Differential conductance map corresponding to (A). Input AA'-BB' is an example to illustrate how gate (V_g) and bias (V_b) voltages are combined to achieve logic operations. The black arrow goes from (0, 0) to (1, 1), when V_g and V_b both change along the short green arrows. The yellow arrow goes from (0, 1) to (1, 0), when V_b and V_g change along the short orange and green arrows, respectively. (C) The schematic diagrams describe the energy level distributions of the four input cases in (B). Phase 0° and 180° correspond to the black and yellow arrow, respectively. (D) Equivalent logic circuit and truth table with AA'-BB' inputs at 0° and 180° phases. (E and F) show the curves of input V_g and V_b and measured output current at 0° and 180° , respectively.

Figure 4.5C schematically shows the energy distributions of MOs (ϵ_1 and ϵ_2) under the voltages indicated by black and yellow arrows in Fig. 4.5(B). The two orthogonal inputs switch the output current by shuttling the MOs in and out of the bias window. The central diagram corresponds to the intersection of

the arrows. The four diagrams on the corners correspond to the four terminals of the arrows (1,1), (0,0), (1,0) and (0,1). The top two diagrams show the resonance states, where ϵ_1 or ϵ_2 is in the bias window, generating high-current “on” states (>300 nA, output=1). The rest belong to the Coulomb blockade regime, with no MO in the bias window. They correspond to low-current “off” states (<300 nA, output=0). This logic operation is illustrated in the truth table in Fig. 4.5(D) and repeated for several cycles in Fig. 4.5(E), (F) to show the stability of SELC. Note that the signal remained stable throughout the whole experiment for about 2 months, even independent of the scan rate variation of the input signal, see Fig. 4.10. At least 37 cycles were taken for each curve, see Fig. 4.9; for illustrative purposes only 9 cycles (40 points per cycle) are shown in Fig. 4.5. The result of this logic operation can be interpreted as a complex logic gate array of one “INH” gate (inhibit) and one “AND” gate feeding their outputs into an “OR” gate. In this logic operation, SELC acts as a high-bias voltage indicator, *i.e.*, a high-bias input produces a high-current output, while a low-bias input produces a low-current output. The on/off ratio of high and low output currents is ~ 10 .

4.4.3 Determination of the gate voltage range for the 1-input logic gates

According to the robustness of the energy difference between the two conductive MOs, we found that the resonance regimes of the two MOs overlap at a certain gate voltage when the bias voltage reaches the energy difference (100 meV), and so enclose a diamond-shaped Coulomb blockade region. This diamond-shaped area provides addressable current signals for selecting voltage ranges to perform logic operations. Since the logic operations rely on clear switching signals, the selected gate voltage range needs to cross the boundaries of the Coulomb blockade area sandwiched between the two resonance regions to provide various current switching signals as the gate voltage changes. That is, the address of SELC’s operation gate voltage depends on the current conversion between the two resonance regimes under a certain bias voltage. We named this addressing process the relative addressing, as it does not depend on the absolute stability of the current under the gate and bias voltages. Thus, the relative addressing can be used to correct for the effect of MOs offset on SELC output at different background potentials, thereby improving the stability of SELC.

For the 1-input logic gates, the input signal is the gate voltage, and the output signal is the current. As shown in Fig. 4.6(A), initially, we set the gate voltage range from -2.02 V (high voltage state “1”) to -1.67 V (low voltage state “0”) under 70 mV bias voltage. In this range, the current value goes from high state “1” (~ 410 nA, “on”) to high state “1” (~ 410 nA, “on”), but the frequency of the output current is twice the frequency of the input voltage. It indicates that the gate voltage range spans the two boundaries of the Coulomb blockade area sandwiched between the two resonance regions. This frequency multiplier signal of current provides us with a basis for selecting the input gate voltage range that can realize multi-functional logic operations.

According to this signal, we keep the high-input gate voltage (“1”) around 2 V and adjust the value of the low-input gate voltage (“0”) from -1.67 V to -1.82 V to confirm the wideness of the boundary between the Coulomb blockade area and the ϵ_1 resonance region (see Fig. 4.7), and the minimum value of the low (“0” / “off”) state current under 70 mV bias in this voltage range (shown as the green arrows in Fig. 4.6(B) to (F)). We can see that as the gate voltage changes from -1.70 V (Fig. 4.6(B)) to -1.73 V (Fig. 4.6(D)), the current drops significantly from 400 nA to below 300 nA. While, if the gate voltage changes from -1.67 V (Fig. 4.6(A)) to -1.70 V (Fig. 4.6(B)), the current stabilizes at 420 \sim 400 nA (high state, “0”) with almost no change. Similarly, if the gate voltage changes from -1.79 V (Fig. 4.6(E)) to -1.82 V (Fig. 4.6(F)), the current stabilizes at ~ 120 nA (low state, “0”) with almost no change. This means that as the gate voltage (V_g) ranges from -1.67 V to -1.70 V the current through the molecular junction is stabilized in the ϵ_1 resonance region. For V_g from -1.70 V to -1.73 V the current is switching between the ϵ_1 resonance region and the Coulomb blockade area, and with V_g from -1.73 V to -1.82 V the current is settled in the Coulomb blockade region. In V_g range -1.67 V to -1.82 V, the maximum current value (~ 410 nA, “1” / “on” state) corresponds to the -1.67 V gate voltage (Fig. 4.6(A)), the minimum current value (~ 120 nA, “0” / “off” state) corresponds to the -1.82 V gate voltage (Fig. 4.6(F)), the current value of the boundary switching point is about 300 nA, $V_g \approx -1.72$ V. As the boundary between the ϵ_1 resonance region and the Coulomb blockade area is very sharp (the wideness of the V_g range is only 0.03V), we assumed that the current

switching between two Boolean states and named the current larger than 300 nA as “1” or “on” state, the current lower than 300 nA as “0” or “off” state. In this way, we determined the gate voltage range for the logic operation.

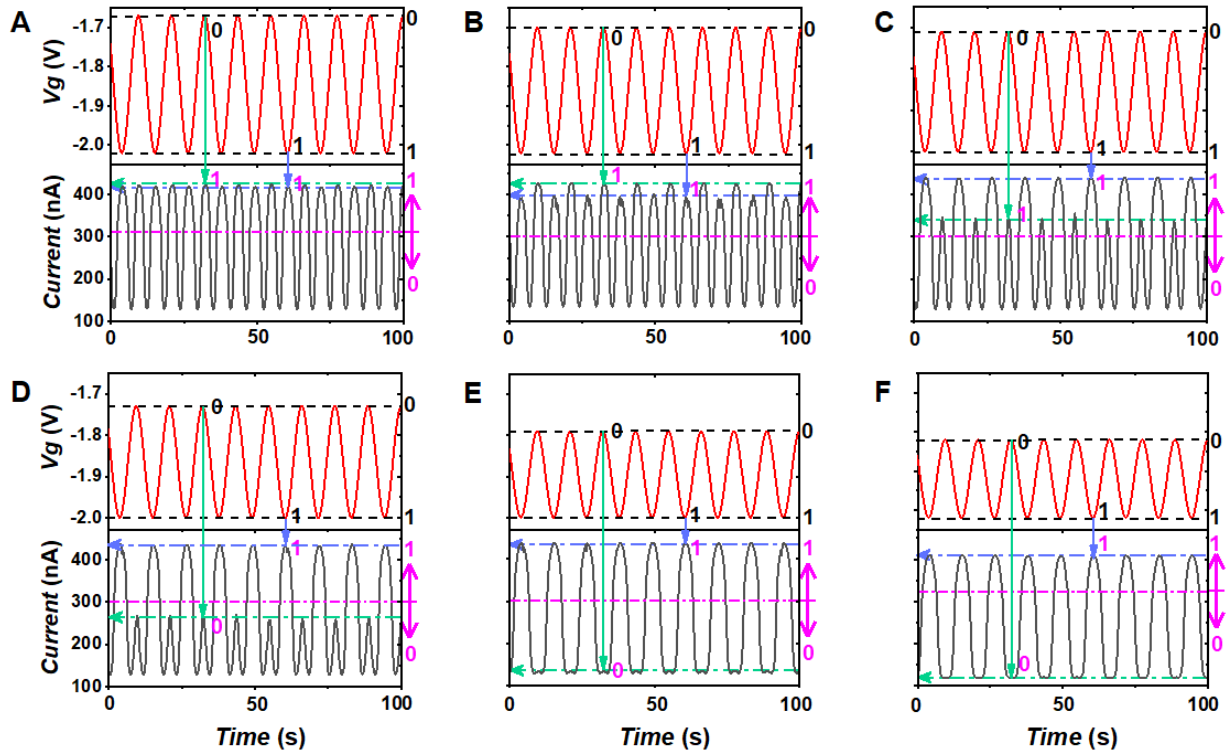


Figure 4.6: The test to determine gate voltage range for the operation of 1-Input logics at 70 mV bias voltage, 225 mK. In (A-F), the red curves are the input gate voltage signal, the high “1” gate voltages are about -2.0 V, the low “0” gate voltages are -1.67, -1.70, -1.71, -1.73, -1.79 and -1.82 V, respectively. The gray curves are the output current. The current values corresponding to the high gate voltages (“1”) are around 420 nA (“1”) marked by the blue arrows. While these marked by the green arrows are modulated by the low “0” gate voltages. The pink arrows on the left of each current curve indicate the Boolean “1” and “0” states of current, which is decided by whether the current value is higher than 300 nA.

4.4.4 SELC 1-input logic gates

For the 1-input logic gates, V_g is the only input, current is the output, and V_b is fixed at 70 mV.

Fig. 4.7(A) shows V_g ranges A and A’ for 1-input logic gates “YES” and “NOT”, respectively. Fig. 4.7(B), (C) show corresponding electronic symbols, truth tables and Input/Output signals. The 1-input “YES” logic

gate is based on current switching between the ϵ_2 resonance regime and the Coulomb blockade region. In this case, the high V_g ('1', -2.02 V) leads to resonance conductance of ϵ_2 MO, resulting in high current ('1', ~410 nA). The low V_g ('0', -1.82 V) reduces the energy of ϵ_2 MO and moves it out of the bias window, resulting in current blockade ('0', ~120 nA). Thus, high-input leads to high-output and low-input leads to low-output, “YES” logic. Conversely, for the 1-input “NOT” logic gate the operation is based on current switching between the Coulomb blockade region and the ϵ_1 resonance regime. In this case, at the high V_g ('1', -1.82 V) no MO lies in the bias window, so the current is in the blockade region ('0', ~120nA). The low V_g ('0', -1.67 V) further reduces the energy of MOs and shifts ϵ_1 into the bias window, so the current is in the resonance region ('1', ~410 nA). Thereby, high-input leads to low-output and low-input leads to high-output, “NOT” logic.

Figure 4.7(D) shows the V_g ranges AA' and A'' for 1-input logic gates “PASS 1” and “PASS 0”, respectively. According to the discussion above, the 1-input “PASS 1” logic gate involves current switching between ϵ_2 and ϵ_1 resonance regimes. Both high and low inputs led to high outputs, “PASS 1” logic. Since the switching process of the output current spans the entire Coulomb blockade region, the frequency of the output current signal is doubled compared with the input gate signal. This interesting feature can be used as a frequency multiplier. The current signal is also used as an address for the logic operations to define the Coulomb diamond region, which provides important information for calibrating the V_g ranges as described in section 4.4.3. By contrast, the 1-input “PASS 0” logic gate is based on the stability of the blockade current. In this case, at both high ('1', -1.82 V) and low ('0', -1.77 V) V_g , the two MOs are distributed on both sides of the bias window (as shown in Fig. 4.5(C)-‘off’), so the output current is in the Coulomb blockade region ('0', ~120 nA) contributed by the extension between the two transmission peaks of Ts (shown as Fig. 4.4(A) ‘5’). High-input and low-input both lead to low-outputs, “PASS 0” logic.

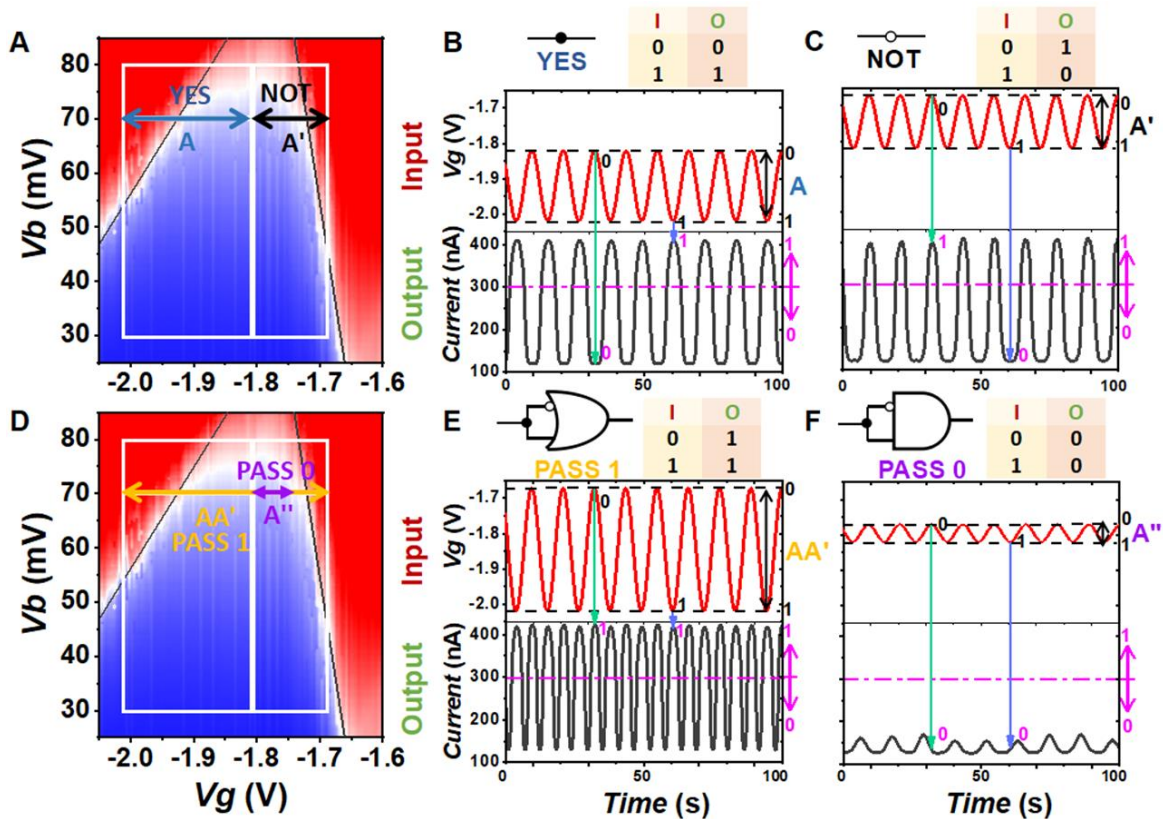


Figure 4.7: Four resettable universal 1-input logic gates. In (A and D), input gate voltages with A, A', AA' and A'' ranges are marked on the current maps, which indicate 1-input “YES”, “NOT”, “PASS 1” and “PASS 0” logic gates. (B) Equivalent circuit, truth table and corresponding Input/Output signal for 1-input “YES” gate. With the gate voltage change from -2.02 V '1' to -1.82 V '0', the current changes from 410 nA '1' to 120 nA '0'. (C) For 1-input “NOT” gate, with gate voltage change from -1.82 V '1' to -1.67 V '0', the current changes from 120 nA '0' to 405 nA '1'. (E) For 1-input “PASS 1” gate, with the gate voltage change from -2.02 V '1' to -1.67 V '0', the current changes from 410 nA '1' to 405 nA '1'. The frequency of the current signal is doubled compared with the input gate signal. (F) For 1-input “PASS 0” gate, with the gate voltage change from -1.82 V '1' to -1.77 V '0', the current changes from 120 nA '0' to 130 nA '0'. All 1-Input logic gates operate at 70 mV bias.

4.4.5 Multi-cycle stability test for 2-input logic gates

Figure 4.8 shows the multi-cycle 2-input logic operations with a time scale of 100 seconds. The 100-second scale curve for each logic operation is a small part out of the entire multi-cycle curve (see Fig. 4.9) to clearly show the curve shape. Each multi-cycle curve includes more than 37 cycles. Here we present 9 cycles to indicate the repeatability of the logic calculations, that is, its

repeatability directly related with the current conversions between resonance and Coulomb blockade regimes. The time used in a cycle is limited by the time it takes the Keithley 6430 to read the data point by point. In practical measurements, the current signal of the molecular junction is very stable as a function of bias and gate voltages, and it can last for several months without change until the low temperature is interrupted. Our measurement lasted two to three months at 4.2 K to 220 mK before we removed the sample from the Helium-3 cryostat, and the logic signal could always be measured consistently. The current signal is temperature independent in the range of 4.2 K to 220 mK. For details on how to implement the 2-input logic calculations, see Fig. 4.11 in section 4.4.6.

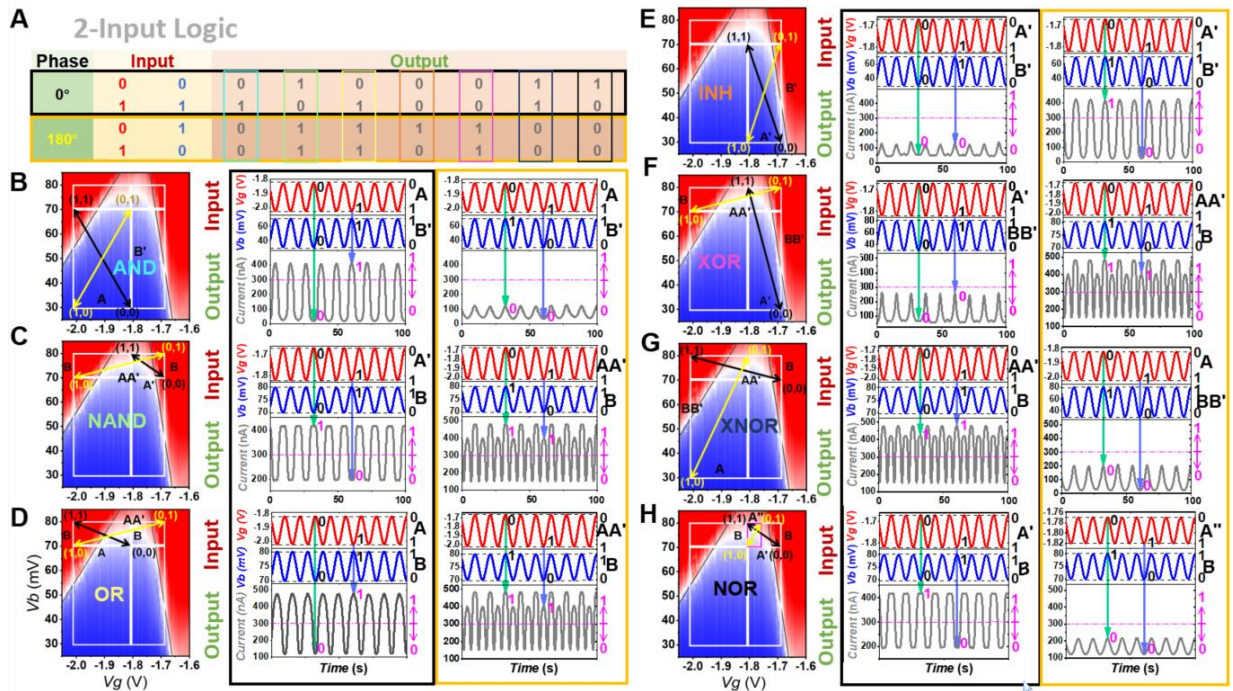


Figure 4.8: The multi-cycle repeatable test for 2-input logic gates at $T = 225$ mK. (A) The truth table for the logic gates. The color frames corresponding to different logic gates shown at (B-H), respectively. The long black and yellow frames indicate the bias signal and gate signal with same phase and with 180° phase, respectively. (B-H) are the logical operation regions marked on the current color map for different logic gates. The input and output signals are shown on the right. The black arrow and yellow arrow in the color map represent the 0° and 180° phase difference between the input bias and gate signals, respectively. The starting point and ending point of the arrows determine the voltages changing range and mark the corresponding output current states. (Red color is the “on” state of the current and blue color is the “off” state).

Figure 4.9 shows the 37-cycle curves of AA'-B measured at 0° and 180° phases to demonstrate the stability of the logical operation. From the output current curves, we can see that the resonance currents (corresponding to the “0” and “1” states of the input voltages) are stable at certain values and do not decay with time. The ~ 460 nA resonance current peaks in Fig. 4.9(A) and (B) correspond to the input (1,1) and (0,1), which belong to the ε_2 and ε_1 resonance regions respectively at $V_b = 80$ mV in Fig. 4.4(B). The ~ 400 nA resonance current peaks in Figure S11A and B correspond to input (0,0) and (1,0), which belong to the ε_1 and ε_2 resonance regions at $V_b = 70$ mV, respectively. The blockade currents (*i.e.*, the deeps) for these two curves are stable at ~ 150 nA, which indicates the stability of the 2-state Coulomb blockade region.

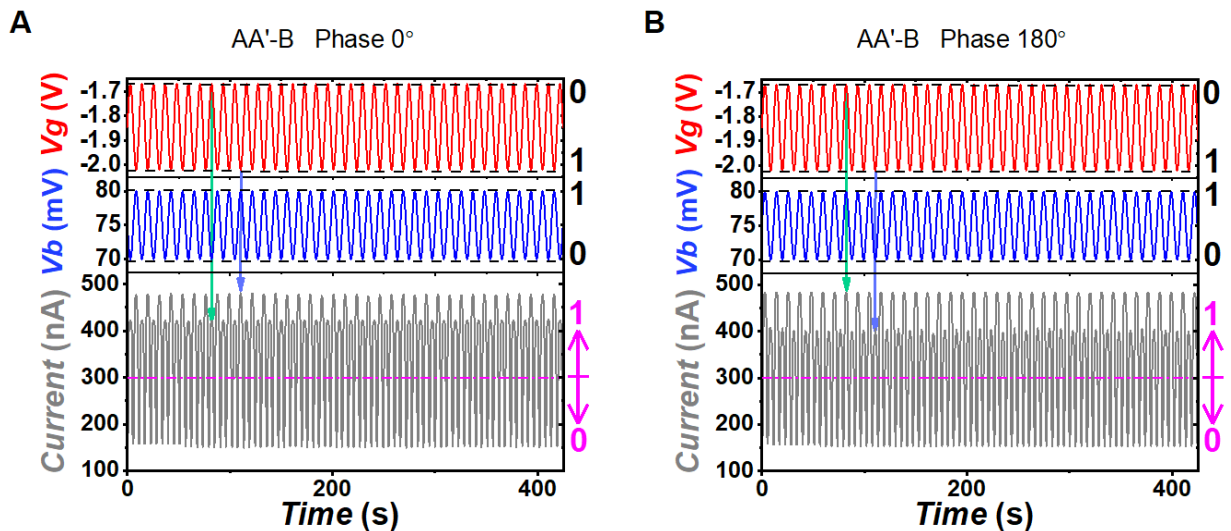


Figure 4.9: The 37-cycle repeatable curves for AA'-B at 0° and 180° phase, 225 mK.

Figure 4.10 shows the robustness of the logic output signal. It is virtually unaffected by changes in the shape and scan speed of the input signal. To clearly see the shape of the curves, we show 17 cycles in Fig. 4.10, where (A) and (B) show curves with 40 points per cycle, and (C) and (D) show curves with 4 points per cycle. Since the time axis is determined by the reading elapsed

time of the points, the switching frequency of the currents in (C) and (D) is 10 times higher than in (A) and (B). As can be seen from the figure, the distribution of the highest (~ 460 to 400 nA) and lowest (~ 150 nA) currents does not change, despite the change in switching speed and the shape of the input signal. This also verifies the stability of the logic output signal.

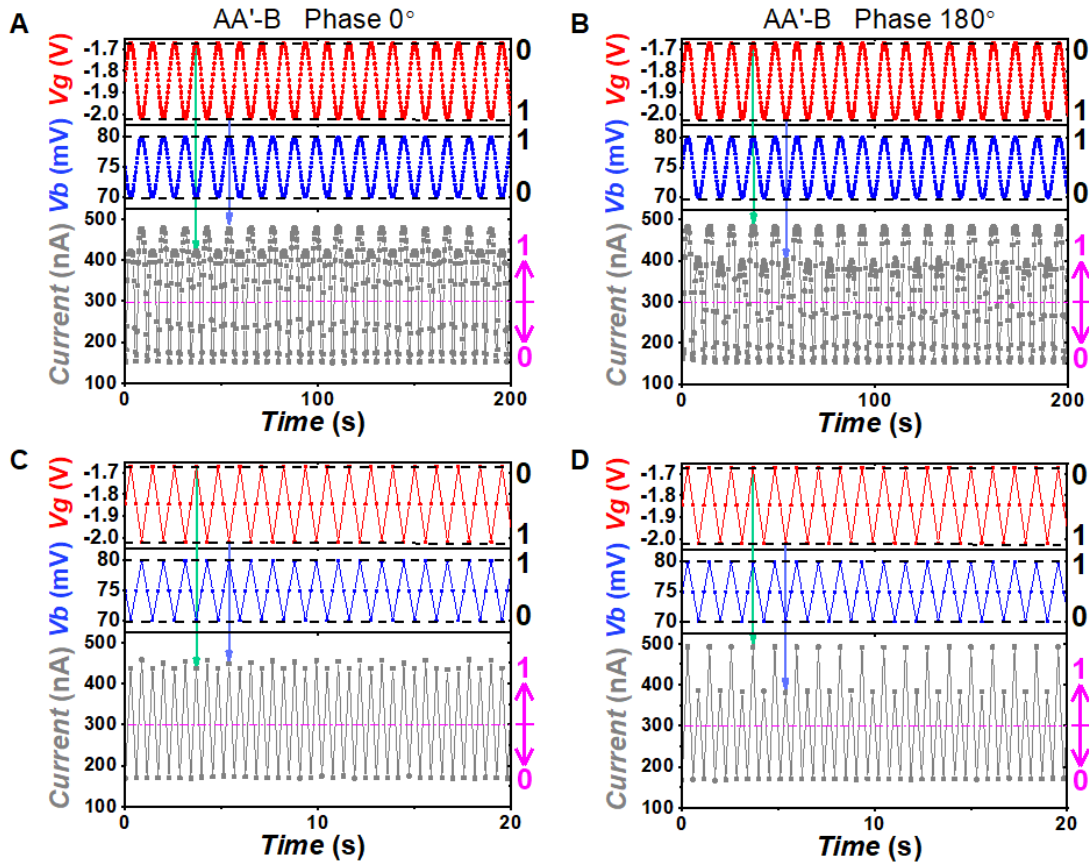


Figure 4.10: AA'-B curves with different points at 0° and 180° phases, 225 mK. (A) The AA'-B curve at 0° phase with 40 points per cycle. (B) The AA'-B curve at 180° phase with 40 points per cycle. (C) The AA'-B curve at 0° phase with 4 points per cycle. (D) The AA'-B curve at 180° phase with 4 points per cycle.

4.4.6 SELC 2-input logic gates

Based on the gate voltage ranges of the 1-input logic gates, bias voltage control is added, so that all seven universal 2-input logic gates can be realized, as demonstrated in Fig. 4.11. In the 2-input logic gates,

gate voltage is Input-signal 1 and bias voltage is Input-signal 2. The main difference between the operation of 2-input and 1-input logic gates is the phase control. The 2-input logic gate contains two input signals, and the phase difference between them determines the moving direction of the MOs relative to the bias window, thereby affecting the state of the output current. Thus, phase control combined with different operating voltage makes it possible to realize all 2-input universal logic gates.

Figure 4.11(A) shows the 2-input “AND” gate. Its operation area is defined by A-B’ in both 0° and 180° phases. The input ranges of V_g and V_b are shown on the current map. The graphs on the right are the Input/Output signals in 0° and 180° phases, respectively. In 0° phase, by changing V_g (Input-1, red curve) from -2.02 V ‘1’ to -1.82 V ‘0’ (range A) and changing V_b (Input-2, blue curve) from 70 mV ‘1’ to 30 mV ‘0’ (range B’), the current (Output, grey curve) changes from 400 nA ‘1’ to 25 nA ‘0’, *i.e.*, (1,1) → 1, (0, 0) → 0. In 180° phase, as V_g changes from ‘1’ to ‘0’ (A) and V_b changes from ‘0’ to ‘1’ (B’), the current changes from 40 nA ‘0’ to 120 nA ‘0’, *i.e.*, (1,0) → 0, (0,1) → 0. “AND” gate works as a Carry in a Half-adder logical circuit that performs an addition operation on two binary digits.

Figure 4.11(B) shows the “INH” gate. Its operation area is defined by A’-B’ in both 0° and 180° phases. In 0° phase by changing V_g from -1.82 V ‘1’ to -1.67 V ‘0’ (range A’) and changing V_b from 70 mV ‘1’ to 30 mV ‘0’ (range B’), the current changes from 120 nA ‘0’ to 50 nA ‘0’, *i.e.*, (1,1) → 0, (0,0) → 0. In 180° phase, by changing V_g from ‘1’ to ‘0’ (A’) and changing V_b from ‘0’ to ‘1’ (B’), the current changes from 25 nA ‘0’ to 420 nA ‘1’, *i.e.*, (1,0) → 0, (0,1) → 1. It works as a Borrow in Half-subtractor.

Figure 4.11(C and D) show the “XOR” and “XNOR” gates, respectively. They have different input voltage ranges in different phases. For the “XOR” gate in 0° phase, as V_g changes from -1.82 V ‘1’ to -1.67 V ‘0’ (A’) and V_b changes from 80 mV ‘1’ to 30 mV ‘0’ (BB’), current changes from 230 nA ‘0’ to 75 nA ‘0’, *i.e.*, (1,1) → 0, (0,0) → 0. At 180° phase, as V_g changes from -2.02 V ‘1’ to -1.67 V ‘0’ (AA’) and V_b changes from 70 mV ‘0’ to 80 mV ‘1’ (B), current changes from 400 nA ‘1’ to 480 nA ‘1’, *i.e.*, (1,0) → 1, (0,1) → 1. Notably, the input gate voltage and bias voltage in both phases have the same minimum value of -1.67 V and the same maximum value of 80 mV, respectively. This means that only the amplitudes of

the input voltage ranges are changed with the phase. It works as a Sum in Half-adder and Diff. in Half-subtractor. For the “XNOR” gate, with AA’ and B inputs in 0° phase, current changes from 480nA ‘1’ to 420 nA ‘1’, *i.e.*, (1,1) → 1, (0,0) → 1. In 180° phase, the corresponding inputs are A and BB’, and current changes from 25 nA ‘0’ to 200 nA ‘0’, *i.e.*, (1,0) → 0, (0,1) → 0. The input gate voltage and bias voltage in both phases have the same maximum value of -2.02 V and 80 mV, respectively.

Figure 4.11(E, F and G) show the “NAND”, “NOR” and “OR” gates. These three logic gates have the same bias voltage range in both phases, only the gate voltage range changes with phase. To avoid repetition, we omitted the curves of the input signals and kept only the input voltage range and Boolean states. For “NAND” gate, the inputs in 0° phase are A’ for V_g and B for V_b . The current changes from 200 nA '0' to 420 nA '1', *i.e.*, (1,1) → 0, (0,0) → 1. The inputs in 180° phase are AA’ and B. The current changes from 400 nA '1' to 480 nA '1', *i.e.*, (1,0) → 1, (0,1) → 1. For “NOR” gate, the Input/Output signal in 0° phase are the same with “NAND” gate (A’-B), *i.e.*, (1,1) → 0, (0,0) → 1. The inputs in 180° phase are A’’ and B. The current changes from 120 nA '0' to 210 nA '0', *i.e.*, (1,0) → 0, (0,1) → 0. For “OR” gate, the inputs in 0° phase are A for V_g and B for V_b . The current changes from 480 nA '1' to 120 nA '0', *i.e.*, (1,1) → 1, (0,0) → 0. In 180° phase, the input ranges are AA’ and B, the same as “NAND” and “XOR” gates, *i.e.*, (1,0) → 1, (0,1) → 1. To clearly show the relationship between the input and output signals, two cycles are shown in Fig. 4.11.

From Fig. 4.11 it is clear that SELC can realize all the universal 2-input logic gates within one gated single-molecule junction, in contrast to conventional CMOS (see section 4.4.9). It allows dynamic logic circuits to be scaled down to a few nanometers, and the single-junction design greatly reduces charge leakage, charge sharing, and back-gate coupling between devices. Crucially, only a 2 V gate voltage (CMOS is in the 3-15 V range) and 100 mV drive voltage (well below the 1.5-5 V of CMOS) are required to run the SELC.

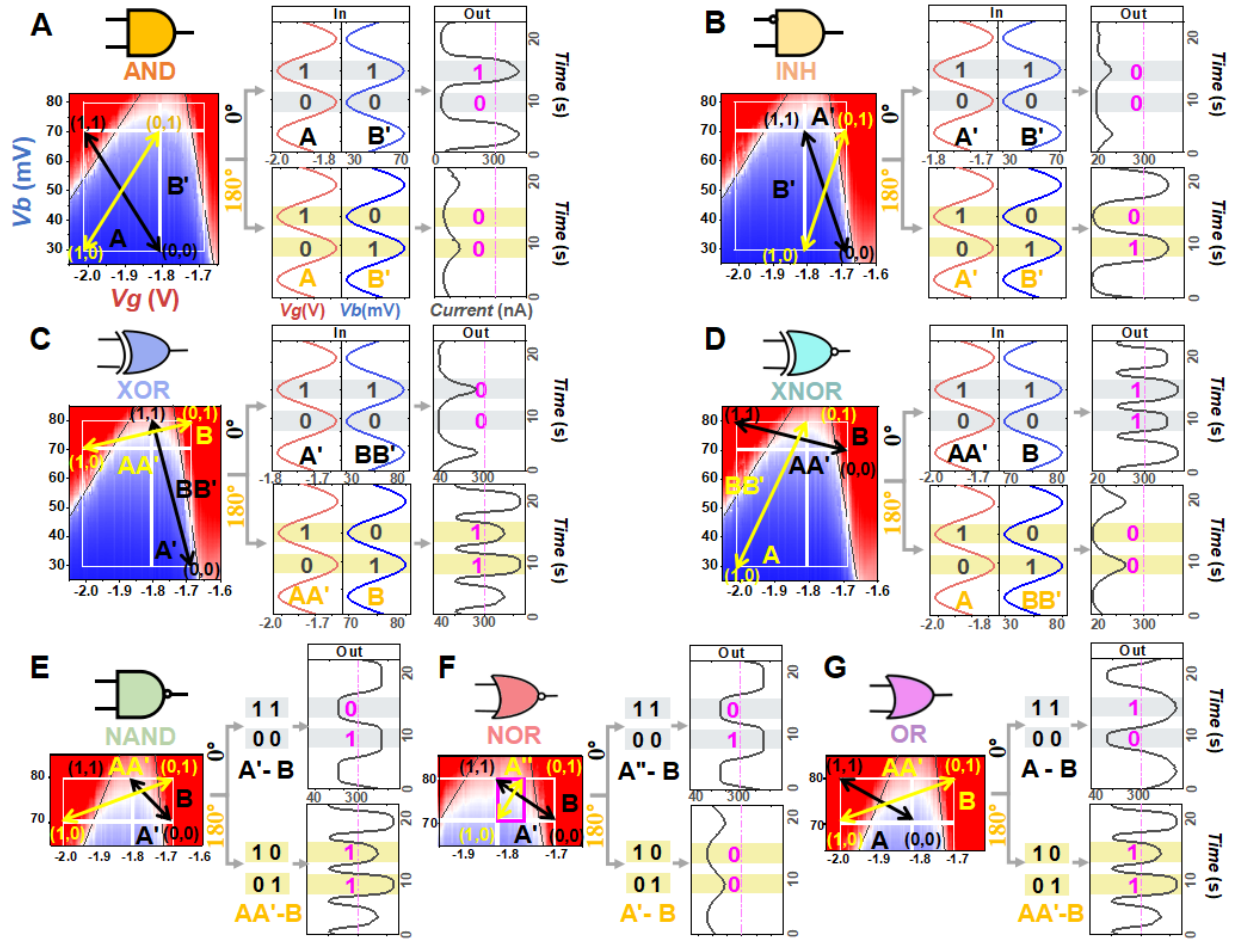


Figure 4.11: Seven resettable universal 2-Input logic gates. (A and B) “AND” and “INH” logic gates with $A-B'$ and $A'-B'$ inputs in both phases, respectively. The black and yellow arrows in current map are corresponding to the Input/Output signals in 0° phase and 180° phase, respectively. (C) “XOR” logic gate with $A'-BB'$ input in 0° phase and $AA'-B$ input in 180° phase. The input gate voltages in both phases have the same minimum value and the input bias voltages in both phases have the same maximum value, i.e., the $(0,1)$ point is the same in the voltage ranges in both phases. The highest gate voltage and the lowest bias voltage (i.e., the $(1,0)$ point) from 0° phase to 180° phase is changed. (D) “XNOR” logic gate with $AA'-B$ input in 0° phase and $A-BB'$ input in 180° phase. The input gate and bias voltages in both phases have the same maximum value, i.e., the $(1,1)$ point is the same in the voltage ranges in both phases. The lowest gate voltage and the lowest bias voltage (i.e., the $(0,0)$ point) from 180° phase to 0° phase is changed. (E, F and G) “NAND”, “NOR” and “OR” logic gates have the same input bias voltage range in both phases and change the gate voltage range with phase only. “NAND” has $A'-B$ input in 0° phase and $AA'-B$ input in 180° phase. “NOR” has $A'-B$ input in 0° phase and $A''-B$ input in 180° phase. “OR” has $A-B$ input in 0° phase and $AA'-B$ input in 180° phase.

4.4.7 Current maps measured at different scales

Figure 4.12 shows the $V_b: 231 \times V_g: 231$ points current maps scanned in different voltage ranges. Fig. 4.12(A) is the full-scale scanning current map of the conduction regimes of ϵ_2 and ϵ_1 MOs. From the map we can see that the patterning of the resonance regime of ϵ_1 is more stable than the patterning of ϵ_2 . The ϵ_2 resonance regime is displaced in the high gate voltage area (the area outside the yellow frame as shown in the map) and this displacement (the zigzag feature shown on the edge) usually happened around $V_g = -2.1$ to -2.3 V. In this conduction area (V_g higher than -2.2 V), the electrons that initially occupied ϵ_1 molecular orbital have been evacuated (ϵ_1 becomes unoccupied for a gate voltage higher than its resonance regime) and the molecule becomes more polarized by the high gate field. Therefore, when ϵ_1 is fully outside the bias window ($|V_g| > 2.2$ V), the polarized molecule will release its potential energy under a threshold gate electrostatic field (if the thickness of Al_2O_3 is 1 nm, then the electrostatic field on the surface of the alumina is $|E_g| > 2.2$ V/nm) through a slight change in its configuration. It is known that the Fc moiety has two conformations (staggered and eclipsed), which are distinguished by the angle between the two cyclopentadiene rings, and Fc can be transformed from one conformation to the other at room temperature since the barrier between them is small [55]. When a $\text{S}-(\text{CH}_2)_3\text{-Fc}-(\text{CH}_2)_9\text{-S}$ molecule is attached in the electrode gap, it can be adsorbed in a conformation that fits the gap (given in detail in reference [1], figure S5) and is fixed in this conformation at low temperature ($T < 4.2$ K) at a certain length. This is because the angle of Fc moiety affects the angle between the carbon chains on either side of it, which determines the molecular length. After the molecular junction is formed, its length is fixed by the electrode gap and therefore one of the two conformations of the Fc is selected. Thus, even when exposed to the gate electrostatic field (perpendicular to the electrode gap and not affecting the electrode distance), the change in

molecular configuration is limited. In spite of this, the similar electronic properties of these two Fc conformations [55], as we discussed in Figure S5, would provide similar conductive MOs and Ts. Therefore, a small change in the molecular configuration (see Fig. 4.12(F)) hardly changes the energy separation between the conductive MOs under the gate electrostatic field, but leads to a small energy shift of ϵ_1 and ϵ_2 MOs (see Fig. 4.12(E)). The junction configurations are optimized by DFT at the corresponding gate field, which is perpendicular to the bias direction. At a gate field of -2.2 V/nm, the energy shift is about -15 meV (see Fig. 4.12(D and E)), which accounts for the shift we observe in experiments with high gate voltage (see the displacement in Fig. 4.12(A)).

As for the ϵ_1 resonance regime, since ϵ_1 is the first conductive MO, the molecule is electrically neutral when ϵ_1 is located in the bias window and the gate voltage is low. Therefore, the current pattern of the ϵ_1 resonance regime is relatively stable. That is why we mainly focus on the low gate voltage region, using the edges of ϵ_1 (r' and r'') in the experiment to calculate the K_G and K_B parameters and determine the *MOs shift* by the crossing point of ϵ_1 (given in details in reference [1], SI-S3 (4)).

However, there is still a slight shift in the entire pattern across the different scan ranges. That is, the values of r' and r'' slopes in these three maps are the same, while the gate voltages corresponding to the crossing points are slightly shifted. As shown in Fig. 4.12(B and C), we zoomed in and scanned the yellow frame region and the region under positive bias only and observed very clear and stable patterns with $V_g = -1.67$ V and -1.64 V for the ϵ_1 crossing points, respectively. Additional scans were performed in the small voltage region near the ϵ_1 crossing point. The results indicate that if the voltage range is positioned in a small region that barely affects the external electrostatic potential of the molecular junction (*e.g.*, logic operating voltage area), then the current signal in this region is highly reproducible. Therefore, the corresponding “on/off”

signal of SELC is very stable even when different voltage ranges are used in the logic operation. In addition, the relative addressing method adopted by the logic operations further avoids the impact of random MOs shifts on the functionality of SELC.

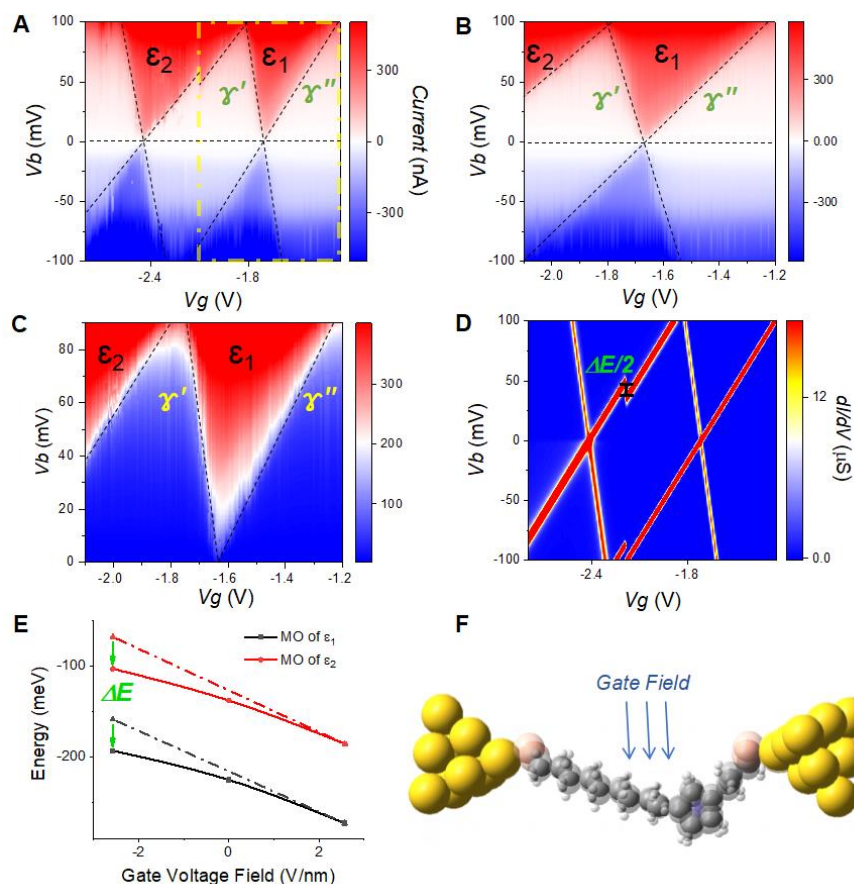


Figure 4.12: The measured 231×231 points current maps for different voltage ranges at 225 mK and the energy shift caused by slight conformational changes of the molecule under high gate voltage fields calculated by DFT. (A) The whole scan for ϵ_2 and ϵ_1 , which represent the resonance regimes contributed by the conductive MOs. (B) and (C) are the zoom-in scans of the voltage ranges within the yellow frame marked in (A). The gate voltages for the crossing points of ϵ_1 at (A), (B) and (C) maps are 1.71 V, 1.67 V and 1.64 V, respectively. γ' and γ'' indicate the edges between the resonant regime of ϵ_1 and the Coulomb blockade regions. (D) is the 101×142 points theoretical conductance map, taking into account the -15 meV energy shift due to slight conformational changes of the molecule when the gate voltage is higher than -2.2 V. (E) is the energy evolution of the two adjacent conductive MOs ϵ_1 and ϵ_2 along the gate voltage field. (F) indicates the slight conformational changes under different gate voltage fields. The calculations were performed in Gaussian package [56] with the B3LYP functional and LANL2DZ basis set.

4.4.8 Measured differential conductance maps of different Fc-based molecular junctions.

To further demonstrate the general feature of two adjacent conductive MOs with stable ~ 100 meV energy separation in Fc-based single-electron transistors (SETs), four differential conductance maps within 0~100 mV voltage range of different Fc-based molecular SETs: Au/S-(CH₂)₄-Fc-(CH₂)₄-S/Au [27], Au/S-(CH₂)₆-Fc-(CH₂)₆-S/Au, Au/S-DPA-CH₂-Fc-(CH₂)₂-S/ Au [23] and Au/S-DPA-Fc-(CH₂)₂-S/Au [23] have been shown in Fig. 4.13. These SETs all show two resonance regions overlapping at around 100 mV, same as Fig. 4.13(B) in the main text. The DFT-NEGF calculations for the ΔMOs (100 to 180 meV) of these four molecules also confirm the experimental observations. This further suggests that the two adjacent conductive MOs with an energy difference of about 100 meV are a unique feature of the Fc-based SETs.

Since symmetric molecules lack the built-in asymmetries of molecular junctions, the polarities of MOs of the junctions along bias direction arise mainly from the asymmetries of molecule-electrode contacts. Whereas these polarities are not intrinsic to the molecules, they are more susceptible to external electrostatic fields than the intrinsic polarities, and so the K_B varies with bias and gate voltages (this is supported by the DFT-NEGF calculations). As shown in Fig. 4.13(A) and (B), the edges of the resonance and Coulomb blockade regions deviate slightly from the straight dashed lines. And for the Fc-based asymmetric molecules containing π -conjugated tether (*i.e.*, the DPA unit) on one side, the molecular orbitals contributed by the π -conjugated tether are easily broadened by the electrodes, leading to wide edges shown in Figure S14C and D. However, these edges are consistent with the straight dashed lines. Therefore, to produce straight and narrow edges, the Au/S-(CH₂)₃-Fc-(CH₂)₉-S/Au molecular junction is targeted.

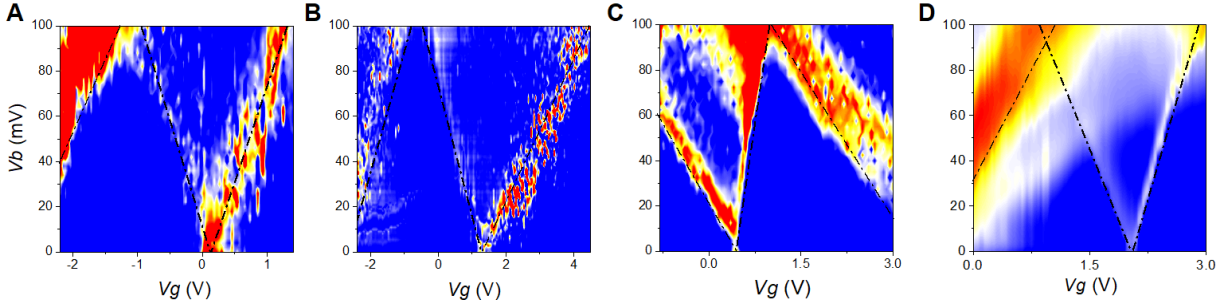


Figure 4.13: The measured differential conductance maps for different Fc-based molecular SETs with 0 to 100 mV bias voltage at $T = 4.2$ K. (A) The map for Au/S-(CH₂)₄-Fc-(CH₂)₄-S/Au molecular junction [27]. (B) The map for Au/S-(CH₂)₆-Fc-(CH₂)₆-S/Au molecular junction (the electromigration curve see Sample-O6, Figure S3). (C) The map for Au/S-DPA-CH₂-Fc-(CH₂)₂-S/Au molecular junction [23]. (D) The map for Au/S-DPA-Fc-(CH₂)₂-S/Au molecular junction [23].

4.4.9 Functionality comparison with conventional CMOS

Conventional silicon-based CMOS (complementary metal oxide semiconductor) remains by far the most widely used technology for preparing logic gates. However, since it requires the integration of 4 to 16 devices to complete the design of a 2-input logic gate (see Fig. 4.14), the mutual interference and charge leakage of devices during dynamic logic calculations hinder their miniaturization. Here, by constructing all 7 universal 2-input logic gates, we can compare CMOS and SELC, and we highlight that our proposed SELC model requires only a single molecule device in the core region for logic computation (see Fig. 4.11 for details), which greatly reduces device density, shrinks device size, and lowers back-gate coupling. Interestingly, as a current-driven device, SELC sets the maximum power consumption of all logic gates to 40 nW ($I_{MAX} \cdot Vb$), an upper limit that is independent of the switching rate. In contrast, the energy dissipation of a CMOS element increases linearly with the switching rate ($C_L V_{DD}^2$ per switching cycle), *e.g.*, at least 50 μ W for CMOS with a clock rate of ~ 500 MHz and an average load capacitance of ~ 15 fF/gate at 2.5 V supply. However, the shortcoming of SELC from a device engineering perspective is that it requires an electrode gap in the range of 1.7 to 2.3 nm to ensure the proper connection of the

molecule and electrodes. Therefore, further design and technological advances are needed to realize the SELC for practical applications, advancing the current prototype to a mass-producible simple, stable and versatile single-molecule logic device.

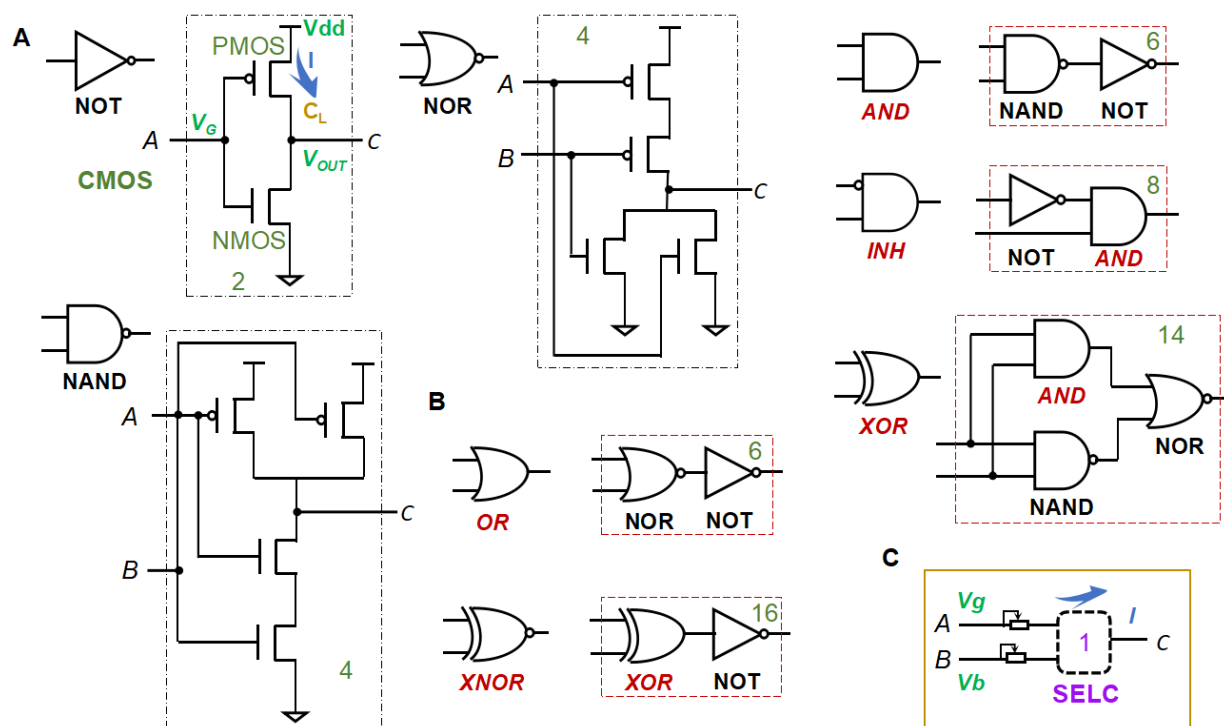


Figure 4.14: Comparing the functionality of CMOS and SELC by building all universal logic gates. (A) The three basic logic gates “NOT”, “NAND” and “NOR” as obtained by CMOS. The number in each rectangular box is the number of CMOS components used in the logic gate. V_{dd} , V_{OUT} and V_G indicate the bias, output and gate (input) voltages of CMOS, respectively. I indicates the charging current. C_L is the load capacitor. (B) The five universal logic gates “OR”, “XNOR”, “AND”, “INH” and “XOR” consist of the three basic logic gates in (A) and can therefore be constructed by CMOS. The number of CMOS components is marked in each box. Both A and B are the input gate voltages, C is the output voltage. (C) By controlling the range of input voltages (A: gate voltage V_g and B: bias voltage V_b) separately, SELC can create all the universal logic gates by switching the output current (C: I) through a single molecular junction.

4.4.10 Leaking Current of the SETs

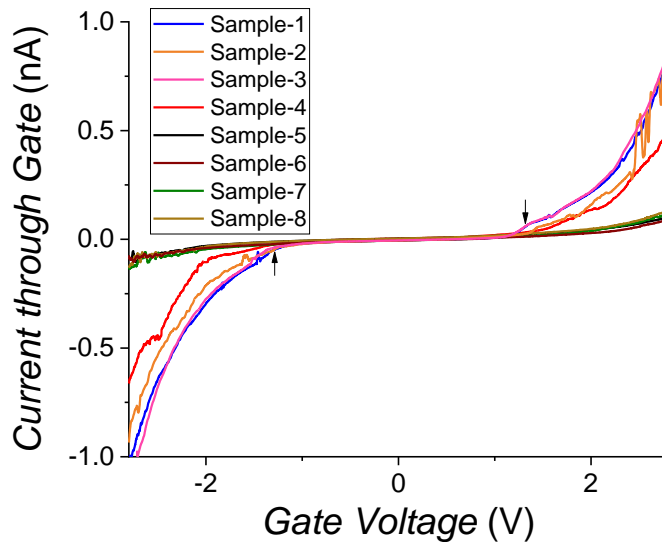


Figure 4.15: Current measured through the Al_2O_3 layers of SETs at 4 K when biasing the gate. Black arrows indicate gate voltage, where the average tunneling currents for samples 1 to 4 are below 0.1 nA.

Once the SETs are fabricated, the leakage current between the source/drain and the gate is always checked. In operative devices, the leakage corresponds to the tunneling current through a thin (2~1 nm) Al_2O_3 layer. The gate resistance of a well-performing SETs in the first pre-screening should be greater than 100 G Ω at 0.1 V. According to reference [27], the tunneling I-V curve through the alumina barrier between the gate and the source/drain provides important information for determining the safety window for the gate voltage (within which the isolation characteristics of the gate are stable). Here, we measured the leakage current of several SETs, whose source-to-drain currents can reach 100 nA in the resonance regime (three orders of magnitude larger than the leakage current). It helps to understand not only the safety window for the gate voltage of SETs, but also the difference between the leakage current through the gate and the current through the source-drain (see Figure 1D in the main text). Fig. 4.15 shows representative leaking current curves

through SETs when biasing the gate. For samples 1 to 4, the leaking current is lower than 0.1 nA within -1.5 V to 1.5 V gate voltage range, providing a safety window of -3 V to 3 V before compromising the isolation barrier to the gate (this doubling relationship is found empirically and may depend on the curve of the leakage current through the gate *vs* the voltage). For samples 5 to 8, the leaking current is lower than 0.1 nA within -2.5 V to 2.5 V gate voltage range, with safety windows about -5 V to 5 V. The safety window is defined for leakage current < 1 nA; for leakage currents of > 1 nA the Al_2O_3 layer can fail leading to a short (which is clearly recognized as a sudden increase of the current to about 0.1 mA, completely overtaking the molecular current signal). Therefore, only SETs with a safety window larger than -3V to 3V can show a stable Coulomb blockade signal in this range. In the SETs reported in this work, the leakage current through the Al_2O_3 layer is below 0.1 nA over the measurement range, which is negligible compared to the resonant current through the molecular junction (about several hundred nanoamps).

4.4.11 Stability of SELC under magnetic field

Normally, the ground state of either the eclipsed or staggered conformation of the Fc moiety is a low spin ($S = 0$) state [55, 57], and the energy required to excite it to the high spin ($S = 2$) state is predicted to be over 40 kcal mol⁻¹ [57]. Once the molecule transits from the low-spin to the high-spin state, it undergoes a dramatic conformational change and begins to respond to magnetic fields (e.g., the Kondo resonance, which is a many-electron phenomenon that occurs when a conductive MO has non-zero spin). If the Kondo resonance occurs, it should be characterized by a sharp zero-bias conductance peak [20] in the region near the charge degeneracy point of ϵ_1 marked by the black arrow in Fig. 4.16. However, the conductance maps do not show

any peak in this region and show little change as the magnetic field increases to 1 T (compare Fig. 4.16 (A), (C) to (B), (D)). This means that the molecule is stable in the $S = 0$ state and is not excited to the $S = 2$ state by a 1 T magnetic field. Furthermore, the small changes in the conductance map indicate that for the molecule in $S = 0$ state, the spin polarization of the molecule has a very limited effect on the conductivity when the magnetic field is below 1 T. This is due to the fact that both spin-up and spin-down orbitals are allowed within the width of the level broadening after the molecule is coupled to the electrode leads on both sides. Unless the magnetic field is strong enough, the energy separation of the MOs caused by the spin polarization cannot be distinguished. This is also supported by the DFT calculations. The results calculated with the UB3LYP (unrestricted B3LYP that allows unpaired spins) method show that the molecular junctions in the $S = 0$ state are spin-degenerate at 0 T magnetic field. Moreover, the transmission spectrum of the spin polarized state does not change significantly compared to that of the unpolarized state (see Fig. 4.16(E), calculated in ATK18 [58]). Thus, the spin polarization does not affect the theoretical results and the robustness of SELC in the absence of magnetic field or at low magnetic fields (~ 1 T).

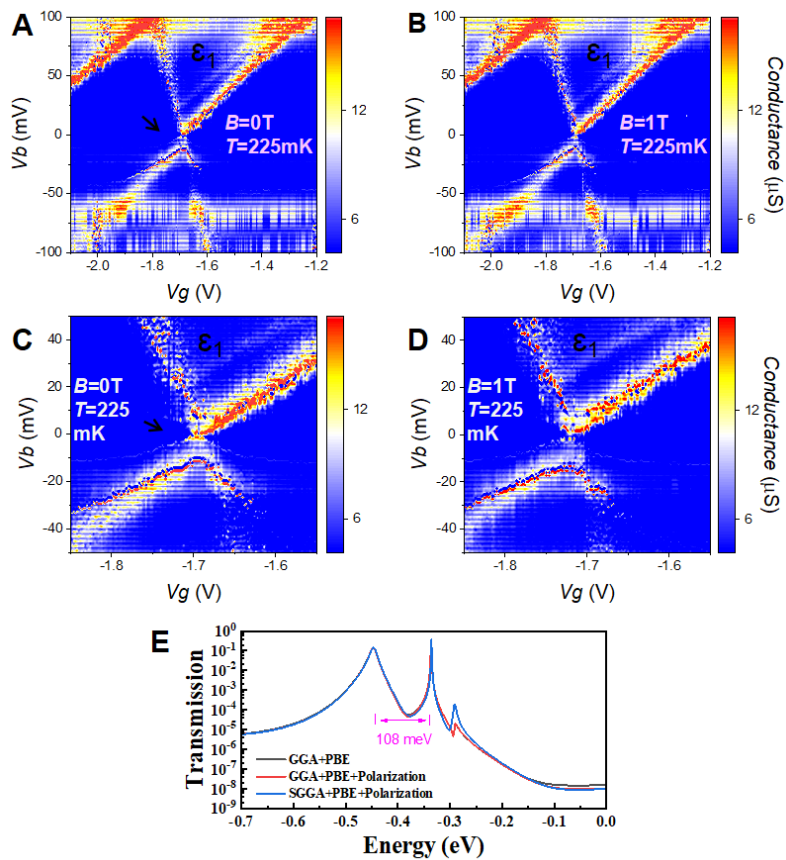


Figure 4.16: Conductance maps measured under magnetic fields and the spin-polarized transmission spectra calculated by DFT. (A) and (B) are 231×231 points conductance maps measured at 225 mK under 0 T and 1 T magnetic fields, respectively. (C) and (D) are 151×151 points conductance maps for a small voltage range at 225 mK under 0 T and 1 T magnetic fields, respectively. (E) is a comparison of the spin-polarized Ts and unpolarized Ts of the optimized tip-to-tip molecular junction at 0 V bias.

4.5 Conclusion

In this chapter we report molecular-scale SELC in a three-terminal SET by utilizing adjacent conductive MOs provided by a single Fc-based molecule. Its operating principle is based on predictable and reliable current conversions modulated by voltages crossing the stable Coulomb blockade regime, avoiding dependence on absolute current and improving function reproducibility. Compared with other approaches [23-25, 28, 31], the non-conjugated asymmetric Fc-based molecule naturally provides logic operations via its robust and unique Coulomb blockade characteristics. The isolation provided by the asymmetric n-alkyl ($n > 3$) linkers on either side of the Fc moiety ensures narrow MO levels, efficiently

suppressing current in the Blockade regime and enabling encoding of information via orthogonal modulation for the realization of sophisticated operation functions. This results in clear and multi-cycle stable current signals controlled by two orthogonal electrostatic fields, enabling in-situ implementation of all four universal 1-input and all seven universal 2-input logic gates in a single molecule with high stability. Through phase control of an external circuit, the benefits of implementing multiple logic operations within a single molecule (instead of connecting several separate devices with switching characteristics in series) are low charge leakage, with no mutual interference, small functional area (~ 2 nm), low operating voltage (because the applied potential only drops over one element [6]) and simple device construction. Crucially, our design can be extended to multi-channel mesoscopic Coulomb blockade systems, field-effect single molecules or molecular layers, with promising future applications of SELC in realizing multifunctional nanodevices including frequency multipliers, diodes, switches, voltage indicators, and calculators, among others.

4.6 References

- [1] R. Liu *et al.*, "Stable Universal 1- and 2-Input Single-Molecule Logic Gates," *Adv Mater*, p. e2202135, May 12 2022, doi: 10.1002/adma.202202135.
- [2] X. Chen *et al.*, "Molecular diodes with rectification ratios exceeding 105 driven by electrostatic interactions," *Nature Nanotechnology*, vol. 12, no. 8, pp. 797-803, 2017/08/01 2017, doi: 10.1038/nnano.2017.110.
- [3] C. Guo *et al.*, "Molecular rectifier composed of DNA with high rectification ratio enabled by intercalation," (in eng), *Nat Chem*, vol. 8, no. 5, pp. 484-90, May 2016, doi: 10.1038/nchem.2480.
- [4] C. Jia *et al.*, "Covalently bonded single-molecule junctions with stable and reversible photoswitched conductivity," (in eng), *Science*, vol. 352, no. 6292, pp. 1443-5, Jun 17 2016, doi: 10.1126/science.aaf6298.
- [5] S. Kumar, M. Merelli, W. Danowski, P. Rudolf, B. L. Feringa, and R. C. Chiechi, "Molecular Memory: Chemical Locking in Molecular Tunneling Junctions Enables Nonvolatile Memory with Large On–Off Ratios (Adv. Mater. 15/2019)," *Advanced Materials*, vol. 31, no. 15, p. 1970111, 2019, doi: <https://doi.org/10.1002/adma.201970111>.
- [6] Y. Han *et al.*, "Electric-field-driven dual-functional molecular switches in tunnel junctions," (in eng), *Nat Mater*, vol. 19, no. 8, pp. 843-848, Aug 2020, doi: 10.1038/s41563-020-0697-5.
- [7] L. Bogani and W. Wernsdorfer, "Molecular spintronics using single-molecule magnets," *Nature Materials*, vol. 7, no. 3, pp. 179-186, 2008/03/01 2008, doi: 10.1038/nmat2133.
- [8] C. Joachim, N. Renaud, and M. Hliwa, "The Different Designs of Molecule Logic Gates," *Advanced Materials*, vol. 24, no. 2, pp. 312-317, 2012, doi: <https://doi.org/10.1002/adma.201104270>.
- [9] N. Zhang, W.-Y. Lo, A. Jose, Z. Cai, L. Li, and L. Yu, "A Single-Molecular AND Gate Operated with Two Orthogonal Switching Mechanisms," *Advanced Materials*, vol. 29, no. 28, p. 1701248, 2017, doi: <https://doi.org/10.1002/adma.201701248>.
- [10] F. Meng *et al.*, "Orthogonally modulated molecular transport junctions for resettable electronic logic gates," *Nature Communications*, vol. 5, no. 1, p. 3023, 2014/01/07 2014, doi: 10.1038/ncomms4023.
- [11] S. Cai *et al.*, "Light-Driven Reversible Intermolecular Proton Transfer at Single-Molecule Junctions," *Angewandte Chemie International Edition*, <https://doi.org/10.1002/anie.201813137> vol. 58, no. 12, pp. 3829-3833, 2019/03/18 2019, doi: <https://doi.org/10.1002/anie.201813137>.
- [12] W. H. Soe *et al.*, "Demonstration of a NOR logic gate using a single molecule and two surface gold atoms to encode the logical input," *Physical Review B*, vol. 83, no. 15, p. 155443, 04/26/ 2011, doi: 10.1103/PhysRevB.83.155443.
- [13] Y. Liu, A. Offenhäusser, and D. Mayer, "An Electrochemically Transduced XOR Logic Gate at the Molecular Level," *Angewandte Chemie International Edition*, <https://doi.org/10.1002/anie.200906333> vol. 49, no. 14, pp. 2595-2598, 2010/03/29 2010, doi: <https://doi.org/10.1002/anie.200906333>.
- [14] W. Du, T. Wang, H.-S. Chu, and C. A. Nijhuis, "Highly efficient on-chip direct electronic–plasmonic transducers," *Nature Photonics*, vol. 11, no. 10, pp. 623-627, 2017/10/01 2017, doi: 10.1038/s41566-017-0003-5.

- [15] H. Song, Y. Kim, Y. H. Jang, H. Jeong, M. A. Reed, and T. Lee, "Observation of molecular orbital gating," (in eng), *Nature*, vol. 462, no. 7276, pp. 1039-43, Dec 24 2009, doi: 10.1038/nature08639.
- [16] H. Park, J. Park, A. K. Lim, E. H. Anderson, A. P. Alivisatos, and P. L. McEuen, "Nanomechanical oscillations in a single-C60 transistor," (in eng), *Nature*, vol. 407, no. 6800, pp. 57-60, Sep 7 2000, doi: 10.1038/35024031.
- [17] S. Goswami *et al.*, "Charge disproportionate molecular redox for discrete memristive and memcapacitive switching," (in eng), *Nat Nanotechnol*, vol. 15, no. 5, pp. 380-389, May 2020, doi: 10.1038/s41565-020-0653-1.
- [18] J. Park *et al.*, "Coulomb blockade and the Kondo effect in single-atom transistors," (in eng), *Nature*, vol. 417, no. 6890, pp. 722-5, Jun 13 2002, doi: 10.1038/nature00791.
- [19] L. Yuan *et al.*, "Controlling the direction of rectification in a molecular diode," (in eng), *Nat Commun*, vol. 6, p. 6324, Mar 2 2015, doi: 10.1038/ncomms7324.
- [20] W. Liang, M. P. Shores, M. Bockrath, J. R. Long, and H. Park, "Kondo resonance in a single-molecule transistor," (in eng), *Nature*, vol. 417, no. 6890, pp. 725-9, Jun 13 2002, doi: 10.1038/nature00790.
- [21] S. J. van der Molen *et al.*, "Light-controlled conductance switching of ordered metal-molecule-metal devices," (in eng), *Nano Lett*, vol. 9, no. 1, pp. 76-80, Jan 2009, doi: 10.1021/nl802487j.
- [22] J. Zhou, K. Wang, B. Xu, and Y. Dubi, "Photoconductance from Exciton Binding in Molecular Junctions," *Journal of the American Chemical Society*, vol. 140, no. 1, pp. 70-73, 2018/01/10 2018, doi: 10.1021/jacs.7b10479.
- [23] L. Yuan *et al.*, "Transition from direct to inverted charge transport Marcus regions in molecular junctions via molecular orbital gating," (in eng), *Nat Nanotechnol*, vol. 13, no. 4, pp. 322-329, Apr 2018, doi: 10.1038/s41565-018-0068-4.
- [24] P. Gehring *et al.*, "Complete mapping of the thermoelectric properties of a single molecule," *Nat Nanotechnol*, vol. 16, no. 4, pp. 426-430, Apr 2021, doi: 10.1038/s41565-021-00859-7.
- [25] P. Gehring *et al.*, "Distinguishing Lead and Molecule States in Graphene-Based Single-Electron Transistors," *ACS Nano*, vol. 11, no. 6, pp. 5325-5331, 2017/06/27 2017, doi: 10.1021/acsnano.7b00570.
- [26] P. Gehring *et al.*, "Efficient heating of single-molecule junctions for thermoelectric studies at cryogenic temperatures," *Applied Physics Letters*, vol. 115, no. 7, p. 073103, 2019/08/12 2019, doi: 10.1063/1.5118861.
- [27] A. R. Garrigues, L. Wang, E. del Barco, and C. A. Nijhuis, "Electrostatic control over temperature-dependent tunnelling across a single-molecule junction," *Nature Communications*, vol. 7, no. 1, p. 11595, 2016/05/23 2016, doi: 10.1038/ncomms11595.
- [28] S. Kubatkin *et al.*, "Single-electron transistor of a single organic molecule with access to several redox states," (in eng), *Nature*, vol. 425, no. 6959, pp. 698-701, Oct 16 2003, doi: 10.1038/nature02010.
- [29] P. Puczkarski *et al.*, "Three-terminal graphene single-electron transistor fabricated using feedback-controlled electroburning," *Applied Physics Letters*, vol. 107, no. 13, p. 133105, 2015/09/28 2015, doi: 10.1063/1.4932133.

- [30] H. B. Heersche *et al.*, "Electron Transport through Single Mn_{12} Molecular Magnets," *Phys Rev Lett*, vol. 96, no. 20, p. 206801, 05/23/ 2006, doi: 10.1103/PhysRevLett.96.206801.
- [31] S. Caneva *et al.*, "A Mechanically Tunable Quantum Dot in a Graphene Break Junction," *Nano Letters*, vol. 20, no. 7, pp. 4924-4931, 2020/07/08 2020, doi: 10.1021/acs.nanolett.0c00984.
- [32] D. Goldhaber-Gordon, H. Shtrikman, D. Mahalu, D. Abusch-Magder, U. Meirav, and M. A. Kastner, "Kondo effect in a single-electron transistor," *Nature*, vol. 391, no. 6663, pp. 156-159, 1998/01/01 1998, doi: 10.1038/34373.
- [33] J. J. Parks, A. R. Champagne, G. R. Hutchison, S. Flores-Torres, H. D. Abruña, and D. C. Ralph, "Tuning the Kondo Effect with a Mechanically Controllable Break Junction," *Phys Rev Lett*, vol. 99, no. 2, p. 026601, 07/11/ 2007, doi: 10.1103/PhysRevLett.99.026601.
- [34] X. Guo, Q. Zhu, L. Zhou, W. Yu, W. Lu, and W. Liang, "Evolution and universality of two-stage Kondo effect in single manganese phthalocyanine molecule transistors," *Nature Communications*, vol. 12, no. 1, p. 1566, 2021/03/10 2021, doi: 10.1038/s41467-021-21492-x.
- [35] B. Fu, M. A. Mosquera, G. C. Schatz, M. A. Ratner, and L.-Y. Hsu, "Photoinduced Anomalous Coulomb Blockade and the Role of Triplet States in Electron Transport through an Irradiated Molecular Transistor," *Nano Letters*, vol. 18, no. 8, pp. 5015-5023, 2018/08/08 2018, doi: 10.1021/acs.nanolett.8b01838.
- [36] R. Jorn and T. Seideman, "Competition between current-induced excitation and bath-induced decoherence in molecular junctions," *The Journal of Chemical Physics*, vol. 131, no. 24, p. 244114, 2009/12/28 2009, doi: 10.1063/1.3276281.
- [37] T. Seideman and H. Guo, "QUANTUM TRANSPORT AND CURRENT-TRIGGERED DYNAMICS IN MOLECULAR TUNNEL JUNCTIONS," *Journal of Theoretical and Computational Chemistry*, vol. 02, no. 03, pp. 439-458, 2003/09/01 2003, doi: 10.1142/S0219633603000616.
- [38] C. Hua, B. Huang, Y. Jiang, S. Zhu, and R. Cui, "Near-infrared-IIb probe affords ultrahigh contrast inflammation imaging," *RSC Adv*, vol. 10, no. 55, pp. 33602-33607, Sep 7 2020, doi: 10.1039/d0ra06249a.
- [39] S. J. Kim *et al.*, "One electron-based smallest flexible logic cell," *Applied Physics Letters*, vol. 101, no. 18, p. 183101, 2012/10/29 2012, doi: 10.1063/1.4761935.
- [40] S. J. Shin *et al.*, "Room-temperature charge stability modulated by quantum effects in a nanoscale silicon island," (in eng), *Nano Lett*, vol. 11, no. 4, pp. 1591-7, Apr 13 2011, doi: 10.1021/nl1044692.
- [41] M. El Abbassi *et al.*, "Controlled Quantum Dot Formation in Atomically Engineered Graphene Nanoribbon Field-Effect Transistors," *ACS Nano*, vol. 14, no. 5, pp. 5754-5762, 2020/05/26 2020, doi: 10.1021/acsnano.0c00604.
- [42] M. Camarasa-Gómez *et al.*, "Mechanically Tunable Quantum Interference in Ferrocene-Based Single-Molecule Junctions," (in eng), *Nano Lett*, vol. 20, no. 9, pp. 6381-6386, Sep 9 2020, doi: 10.1021/acs.nanolett.0c01956.
- [43] X. Zhao, G. Kastlunger, and R. Stadler, "Quantum interference in coherent tunneling through branched molecular junctions containing ferrocene centers," *Physical Review B*, vol. 96, no. 8, p. 085421, 08/15/ 2017, doi: 10.1103/PhysRevB.96.085421.

- [44] D. Thompson and C. A. Nijhuis, "Even the Odd Numbers Help: Failure Modes of SAM-Based Tunnel Junctions Probed via Odd-Even Effects Revealed in Synchrotrons and Supercomputers," *Accounts of Chemical Research*, vol. 49, no. 10, pp. 2061-2069, 2016/10/18 2016, doi: 10.1021/acs.accounts.6b00256.
- [45] L. Cao *et al.*, "The supramolecular structure and van der Waals interactions affect the electronic structure of ferrocenyl-alkanethiolate SAMs on gold and silver electrodes," *Nanoscale Advances*, 10.1039/C9NA00107G vol. 1, no. 5, pp. 1991-2002, 2019, doi: 10.1039/C9NA00107G.
- [46] Q. Wang *et al.*, "Single-Atom Switches and Single-Atom Gaps Using Stretched Metal Nanowires," *ACS Nano*, vol. 10, no. 10, pp. 9695-9702, 2016/10/25 2016, doi: 10.1021/acsnano.6b05676.
- [47] W. Nawrocki, "Electrical and thermal conductance quantization in nanostructures," *Journal of Physics: Conference Series*, vol. 129, 2008, doi: 10.1088/1742-6596/129/1/012023.
- [48] A. Singh, D. H. Dahanayaka, A. Biswas, L. A. Bumm, and R. L. Halterman, "Molecularly Ordered Decanethiolate Self-Assembled Monolayers on Au(111) from in Situ Cleaved Decanethioacetate: An NMR and STM Study of the Efficacy of Reagents for Thioacetate Cleavage," *Langmuir*, vol. 26, no. 16, pp. 13221-13226, 2010/08/17 2010, doi: 10.1021/la100103k.
- [49] H. Häkkinen, "The gold–sulfur interface at the nanoscale," *Nature Chemistry*, vol. 4, no. 6, pp. 443-455, 2012/06/01 2012, doi: 10.1038/nchem.1352.
- [50] P. Gehring *et al.*, "Quantum interference in graphene nanoconstrictions," *Nano letters*, vol. 16, no. 7, pp. 4210-4216, 2016.
- [51] C. Jia *et al.*, "Redox Control of Charge Transport in Vertical Ferrocene Molecular Tunnel Junctions," *Chem*, vol. 6, no. 5, pp. 1172-1182, 2020/05/14/ 2020, doi: <https://doi.org/10.1016/j.chempr.2020.02.018>.
- [52] H. Jeong *et al.*, "A new approach for high-yield metal–molecule–metal junctions by direct metal transfer method," *Nanotechnology*, vol. 26, no. 2, p. 025601, 2014/12/16 2014, doi: 10.1088/0957-4484/26/2/025601.
- [53] J. J. Henderson, C. M. Ramsey, E. del Barco, A. Mishra, and G. Christou, "Fabrication of nanogapped single-electron transistors for transport studies of individual single-molecule magnets," *Journal of Applied Physics*, vol. 101, no. 9, p. 09E102, 2007/05/01 2007, doi: 10.1063/1.2671613.
- [54] S. Alavi, B. Larade, J. Taylor, H. Guo, and T. Seideman, "Current-triggered vibrational excitation in single-molecule transistors," *Chemical Physics*, vol. 281, no. 2, pp. 293-303, 2002/08/01/ 2002, doi: [https://doi.org/10.1016/S0301-0104\(02\)00567-0](https://doi.org/10.1016/S0301-0104(02)00567-0).
- [55] N. Mohammadi, A. Ganesan, C. T. Chantler, and F. Wang, "Differentiation of ferrocene D5d and D5h conformers using IR spectroscopy," *Journal of Organometallic Chemistry*, vol. 713, pp. 51-59, 2012/08/15/ 2012, doi: <https://doi.org/10.1016/j.jorganchem.2012.04.009>.
- [56] *Gaussian 16 Rev. C.01*. (2016). Wallingford, CT.
- [57] T. P. Gryaznova, S. A. Katsyuba, V. A. Milyukov, and O. G. Sinyashin, "DFT study of substitution effect on the geometry, IR spectra, spin state and energetic stability of the ferrocenes and their pentaphospholyl analogues," *Journal of Organometallic Chemistry*, vol. 695, no. 24, pp. 2586-2595, 2010/11/15/ 2010, doi: <https://doi.org/10.1016/j.jorganchem.2010.08.031>.
- [58] Q. Simulator, in *Quantum ATK version 2018.06, Synopsis Quantum ATK.*, 2018.

APPENDIX A: DESIGN OF ANTENNAS OPERATING IN THE THZ GAP REGION

We performed a series of simulation studies on different types of antennas using COSMOL software for their implementation in experiments on AFM based THz spintronics for the generation and detection of the EM signals. Spiral and bowtie antennas operating at several frequencies were designed and their THz emission pattern was studied. Bowtie antennas were concluded to be applicable for the desired purpose in our experiments. For the optimized geometry of the bowtie antenna, the resonant length was calculated for the range of frequency of our interest and flare angle dependence of resonant emission was studied as well. Results from those studies are summarized in the following sections.

Study on spiral antennas

A set of spiral antennas having operating frequencies 500GHz, 1THz, 1.5THz and 2THz were designed by considering parameters for the MgF₂ substrate and their emission spectra were studied using COSMOL software package. A flow of a DC current in the order 10^8 A/cm² was considered while calculating the emission spectra and the AFM sample to be placed at the center of the spiral region of the antenna as shown in Fig. A.1(A). As evident from the figure, the antennas spiral in a direction where both input and output sides of the feed line rotate next to each other while meeting at the sample position. A detailed design of an antenna is shown in Fig. A.1(B). The blue lines connecting the spiral from the left and the right side represent the feed lines which supply the high-density DC current required to drive the AFM into resonance. Fig. A.1(C) represents the angular distribution of the radiation pattern around the antenna perpendicular to the antenna plane. The black line at the center connecting 90° to 270° separates the substrate and the air. While the radiation intensity increases significantly with increase in frequency, it is more drastic while going from 1THz (green curve) to 1.5THz (red curve). For all considered frequencies, the emission intensity seems to be maximum on the substrate side compared to the free space air. Fig. A.1(D), represent the THz current distribution in the antenna designed for 1.5THz. As we move away from the center of the spiral, the THz current intensity slowly decreases, and the decrease is not uniform towards

the outer spirals. Fig. A.1(E) and (F) represent the 2D and the 3D plots of radiation pattern for obtained for a 1.5THz spiral antenna, corresponding to the red curve in Fig. A.1(C).

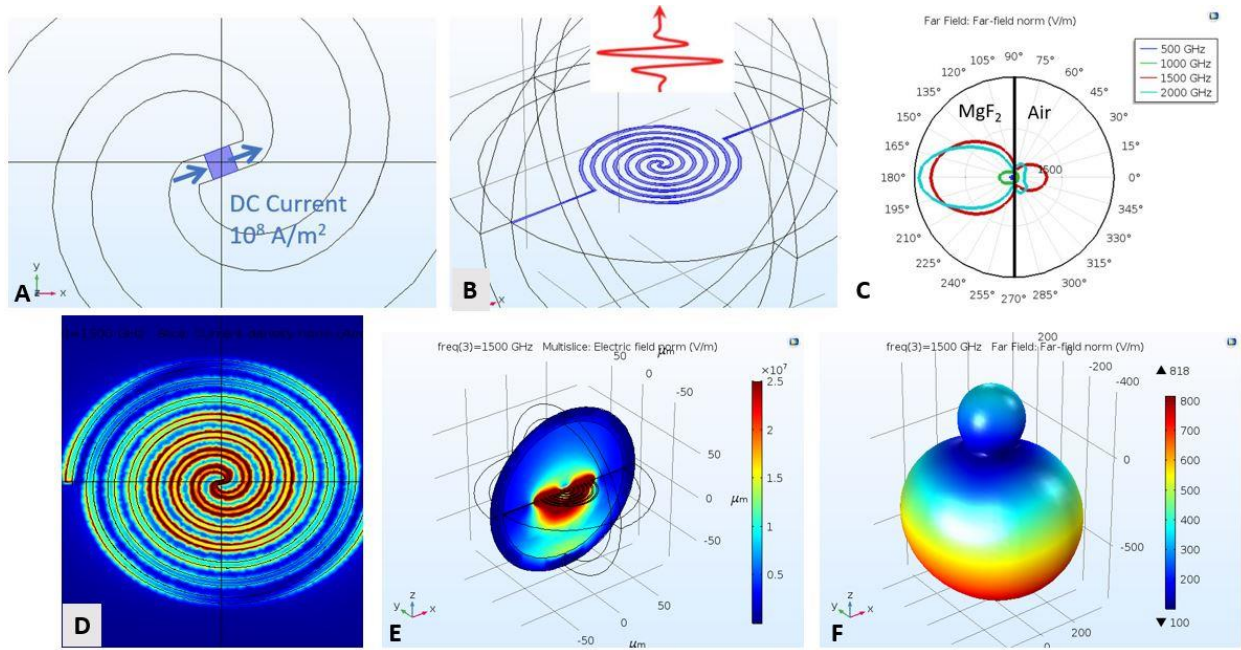


Figure A. 1: (A) A center part of a spiral antenna showing a small sample region and the direction of high-density dc current flow. (B) A spiral antenna with feed lines on the left and the right-side. (C) Angular distribution of the radiation pattern at different frequencies across the studied spiral antennas. Blue, green, red and cyan curves represent emission patterns for 500, 1000, 1500 and 2000GHz antennas respectively. The black line at the center connecting 90° and 270° separates the substrate from the air. (D)A THz current distribution in the spiral antenna operational at 1.5THz. (E)A 2D plot for the radiation intensity for 1.5THz antenna across a direction perpendicular to the antenna. The plane at 0 micron in the vertical direction separates the substrate (lower) and the air (upper) regions. (F)A 3D plot for the radiation distribution for a 1.5THz antenna.

In Fig. A.1(A) and (B), the narrow region of the microscopic sample extends and spirals out in similar microscopic manner. This limits the use of this type of antennas in experiments where a flow of high current density is required. Possible use of long and narrow Pt or Au wire in these antennas will lead to a higher resistance which makes it difficult to withstand the high current density, of the order 10⁸ A/cm²,

required for the operation of considered AFM based THz devices. Nevertheless, this type of antennas could be used to detect the THz radiation after efficiently directing them to the sample position using the antenna.

Study on bowtie-antennas

To overcome the shortcomings of spiral antennas regarding the flow of high current density through a device, we studied different types of bowtie antennas. Quick opening of the bow in a bowtie antenna across a narrow sample region reduces the resistance of the device and allows the flow of the high-density current through the sample. Different bowtie antennas having operational frequencies in the range from 200GHz to 1.5THz with different directions of feed lines were designed and studied.

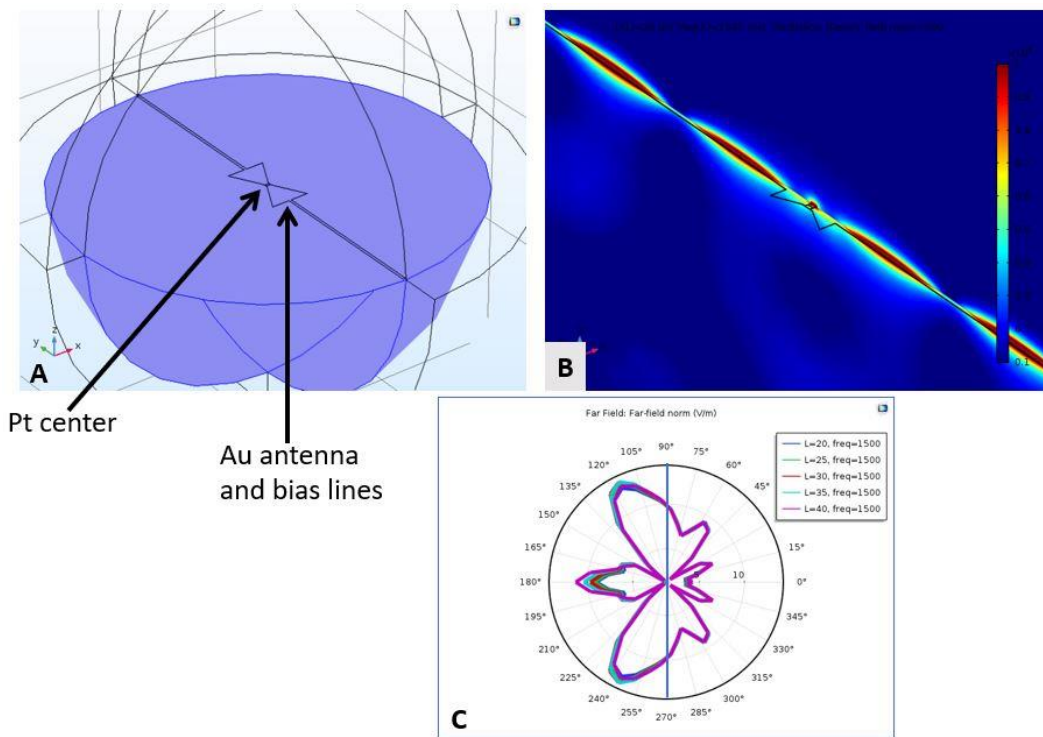


Figure A.2: (A) Design of a bowtie antenna on MnF₂ substrate with feed lines passing through the center of bows along the length of the antenna. The sample region is shown as the Pt center area where AFM sample will sit on top of Pt or any other high spin orbit coupling material. (B) Emission intensity plot across the antenna and the feed lines for an antenna in (A) with resonance frequency 1.5THz and length 20 μm (C) Angular distribution of the emission pattern for a set of 1.5 THz antennas with different bowtie lengths shown by color code.

Figure A.2(A) shows the design of a bowtie antenna where feed lines pass through the center of bows along the length of the antenna. The sample region is the constricted part at the center of the bowtie which quickly opens on both sides across the narrow sample region and helps in reducing the resistance of the device allowing the passage of high-density dc current only through the sample position at the center of the antenna. Fig. A.2(B) shows the plot of emission intensity along the length of the device having an antenna length of $20\mu\text{m}$ and operational frequency 1.5THz . From the emission, it appears the THz signal will flow through the bias line and give rise to dipolar emission at several places along the feed lines (emission areas outside the bowtie in the figure). This so called long-dipole antenna effect reduces the emission concentration from the bowtie region of the antenna and makes the bowtie non-influential for the radiated signal in this geometry. In other words, the feed lines become part of the resonator.

Figure A.2(C) shows angular distribution of radiated signal of 1.5THz bowtie antenna for different lengths. From this graphic, it seems the emission of these antennas at a given frequency is almost independent of the length over the considered range.

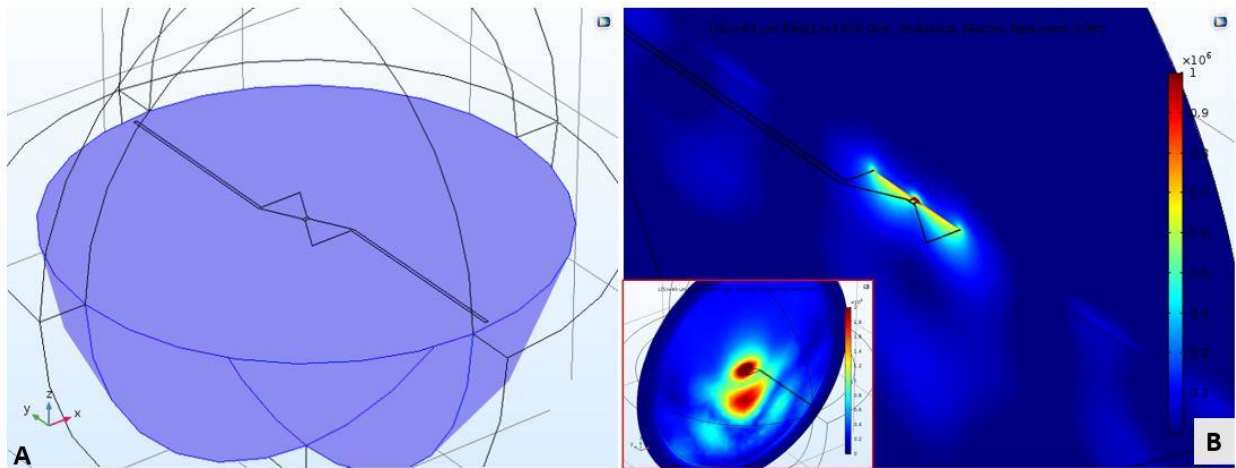


Figure A. 3: (A) A design of slightly different bowtie antenna on the MnF₂ substrate where feed lines pass through the opposite side of the flat edge of the bows. (B) Emission intensity plot for the type of antenna shown in (A) with a resonant frequency 1.5THz and length $40\mu\text{m}$. Inset of (B) shows the emission intensity across a plane perpendicular to the direction of the bowtie and passing through its center.

Figure A.3(A) shows a modified design of the bowtie antenna where feed lines pass longitudinally at the opposite sides of the flat edge of the bows. Fig. A.3(B) shows the emission plot for the design of the antenna shown in Fig. A.3(A) with operational frequency 1.5THz and length 40 μ m. In this case the THz signal is confined much better than in the earlier case. In this case the resonance occurring at the bowtie will enhance the emission but there is still some emission from the feed lines, due to THz signal passing through them, which can be seen as slightly lighted regions around the feed lines away from the bowtie. Inset of Fig. A.3(B) shows a transverse view of the emission on a plane transverse to and passing through the center of the bowtie. As explained in Appendix A for spiral antennas, the emission intensity is more towards the substrate side than the free space (separated by a horizontal diagonal line of the circular view).

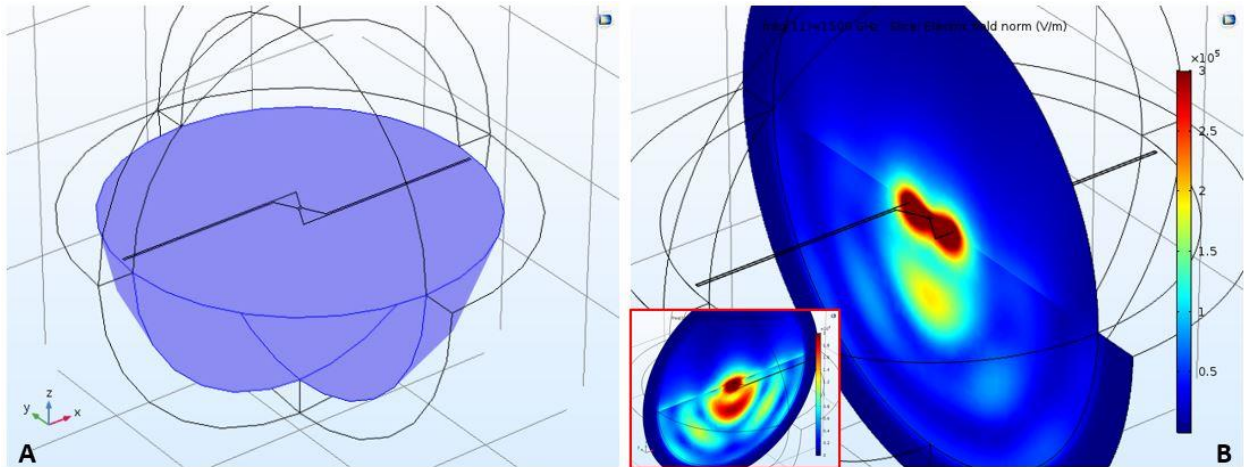


Figure A. 4(A): A design of a bowtie antenna on a MgF₂ substrate where the feed lines are transversal to the bowtie and enter through the opposite corners of the bows in the opposite directions. **(B)** Emission intensity plot for the design of the bowtie shown in (A) with resonant frequency 1.5THz. Inset of (B) shows the transverse view of the emission of the antenna across a plane perpendicular to and passing through the center of the bowtie.

Figure A. 4(A) shows another modified design of the feedlines of the bowtie antenna on a MgF₂ substrate where the feed lines are transversal to the bowtie and run through the opposite corners of the bows in the opposite directions. The emission intensity plot is shown in Fig. A. 4(B) where the intensity is

completely confined entirely to the bowtie and the emission is optimized. In this case there is no emission occurring around the feed lines. Inset of Fig. A. 4(B) shows the transverse view of the emission intensity through a plane perpendicular to and passing through the center of the bowtie. Due to the optimum emission of THz radiation from the bowtie, we will consider this design in our project for generation and detection of THz signals using AFM insulators.

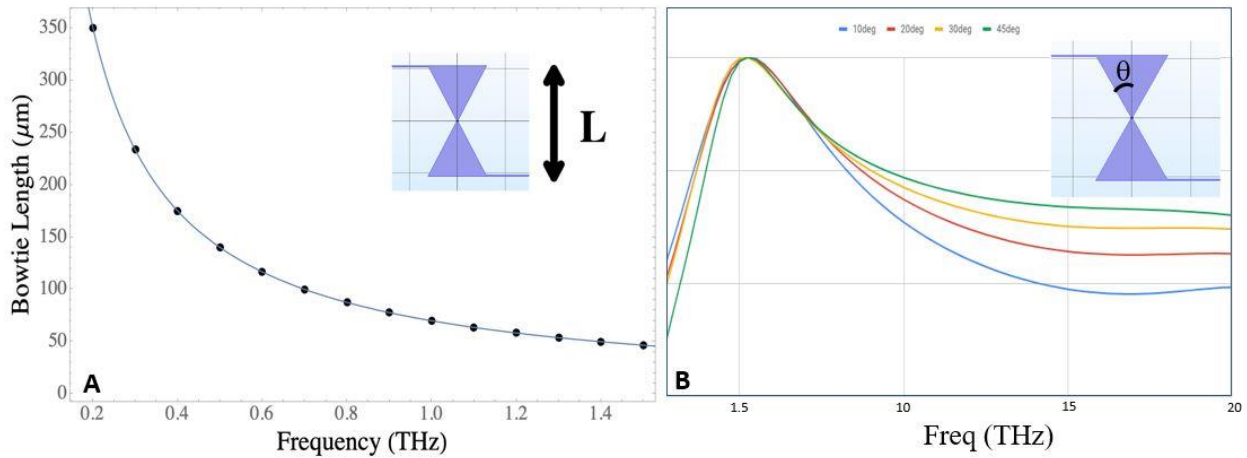


Figure A. 5: (A) A plot of calculated bowtie lengths for different frequencies at a 30° flare angle for the optimized antenna geometry. (B) The flare angle dependence of resonance linewidth for a 1.5THz bowtie antenna with the optimized geometry for the feedlines.

We have also calculated the required resonant lengths of the bowtie antennas for frequencies in the range from 200GHz to 1.5THz and the result is shown in Fig. A. 5(A). As shown in the figure, the required resonant length decreases nonlinearly with an increase in frequency of the antenna. A bowtie antenna of length $350\mu\text{m}$ is required for the resonant emission of radiation at 200GHz and that of length $50\mu\text{m}$ is required for resonant emission at 1.5THz. We also investigated for the flare angle dependence of the bowtie antenna for the optimized geometry at resonant length for a particular frequency. Fig. A. 5(B) shows the flare angle dependence of the resonant linewidth for a bowtie antenna of length $50\mu\text{m}$ resonating around 1.5 THz. The calculations show the resonant linewidth is not significantly dependent on the flare angle for

a given frequency. From this, we are considering our devices with flare angle 30° for which the resonant length at different frequencies is plotted in Fig. A. 5(A).

For some of the AFMs of our interest like MnF_2 and FeF_2 , it is required to have emission set up with circular polarization required by their chirality dependent dynamics. For this, two optimized bowtie antennas crossed to each other will be used to create the required circular polarization. Fig. A. 5(A) shows a linearly polarized bowtie antenna which will be used for emission/absorption experiments involving high frequency microwaves in THz and sub-THz region. The sample will sit in the constricted region of the bowtie shown by orange color in Fig. A. 6(A). Fig. A. 6(B) shows two bowties crossed at the constricted region which will be used for studies involving circular polarization. The sample will sit at the intersection region of two constricted regions.

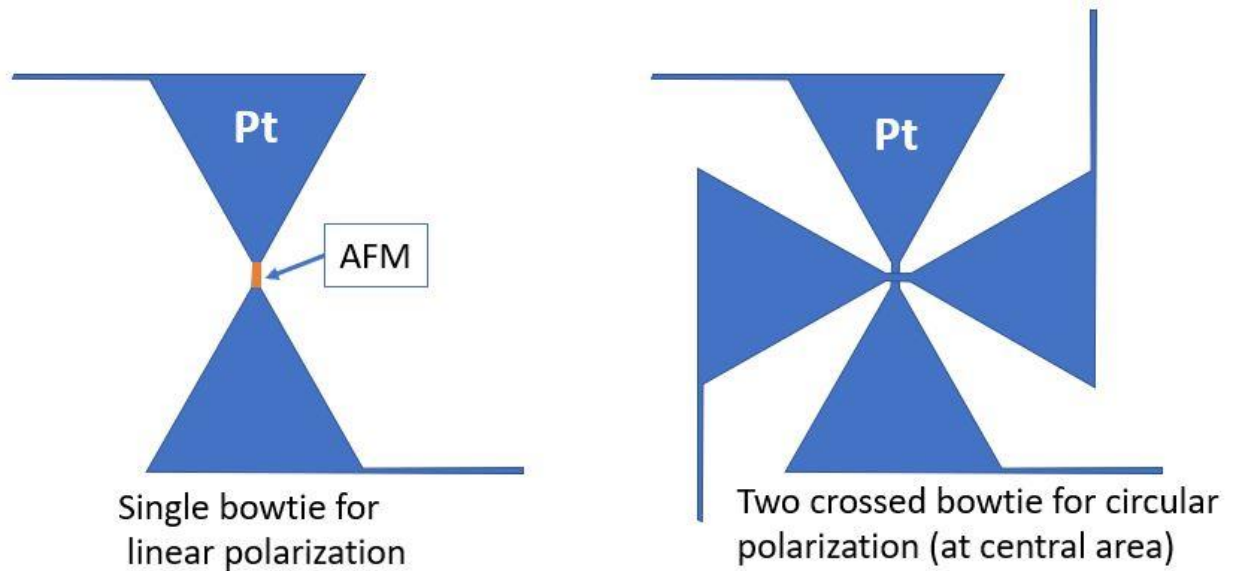


Figure A. 6: (A) Optimized geometry of single bowtie antenna which will be used for the emission/absorption of linearly polarized radiation. The magnetic sample will sit at the center of the bowtie in the constricted region (shown in orange color) (B) Two crossed bowtie which will be used for the emission/absorption of circularly polarized radiation. The magnetic sample will sit at the cross section of two bowties.

APPENDIX B: FABRICATION AND CHARACTERIZATION OF COPLANAR WAVEGUIDES AND STT-FMR DEVICES

The coplanar waveguides and the STT-FMR devices are fabricated by using the process of photolithography followed by metallization and lift off. The devices can be single- or multi- layered where any additional layers to a multilayered device can be added by following the same procedure as described below.

Photolithography process

Sample preparation and spin coating

These devices are usually fabricated on undoped semi-insulating GaAs wafers to match the requirement of 50 Ohm impedance matching.

- A clean GaAs wafer, whole or a big enough piece, should be cleaved into pieces of required dimension using diamond scribe.
- Resulting pieces of wafers should be cleaned with acetone, ethanol, isopropanol and DI water followed by blow dry with N₂ gas.
- Then the samples can be spin coated. If the sample is big enough to be held in vacuum chuck of the spinner, it can be directly placed otherwise it has to be anchored on top of small microscope slide using Lift Off Resist (LOR) to properly held in the vacuum chuck of spinner. The process involves putting a small amount of LOR on a glass slide with wafer piece on top and heating the slide on a hot plate at **110°C for 10 minutes**. In 10 minutes, the sample will be strongly held to the glass slide.
- **LOR** is spin coated first by applying a layer of it on top of wafer held on vacuum chuck of spinner following by spinning at **3000rpm for 30 seconds**.
- Then the resulting device should be baked on hot plate at **175°C for 5 minutes**.
- Once the sample cools down, photoresist **Shipley-1300** should be spin coated at **5000rpm for 30 seconds** and it should be baked at **125°C for 2 minutes**.

- Photoresist spin coated device should be protected from white light and UV-radiation until the next step is completed. Putting sample in an opaque sample holder or aluminum foil wrapping is highly recommended.

Mask-alignment, exposure, and development

- Check photomask under microscope for any dirtiness. If there is any dirt, the mask should be cleaned with acetone, isopropanol and DI water followed by sonication in DI water for at least 10 minutes. From my personal experience, I advise not to do the mask cleaning all the time as the cleaning process itself leaved some residue on the pattern making them irregular at the edges which are supposed to be very sharp otherwise. **The mask company, Advance Corp, offers free mask cleaning for their mask so we can do mask cleaning by the company if the mask gets dirty.**
- Put mask on the mask aligner and load sample on the stage at right position under the desired device pattern to be transferred on the chip. Do alignment using alignment markers if working on a multilayer device like STT-FMR. **Use manual for proper procedure of operating the mask aligner.**
- Check the UV intensity and calculate the exposure time needed for the required dose (**126mJ/cm²**). To calculate the time, you need to divide dose by the measured intensity.
- Set exposure time to calculated value and do exposure following the manual.
- Exposed sample should be taken out and developed in **CD-26 for 45 seconds** and then **quickly transferred to DI water** to stop the developing process followed by blow dry.
- Check device under microscope to see whether you have good pattern in terms of color, edges and dirt. If not think twice about the cause of defect and repeat the process until you get an optically nice-looking pattern. **Use of new CD-26 and DI water on each step is highly recommended to maintain cleanliness of the devices.**
- Then the device should be hard baked for **5 minutes at 125°C** on hop pan followed by cool down and undercutting development on **CD-26 for 1 minute**, DI water dipping and blow dry.

- Now the device is ready for a metallization but right before the metallization we descum the device in O₂ plasma for **20 second at 53 milli Torr O₂** pressure in SAMCO RIE to remove any residue. **(Follow proper procedure from the SAMCO manual)**

Metallization and lift off

- The ready to metallization sample should be loaded on the sample holder of the evaporator with upside of the device facing down of the evaporator. Devices can be easily anchored in the sample holder using Kapton tape. Many devices of similar type can be metallized at the same time.
- Put right metal crucibles with enough metal in the crucible pocket. For CPWs of both devices we use Ti(10nm)/Cu(220nm)/Au(20nm) layers. The **crucibles should be placed in right order**, so you evaporate titanium (sticking layer) first followed by copper (main conducting layer) and then gold (capping layer to protect copper from oxidation).
- The evaporation chamber should be pumped down to below **1x10⁻⁵ Torr** before starting the evaporation process. I recommend waiting until the pressure gets down to low -6 pressure range.
- Once the pressure is at desired level, evaporate metals in a right order **following proper evaporation procedure from the manual**. For Evan e-beam evaporator in Physics clean room, the tooling factor values keep changing from time to time so use the latest value of tooling factor while setting the evaporation parameters (z-ratio value, density of material used and tooling factor).
- Get right thicknesses of metal evaporated using evaporation rates around **0.5Å/sec for Ti, 2Å/sec for Cu and 1Å/sec for Au**.
- Once completed, let the system cool down and take the samples out.
- Dip the devices in the PG-remover solution in a petri dish and place it on hot top at 60°C. The lift off will take place slowly. Once the devices are completely lifted off, move them to DI water and finally blow dry.

- Now the CPW devices are ready to use in the experiments. Optionally, one can add a thin layer of SiO₂ layer (~20nm) on top of the device to protect it from dust particles and metal scratching. For this, microscope slides can be used as shadow mask for the SiO₂ layer deposition. The SiO₂ layer should be deposited in such a way that enough space is left on either end of the CPW giving ample room for electrical connections while mounting the sample in the sample holder.
- For STT-FMR devices, a similar process of photolithography is used and twice in the case where the sample is also required to be deposited from the photolithography process. In such case, photolithography is first done for the sample region and the sample is deposited at the center of CPW. Once the sample is lifted off, second photolithography is done to pattern the CPW using mask alignment process to align sample with respect to the CPW (using the alignment markers on the mask and the device). Then the device is metallized and lifted off resulting into a device which can be used for a measurement.

Device characterization

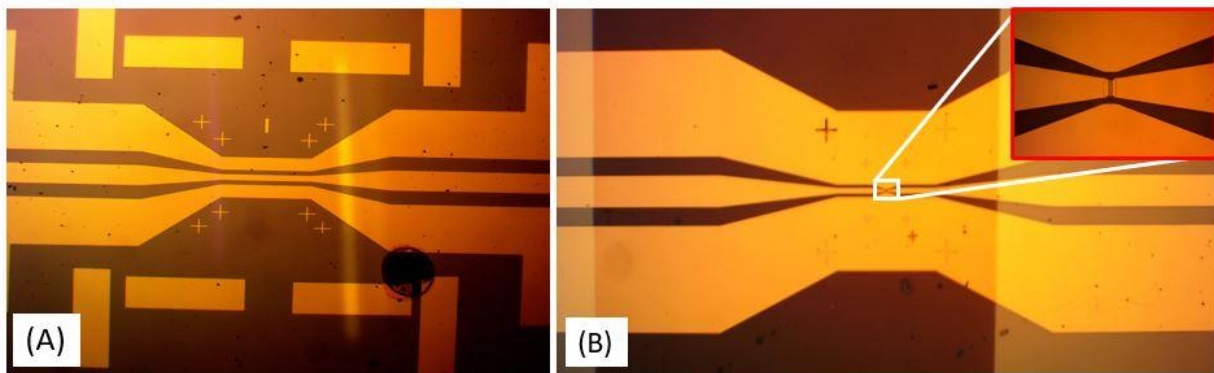


Figure A. 7: Microscope images of fabricated devices. (A) An image of a CPW fabricated by single step photolithography process. (B) An image of a STT-FMR device fabricated by using two step photolithography process. The inset shows the magnified view of the constricted sample region where a $15\mu\text{m}\times 25\mu\text{m}$ Pt/Py sample in the gap region is connected to the two ends of the central line of the CPW.

Microscope images in Fig. A.7(A) and (B) represent the fully fabricated CPW and STT-FMR devices which could be used for the measurement purpose. The inset in Fig. A.7(B) shows the sample (a $15\mu\text{m}\times 25\mu\text{m}$ Pt/Py stripe) region lying in the highly constricted region of the STT-FMR device. The fabricated CPWs and STT-FMR devices are characterized by measuring the microwave transmission parameter (S_{21}) using a vector network analyzer (VNA). Normal CPWs are continuous across the central line and thus can always be characterized for the microwave transmission whereas the presence of a sample gap in the STT-FMR devices limits similar characterization of STT-FMR devices. These devices can be characterized for microwave transmission if the sample in the gap region is an electrical conductor. In other cases, a STT-FMR device must be thoroughly examined microscopically for defects before attempting the actual measurement.

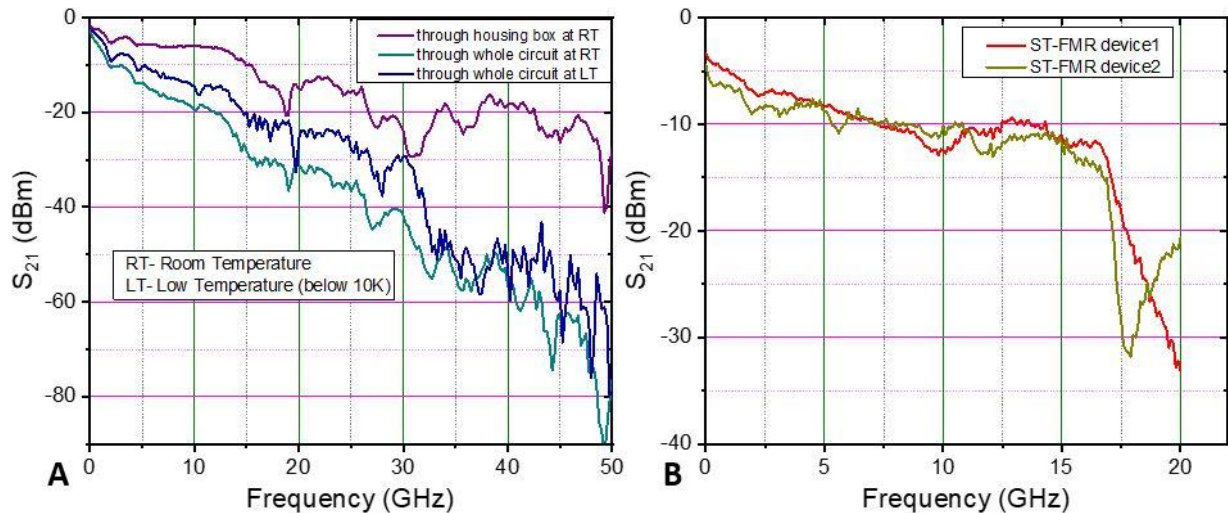


Figure A. 8: (A) Microwave transmission through a CPW from 10MHz to 50GHz under different conditions. The purple curve denotes the transmission through the sample in a housing box at the room temperature. The olive and blue curves respectively represent the transmission at room temperature and low temperature when the housing box with the CPW in (A) is put inside a cryostat. (B) Room temperature microwave transmission through two STT-FMR devices of different sample sizes in the frequency range 10MHz to 20GHz.

A device to be characterized is first mounted on a sample holder build specifically to fit these devices. The device is mounted using silver paint, as an adhesive, in such a way that it is stable on its position

as well as with respect to the connection to the microwave coaxial lines. The ground planes on either side of the device are grounded to the housing box which eventually gets grounded to the building ground. Overall connection to the device can be checked on the other side of the coaxials using a multimeter. For STT-FMR devices with a very small sample size, the current supplied by multimeter can fry the device and this test should be done in a low applied current using a Keithley or a lock in amplifier. Once a proper connection is established, the devices can be characterized for their microwave transmission property.

Figure A.8(A) shows characterization curves for a CPW from 10MHz to 50GHz under different external conditions. The purple curve represents the room temperature transmission after mounting the CPW in a housing box. The decrease in transmitted power (ideally linear) with increase in frequency corresponds to the increase in the microwave power in the circuit with increase in frequency. The dips in the spectrum are due to microwave reflection occurring at some points of the circuits. The olive-colored curve in the circuit corresponds to the microwave transmission at room temperature through the whole circuit which involves two long coaxials in the cryostat, the housing box, and several microwave adapters. The low transmission in this case, compared to the case involving only the housing box, corresponds to the additional losses caused by the insertion loss of additional adapters used and the loss caused by long coaxials. The blue curve represents the transmission through the whole circuit when the system is at low temperature (below 10K). At the lower temperatures the transmission through the stainless-steel microwave coaxials, used in the lower part of the cryostat, improves which corresponds to the upshift of transmission spectrum at lower temperatures. Depending on the type of sample used, we can perform experiments when the transmission is better than -30dBm. Below this level of transmission, the observed signals in the measurements done by using such CPWs get too noisy. Nevertheless, a careful fabrication of non-defective clean devices and improvement of microwave circuit, particularly at the joints, can reduce the losses in the circuit and lead to an overall circuit with low loss even at 50GHz. Fig. A.8(B) represent the room temperature transmission spectrum of two STT-FMR devices in the frequency range 10MHz to 20GHz

where the sample was made from Pt/Py heterostructure with sizes $15\mu\text{m}\times 15\mu\text{m}$ (red curve) and $15\mu\text{m}\times 25\mu\text{m}$ (brown curve).

Once the devices are characterized for the microwave transmission, they can be used in actual measurements where the characterization curves serve as a guide while choosing the microwave frequency. A rule of thumb is we don't want to choose a frequency corresponding to a sharp dip in the transmission spectrum.